DOT/FAA/AR-10/18

Air Traffic Organization
NextGen & Operations Planning
Office of Research and
Technology Development
Washington, DC 20591

Damage Tolerance and Durability of Fiber-Metal Laminates for Aircraft Structures

October 2010

Final Report

U.S. Department of Transportation
Federal Aviation Administration

NOTICE

This report is available at the Federal Aviation Administration William J. Hughes Technical Center's Full-Text Technical Reports page: actlibrary.tc.faa.gov in Adobe Acrobat portable document format (PDF).

Technical Report Documentation Page

1. Report No.	2. Government Accession No.	3. Recipient's Catalog No.
DOT/FAA/AR-10/18		

4. Title and Subtitle	5. Report Date
DAMAGE TOLERANCE AND DURABILITY OF FIBER-METAL LAMINATES FOR AIRCRAFT STRUCTURES	October 2010
	6. Performing Organization Code

7. Author(s)	8. Performing Organization Report No.
Jenn-Ming Yang, Thomas H. Hahn, Hyoungseock Seo, Po-Yu Chang, and Po-Ching Yeh	

9. Performing Organization Name and Address	10. Work Unit No. (TRAIS)
Mechanical and Aerospace Engineering Department Materials Science and Engineering Department University of California at Los Angeles Los Angeles, CA 90024-1597	
	11. Contract or Grant No. 04-C-AM-UCLA

12. Sponsoring Agency Name and Address	13. Type of Report and Period Covered
U.S. Department of Transportation Federal Aviation Administration Air Traffic Organization NextGen & Operations Planning Office of Research and Technology Development Washington, DC 20591	Final Report
	14. Sponsoring Agency Code AIR-100

15. Supplementary Notes

The Federal Aviation Administration Airport and Aircraft Safety R&D Division Technical Monitor was Curt Davies.

16. Abstract

Fiber-metal laminates are a family of hybrid metal and composite laminates for aircraft structural applications. These hybrid laminates have the advantage of metal and fiber-reinforced composites, providing superior mechanical properties to the conventional lamina merely consisting of fiber-reinforced lamina or monolithic aluminum alloys. As a replacement of high-strength aluminum alloys, S2-glass fiber-reinforced aluminum laminates (GLARE) have been applied to aircraft structures for weight reduction and improved fatigue resistance. The research and development activities have covered damage tolerance and durability of GLARE subjected to multiple impacts and multiple-site fatigue damage.

The experiment and finite element simulation for low-velocity multiple impacts was performed on GLARE laminates in this report. Drop-weight impact was applied twice at a variety of energy levels to inflict multiple-impact damages for aluminum 2024-T3 and GLARE 5-2/1. The numerical model using the finite element method was developed by using the commercial finite element code ABAQUS and verified by comparing to the experimental data. The two- and three-dimensional failure criteria in composite layer were used to predict all dynamic responses, including load-time history, maximum deflection-time history, and damage progression. In addition, the user-defined material subroutine VUMAT was developed and linked with ABAQUS to represent a three-dimensional progressive failure. The finite element simulation showed good agreement with experimental data for multiple-impact behavior.

The multiple-site fatigue damage behaviors of fiber-metal laminates were investigated experimentally and analytically under constant-amplitude fatigue loading. It was found that the presence of multiple-site fatigue cracks would accelerate the crack growth rates in the metal layers of fiber-metal laminates as two propagating cracks approach each other. An analytical methodology was proposed to calculate the fiber-bridging stress based on the crack-opening relations. The multiple-site crack growth rates were predicted by an empirical Paris-type fatigue law. The effective stress-intensity factor (SIF) at a crack tip was formulated as a function of applied SIF, crack-opening SIF, and nondimensional SIF. Weight function approach was used for SIF calculation. The predicted crack growth was validated by the experiments.

17. Key Words	18. Distribution Statement
Fiber-metal laminates, GLARE, Multiple-site damage, Multiple impacts, Fatigue crack growth	This document is available to the U.S. public through the National Technical Information Service (NTIS), Springfield, Virginia 22161. This document is also available from the Federal Aviation Administration William J. Hughes Technical Center at actlibrary.tc.faa.gov.

19. Security Classif. (of this report)	20. Security Classif. (of this page)	21. No. of Pages	22. Price
Unclassified	Unclassified	83	

TABLE OF CONTENTS

LIST OF FIGURES

LIST OF TABLES

LIST OF SYMBOLS AND ACRONYMS

Al	Aluminum
σ_{ij}	Material stress state
ε_{ij}	Material strain state
ε_{ij+}^{init}	Tensile strain component at failure
ε_{ij-}^{init}	Compressive strain component at failure
f^{ft}	Hashin fiber tension failure initiation
f^{fc}	Hashin fiber compression failure initiation
f^{mt}	Hashin matrix tension failure initiation
f^{mc}	Hashin matrix compression failure initiation
E_{11}	Composite modulus along the fiber axis
E_{22}	Composite modulus transverse to the fiber axis
υ_{12}	Poisson's ratio for the fiber-matrix direction
υ_{23}	Poisson's ratio for the matrix-matrix direction
G_{12}	Shear modulus fiber-matrix direction
t	Time value at the current finite element analysis increment
Δt	Time step between successive increments
$\dot{w}^i$	Damage propagation rate for each failure mode (i)
w^i	Damage state variable for each failure mode (i)
Ω_0	Damage nucleation rate constant
Ω_1	Damage growth rate constant
S_{ij}	Material compliance matrix
d	Material degradation factor
C_{ij}	Material stiffness matrix
v_i	Velocity vector
T_i	Surface traction vector
F_i	Body force vector
ρ	Density
U	Internal energy per unit volume
W	Internal energy
$\dot{\varepsilon}_{ij}$	Strain rate
S_{ijkl}	Material compliance tensor
C_{ijkl}	Material stiffness tensor
I_{ijkl}	Fourth-order identity tensor
2D	Two-dimensional
2D	Three-dimensional
BVID	Barely visible impact damage
C3D8R	Hexahedral solid element
CVID	Clearly visible impact damage
FML	Fiber-metal laminates
FE	Finite element
GLARE	S2-glass fiber-reinforced aluminum laminates

MSD	Multiple-site damage
SC8R	Hexahedral shell continuum element
SIF	Stress-intensity factor
VUMAT	User-defined material subroutine

EXECUTIVE SUMMARY

Fiber-metal laminates (FML) are a family of hybrid metal and composite laminates for aircraft structural applications. Commonly, FMLs, such as aramid-reinforced aluminum laminates and S2-glass fiber-reinforced aluminum laminates (trade name GLARE), are composed of alternating layers of unidirectional or bidirectional fiber-reinforced prepregs with aluminum alloy sheets. These hybrid laminates have the advantage of metal and fiber-reinforced composites, providing superior mechanical properties compared to the conventional lamina, which merely consists of fiber-reinforced lamina or monolithic aluminum alloys. As a replacement of high-strength aluminum alloys, GLARE laminates have been applied to aircraft structures, such as the Airbus A-380, including fuselage and leading edges, for weight reduction and improved fatigue resistance. This report summarizes a comprehensive study on the damage tolerance and durability of GLARE subjected to impact and dynamic fatigue loading. Specifically, this study focused on investigating the multiple impacts and multiple-site fatigue damage of GLARE laminates.

For multiple-impact behavior, two different levels of impact energy were used to inflict barely visible impact damage and clearly visible impact damage on the laminates. The experiment and finite element (FE) simulation for low-velocity multiple impacts was performed on GLARE laminate. Drop-weight impact was applied twice at a variety of energy levels to cause multiple-impact damages for aluminum 2024-T3 and GLARE 5-2/1. The numerical model, using the FE method, was developed by using the commercial FE code ABAQUS and verified by comparing to the experimental data. The two-dimensional and three-dimensional (3D) failure criteria of the composite layers were used for predicting all dynamic responses, including load-time history, maximum deflection-time history, and damage progression. The 3D progressive failure model was incorporated into the user-defined material subroutine (VUMAT) in the ABAQUS software package. The FE simulation shows good agreement with experimental data for stress analysis under multiple-impact loads.

The multiple-site fatigue damage behaviors of FMLs were investigated experimentally and analytically under tension-tension, constant-amplitude fatigue loading. It was found that the presence of multiple-site fatigue cracks would accelerate the crack growth rates in the metal layers of FMLs as two propagating cracks approached each other. An analytical methodology was proposed to calculate the fiber-bridging stress based on the concept of crack-opening relations. The multiple-site crack growth rates were predicted by an empirical Paris-type fatigue law in which the effective stress-intensity factor (SIF) was formulated as a function of applied SIFs, crack-opening SIFs, and nondimensional SIFs. The predicted crack growth was validated by constant-amplitude fatigue tests at various stress levels on multiple-site damage specimens.

1. INTRODUCTION.

Fiber-metal laminates (FML) are a family of hybrid metal and composite laminates for aircraft structural applications. Commonly, FMLs, such as aramid-reinforced aluminum laminates and S2-glass fiber-reinforced aluminum laminates (trade name GLARE), are composed of alternating layers of unidirectional or bidirectional fiber-reinforced prepregs with aluminum alloy sheets. GLARE was invented by the Delft University in the Netherlands [1 and 2]. These hybrid laminates have the advantage of metal and fiber-reinforced composites, providing superior mechanical properties compared to the conventional lamina, which merely consist of fiber-reinforced lamina or monolithic aluminum alloys. As a replacement of high-strength aluminum alloys, GLARE laminates have been applied to aircraft structures, such as the Airbus A380, including fuselage, leading edges, etc., for weight reduction and improved fatigue resistance [3]. There are different grades of GLARE laminates, as shown in table 1. Because of different lay-up sequence and fiber orientation, different grades of GLARE laminates have different mechanical properties. A typical GLARE 3-3/2 laminate is shown in figure 1.

Table 1. Grades of GLARE Laminates

GLARE Grade	Subgrades	Metal Sheet Thickness (mm) and Alloy	Prepreg Orientation in Each Fiber Layer	Main Beneficial Characteristics
1		(0.3-0.4) 7475-T761	0°/0°	Fatigue, strength yield stress
2	GLARE 2A	(0.2-0.5) 2024-T3	0°/0°	Fatigue, strength
	GLARE 2B	(0.2-0.5) 2024-T3	90°/90°	Fatigue, strength
3		(0.2-0.5) 2024-T3	0°/90°	Fatigue, impact
4	GLARE 4A	(0.2-0.5) 2024-T3	0°/90°/0°	Fatigue, strength in 0° direction
	GLARE 4B	(0.2-0.5) 2024-T3	90°/0°/90°	Fatigue, strength in 90° direction
5		(0.2-0.5) 2024-T3	0°/90°/90°/0°	Impact
6	GLARE 6A	(0.2-0.5) 2024-T3	(+)45°/(-)45°	Shear, off-axis properties
	GLARE 6B	(0.2-0.5) 2024-T3	(-)45°/(+)45°	Shear, off-axis properties

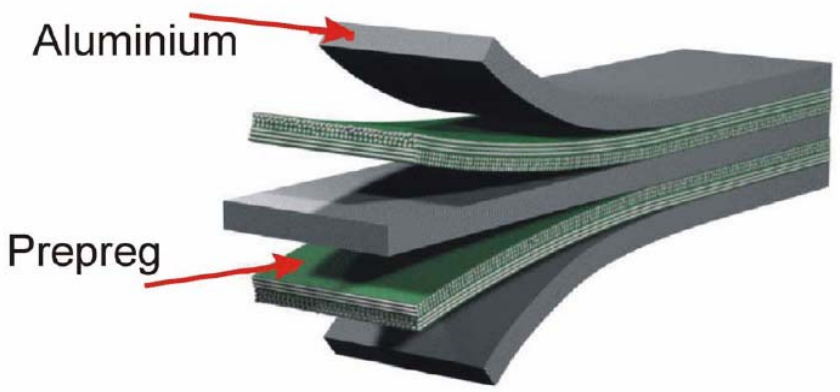

Figure 1. A Cross-Ply GLARE 3-3/2 Laminate

It is well known that FMLs exhibit excellent fatigue crack growth resistance due to the fiber-bridging mechanism, as shown in figure 2. As the crack propagates, the crack opening is restrained by the intact fibers in the wake of the fatigue crack. This results in a reduction of stress-intensity factor (SIF) at the crack tip and a far lower fatigue crack growth rate compared to the monolithic aluminum alloy.

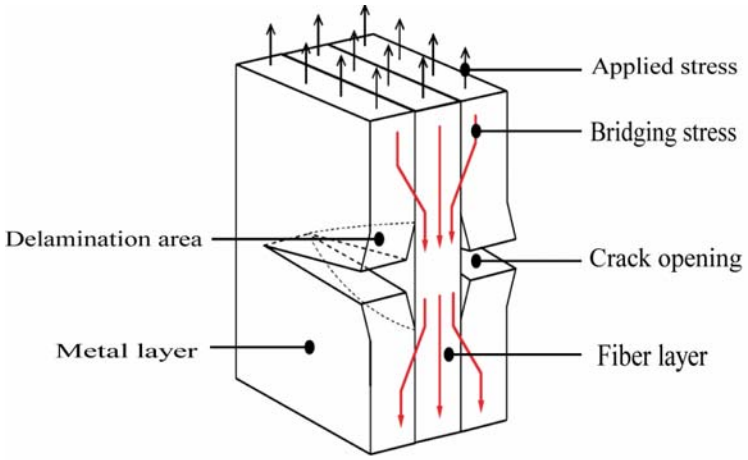

Figure 2. Bridging Mechanism in FMLs With Cracked Metals and Delamination

For aircraft composite structures, the most significant safety issues are impact resistance, damage durability, and tolerance after single or multiple impacts. Impact damage of aircraft structures can occur by a collision between cargo vehicles, dropped tools during maintenance, hail, bird strikes, and lightning strikes [4]. Damage caused by impact degrades laminate stiffness and strength, which is the load-bearing ability of the structure [5 and 6]. In general, if the impact energy is low, only barely visible impact damage (BVID) will occur. However, if the impact is repeated, even if it is at the level of low-impact energy, the small dent damage may accumulate. Thus, it would lead to strength reduction in FMLs, as observed in references 7-11. However, the information for FMLs subjected to multiple-impact loads is limited in the literature. More studies are needed to investigate the multiple-impact scenarios in FMLs.

In 1988, Aloha Airline Flight 243 suffered explosive decompression when part of the fuselage ruptured during flight due to metal fatigue and failed epoxy bonding. The multiple-site fatigue damage in metallic airframe has received considerable attention. Since that accident, much research has been conducted to study the multiple-site damage (MSD) problems in aircraft structures to avoid catastrophic failure in flight [12-18]. When monolithic aluminum alloys are subjected to cyclic fatigue load, cracks emanate around the fastener holes and propagate. A number of neighboring cracks might coalesce to form a single dominant crack. As these fatigue cracks are present in the fuselage of an aging aircraft, significant load redistribution will occur, especially ahead of the dominant cracks. The interaction of fatigue cracks will increase the SIF and enhance the crack growth rate in metallic alloys. Subsequently, the residual strength is reduced and the integrity of structural components is affected.

In FMLs, the crack propagation and fracture characteristics are essentially different from those of metallic alloys. When FMLs are subjected to fatigue loading, cracks initiate and progress in the metal layer. The crack opening in the metal layers is restrained by the intact fibers in the wake of the fatigue crack. The crack growth in the metal layer is impeded by the fiber-bridging mechanism, resulting in a much lower crack growth rate compared to monolithic aluminum alloy. As a result, it is anticipated that the influence of multiple-site damage in FMLs will differ from that of a metallic structure. Also, MSD fatigue may occur only in the surface metal layers, i.e., a crack through the thickness direction of a single aluminum surface layer. These surface cracks may initiate from a scratch, a notch, or an impact damage site. In the FML surface crack configuration, the fiber-bridging effect can be treated as a crack opening bridged by the intact laminate [19]. Away from the surface metal layer and fiber/prepreg with delamination, the remaining intact laminate is able to support the outer surface metal layer, leading to significant reduction of stress level in the cracked metal layer. Also, though FMLs are designed symmetrically in lay-up sequence, the presence of the surface cracks would make the laminates unsymmetrical. Besides the fiber-bridging effect in crack growth, there is neutral line shift/deflection from secondary bending because of unsymmetrical internal stresses in laminates [20]. The secondary bending effect increases stresses in the layers, depending on the laminate thickness and the crack length. If the thickness of the FMLs is large compared to crack length, the shift of the neutral axis of a laminate induced by the cracked outer metal layer would be small, and the corresponding secondary bending can be neglected. Concerning multiple-site surface crack growth, there is very few data available in current literature [19-21] that studies crack propagation, crack linkup phenomena in cracked surface metal layers of FMLs under cyclic load. The fatigue behavior of FMLs with the presence of MSD has not been well documented. A better understanding of the multiple-site fatigue damage behaviors in FMLs, such as crack growth interaction, crack linkup, and delamination linkup, are structural integrity concerns.

In this study, experiments and finite element (FE) simulations were conducted to study the multiple-impact behavior of GLARE laminates. The commercial FE software package ABAQUS was used with VUMAT (explicit user-defined material subroutine) to simulate the damage progression in composite layers of GLARE laminates. The simulation results were validated with experiments. The multiple-site fatigue damage in GLARE laminates was then experimentally investigated under different applied loads with detailed damage characterization. Both through-thickness and partial-thickness MSD fatigue scenarios were studied to understand

crack and delamination interactions. An analytical prediction model of crack growth was developed and experimentally validated.

2. TEST PROGRAM AND TEST MATRIX.

2.1 MULTIPLE-IMPACT LOAD TEST.

2.1.1 Materials.

Aluminum (Al) 2024-T3 and GLARE 5-2/1 were used for multiple-impact experiments. Figure 3 shows the configuration of GLARE 5-2/1 laminates used in the present experimental investigation. Figure 3(a) shows that GLARE 5-2/1 laminate consists of two layers of Al 2024-T3 and one layer of [0°/90°/90°/0°] glass/epoxy composite, and figure 3(b) shows a cross-sectional view of GLARE 5-2/1 in detail. The materials properties of GLARE constituents are shown in table 2.

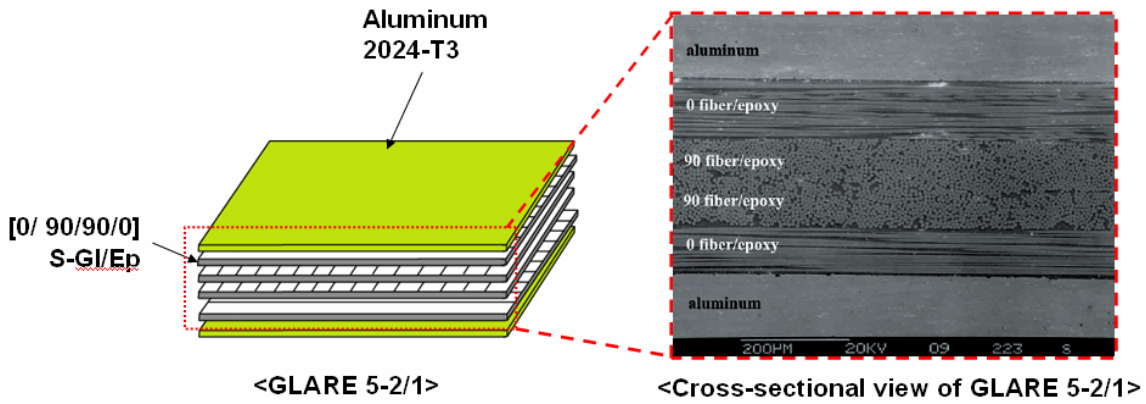

(a) (b)

Figure 3. (a) Schematic and (b) Cross-Sectional Views of GLARE 5-2/1

Table 2. Materials Properties of GLARE Laminates

	Al 2024-T3	S2-Glass Fiber/Epoxy
E_x (GPa)	72.4	55.5
E_y (GPa)		9.5
G_{xy} (GPa)	2706	5.55
σ_{ys} (MPa)	369	
ν_{xy}	0.33	0.3
ν_{yx}	0.33	0.0575
α[1/°C]	$22x10^{-6}$	$6.1x10^{-6}$
t (mm)	0.3~0.4	0.133

2.1.2 Specimen Geometry, Coordinates, and Impact Energy.

The average thickness of different layers was measured using optical micrographs. For GLARE 5-2/1, the average thickness of the Al layer was 0.489 mm, and the average thickness of the composites was 0.584 mm. The total laminate thicknesses were 1.562 mm for GLARE 5-2/1. The average thickness of the Al 2024-T3 sheet was 1.60 mm. For multiple-impact load tests, all specimens were cut by a water jet to a size of 76.2 x 76.2 mm. The GLARE 5-2/1 was examined carefully for any damage caused by cutting. Diverse impact energies like 8 J (2x4J), 16 J (2x8 J), and 26 J (2x13 J) were applied by adjusting the dropping height in low-velocity, multiple-impact tests. Two scenarios were studied for the multiple-site impact damage, as shown in figure 4.

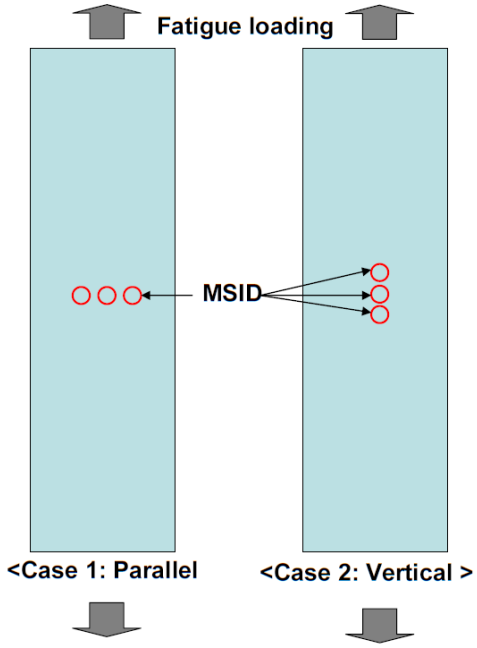

Figure 4. Multiple-Site Impact Damage Specimens

2.1.3 Impact and Postimpact Test Article Instrumentation and Procedure.

As shown in figure 5, low-velocity impact tests were conducted on a Dynatup® Model 8250 drop weight impact tower at impact velocities below 5 m/s. Al 2024-T3 was used as a baseline for comparison with GLARE laminates. The data during impact testing were collected by a PC-based data acquisition system: GRC 930-I Dynatup with a photodiode velocity detector. After just applying impact, the pneumatic rebound breaks are activated to push up and hold the impactor assembly in place so that the specimen is not subjected to multiple impacts. To achieve multiple-impact damages, the impactor was dropped twice on the same locations of Al 2024-T3 and GLARE 5-2/1. The specimens were clamped between two 114.3- by 114.3-mm-square steel plates. The steel plates had a 31.7-mm-diameter circular opening at the center. A 12.7-mm-diameter steel rod with a semi-spherical end, and a mass of 5.6 kg, was used as an impactor.

Figure 5. Dynatup Model 8250 Instrumented Drop Weight Impact Tower

As shown in figure 6, after the impact test, postfatigue tests were conducted and the crack length was measured on each crack site. After the impact or postimpact fatigue test, characterization was performed to investigate the state of damage. The outer Al layers of the GLARE laminate were removed chemically, using sodium hydroxide solution, to observe the damage characteristics in the S2-glass fiber/epoxy layer after any two cracks linked or cracks reached the edge of the specimens.

Figure 6. Multiple-Site Impact Damage Fatigue Test

2.2 MULTIPLE-SITE DAMAGE FATIGUE TEST.

2.2.1 Materials.

The materials used in this study were GLARE 3-3/2 that consisted of three thin layers of Al 2024-T3, bonded together with two thin S2-glass fiber layers in an FM®94 adhesive system. These materials were manufactured and provided by Airbus, Germany. They were cured in an autoclave cycle with a maximum pressure of 6 bar at a curing temperature of 120°C. The lay-up for this grade of GLARE laminate is defined as [2024-T3/0° glass fiber/90° glass fiber/2024-T3/90° glass fiber/0° glass fiber/2024-T3].

To avoid secondary bending effects due to unsymmetrical internal stresses present in the FMLs, these GLARE laminates have a symmetrical lay-up. The materials properties of the constituents of GLARE laminates are listed in table 2.

2.2.2 Specimen Geometry, Coordinates, and Loads.

The specimen dimensions were 300 mm in length and 75 mm in width. Two types of MSD were introduced: through-thickness open holes and surface slits. The spacing in between two neighboring open holes/slits was 30 mm, and the distance in between the top and bottom rows of circular holes/surface slits was 100 mm. For through-thickness specimens, two rows of open holes were carefully prepared with radii of 2.5 mm (length of 4 mm), and the starter notch was 1 mm in length. For partial-thickness specimens, two rows of surface slits were carefully prepared with a length of 4 mm. The width of the slit was 1 mm. The configuration is shown in figure 7 for both through-thickness specimens and partial-thickness specimens. No delamination occurred during machining, as shown in figure 8.

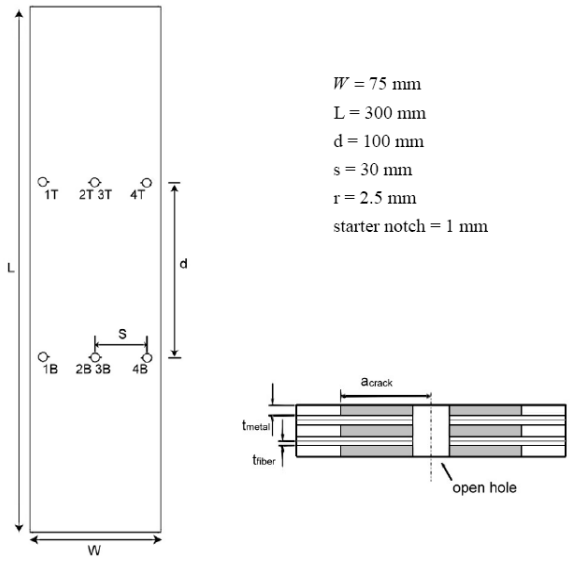

(a)

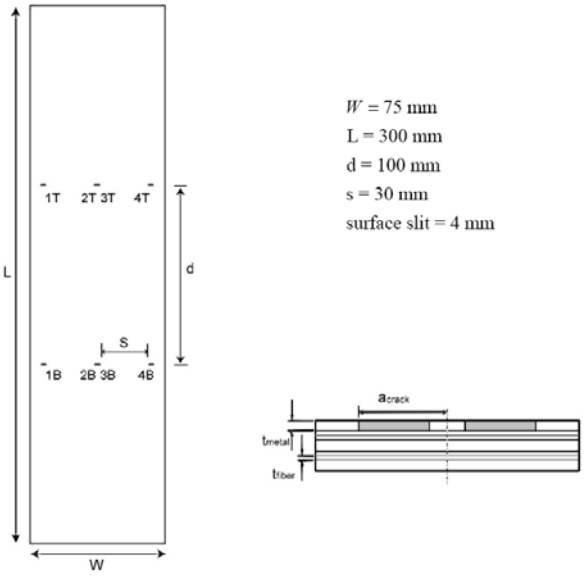

(b)

T = top B = bottom

Figure 7. Configuration of GLARE 3-3/2 Laminate Specimens (a) Through-Thickness MSD and (b) Partial-Thickness MSD

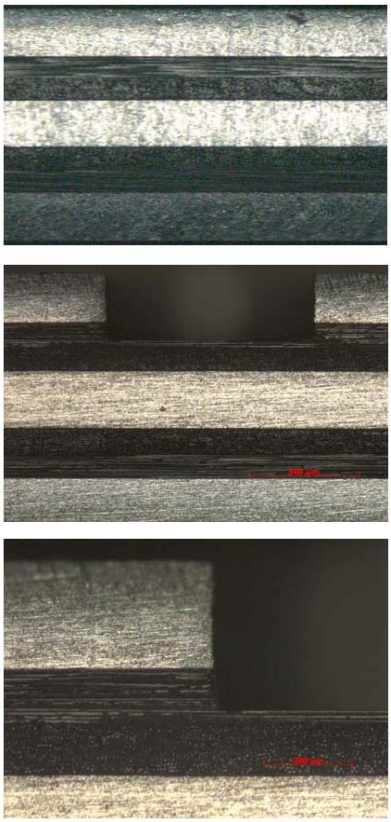

Figure 8. Cross-Sectional View of GLARE 3-3/2

2.2.3 Fatigue Test Article Instrumentation and Procedure.

The constant-amplitude fatigue tests were conducted using a servohydraulic testing machine, INSTRON™-8350. The fatigue test was done according to ASTM D 3479 [22]. All constant-amplitude fatigue tests were conducted in tension-tension loading at a frequency of 10 Hz and a stress ratio of R = 0.05. Tests were conducted in a sinusoidal cyclic waveform under load control. The maximum applied stress levels were 120 MPa and 100 MPa, respectively. The crack lengths as a function of fatigue cycles for GLARE 3-3/2 specimens were recorded through continuous monitoring during the fatigue tests. After the fatigue tests, the chemical-mechanical removal method was used to detect the delamination in the interface of metal/prepreg in GLARE laminates. To investigate the fatigue cracking in the inner Al layers of GLARE 3-3/2, the surface aluminum sheets were etched away by chemical solutions, and the composites layers were removed mechanically.

3. ABAQUS FE SIMULATION FOR FMLs UNDER MULTIPLE-IMPACT LOADS.

The ABAQUS FE simulation work was performed to represent and predict the response to multiple-impact behavior in GLARE laminates. The response was then compared to Al 2024-T3.

3.1 GENERAL DEVELOPMENT OF FE MODELING.

The multiple impact was simulated under a diverse multiple-impact energy level using the commercial FE code ABAQUS [23]. The applied impact energy levels in the FE model were identical to what was used in the experiments. The FE model was simulated for BVID with 8 J (2x4 J) and 16 J (2x8 J)) and clearly visible impact damage (CVID) with 26 J (2x13 J)). In the FE simulation of GLARE 5-2/1, the same geometry of the specimens used in the experiments was taken. For predicting damage caused by impact, the ABAQUS/Explicit solver was used for GLARE laminates. The element types used in the simulation work were hexahedral solid element (C3D8R) for the aluminum layer and hexahedral solid element (C3D8R) and hexahedral shell continuum element (SC8R) for the composite layer with different fiber orientation. Damage in GLARE laminate can be distinguished between damage in aluminum and in S2-glass/epoxy layers. The aluminum layers were assumed to have elastic-plastic deformation in compression and crack damage in tension. For damage in the fiber/prepreg, both the damage in the epoxy matrix and in the fiber layers was considered. The first damage was caused by cracking under tension, and the second damage was caused by fiber and matrix failure under tensile loading [24]. The damage that occurred in the S2-glass/epoxy layer was implemented in ABAQUS using VUMAT. The S-2 glass fiber-reinforced composite layers were modeled with VUMAT, which was developed based on Hashin three-dimensional (3D) failure criteria [25], to degrade the stiffness. When each node was integrated in the composite layer during multiple impacts, VUMAT was used to calculate the stiffness matrix.

In modeling dynamic impact behavior, because of the excessive distortion that some FEs may experience, this nonlinearity of constitutive behavior would lead to complicity in convergence or divergence. The issue of numerical convergence needs to be addressed properly to prevent the occurrence of divergence of numerical solution. In ABAQUS, the parameters' "hour glassing" are used to hasten the convergence of numerically nonlinear modeling for the reduced integration elements, such as C3D8R and SC8R, in stress/displacement analyses [23]. To eliminate the singularity upon the integration point, hourglass control is critical in the nonlinear impact simulation. If the returned stress/strain value from the integration point is zero, the degree of distorted meshes will not be able to be controlled. Numerically, the FE model will go divergent.

Figure 9 shows the experimental setup compared to the FE mesh. Since the impact load was only on the near-field meshed grids, the far-field meshed grids were not considered, as shown in figure 9(a). The GLARE laminate mesh was modeled based on the real size of the impact fixture hole. The cross and front views of the FE model are shown in figure 9(b) and (c), respectively. As shown in the cross and front views of the multiple-impact loads, two impact loads were applied at a different time interval. There were no interactions between these two impactors simulated as rigid bodies in FE modeling, although they did have contact. The boundary conditions in figure 9(d) correspond to the experimental setup. Because of the symmetry of GLARE 5-2/1 laminates, only half the laminates were modeled with symmetrical boundary conditions applied. All edge elements were fixed in the x, y, and z directions with zero

displacement. The rigid body simulated as an impactor was allowed to move only along the z direction with zero rotation. The materials properties and damage failure criteria [24, 26, and 27] of GLARE 5-2/1 laminates used in this model are summarized in tables 3 and 4, respectively.

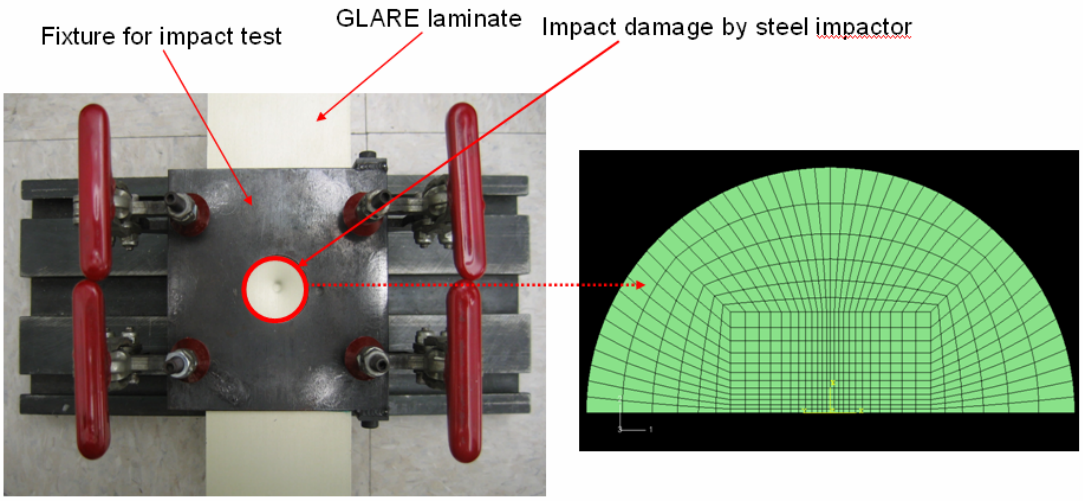

(a) Experimental Setup and FE Mesh

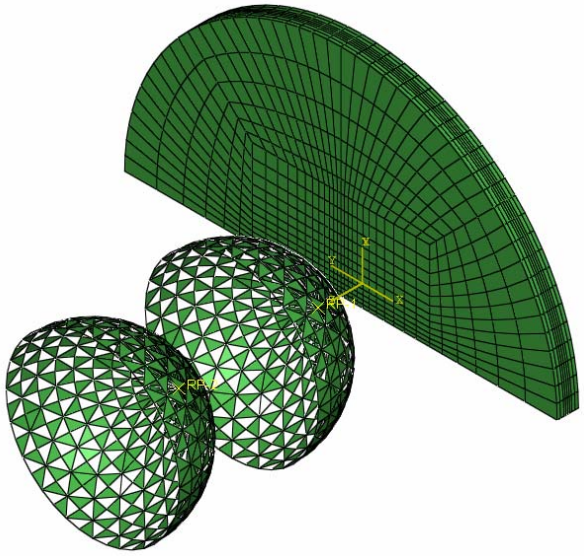

(b) Cross View of Multiple Impacts

Figure 9. Finite Element Model Geometry and Boundary Conditions (a) Experimental and Mesh Setup, (b) Cross View of Multiple Impacts, (c) Meshed Model of GLARE 5-2/1, and (d) Boundary Condition

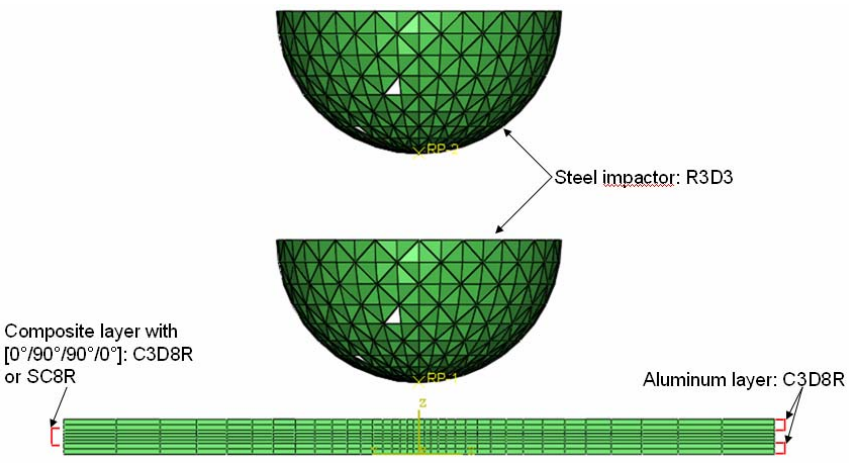

(c) Front View of Meshed FE Model

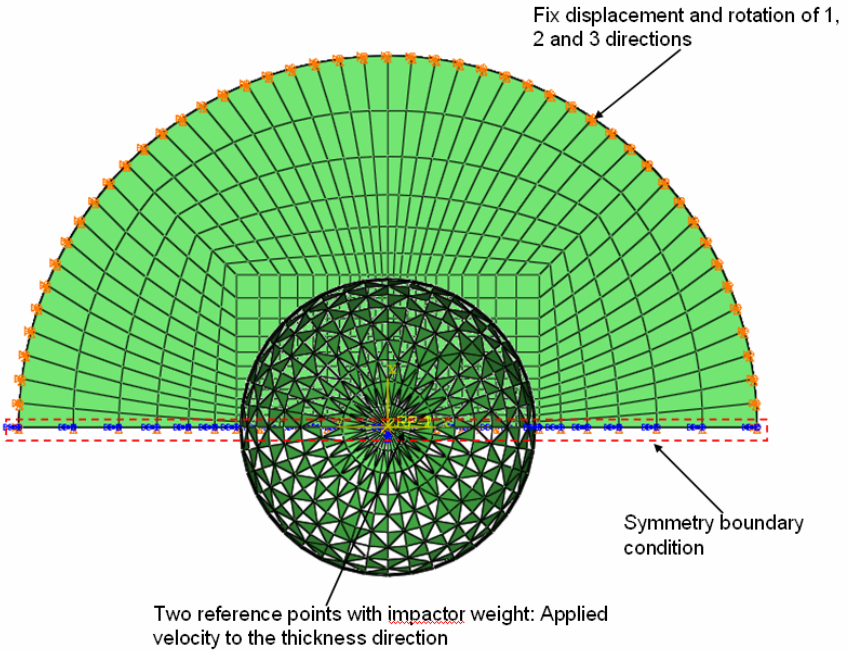

(d) Boundary Condition

Figure 9. Finite Element Model Geometry and Boundary Conditions (a) Experimental and Mesh Setup, (b) Cross View of Multiple Impacts, (c) Meshed Model of GLARE 5-2/1, and (d) Boundary Condition (Continued)

Table 3. Materials Properties Used in the FE Model [5 and 6]

Material	Parameter Values, GPa					
	E_{11}	E_{22}	G_{12}	G_{23}	ν_{12}	ν_{23}
Al 2024-T3	72.2	72.2	-	-	0.33	0.33
S2-Glass fiber	55	9.5	5.5	3	0.33	0.33

Table 4. Damage and Failure Properties Used in the FE Model [5 and 6]

Material	Parameter Values, MPa					
	σ_{ys}	X_t	X_c	Y_t	Y_c	S_{lt}
Al 2024-T3	320	-	-	-	-	-
S2-Glass fiber	-	2500	2000	50	150	75

3.2 NUMERICAL METHOD FOR GLARE IMPACT.

3.2.1 Three-Dimensional Modeling Rationale.

In typical FE analyses of composite structures, continuum shell elements are used to model the composite laminate. Continuum shells combine the planar nature of traditional shells with the 3D geometry of solid elements. As such, they offer a computationally efficient method for simulating systems that are globally 3D, but locally planar [28]. A multilayered, laminated composite structure is a good example of such a system. Because the mechanical properties of the composite laminate will, in general, vary between subsequent layers, the structure cannot be modeled with a single set of 3D solid elements; each layer must be represented by a unique element set. One layer of a unidirectional tape-based (i.e., not woven) composite typically has a thickness on the order of hundreds of microns, whereas the structure into which it is incorporated has geometry on the order of meters. Because of this large aspect ratio with respect to the laminate thickness, each layer can be assumed to be in a state of plane stress, with all through-thickness normal and shear components of the stress tensor (σ_{13}, σ_{23}, σ_{33}) assumed negligible in comparison to their in-plane counterparts (σ_{11}, σ_{22}, σ_{12}). Therefore, such a system is technically 3D, but approximately planar, and can be modeled with continuum shell elements.

This planar assumption is valid for most composite structures, but breaks down in several specific instances. The most obvious breakdown scenario is for a thick composite, in the limiting case for which the aspect ratio of the laminate width and/or length with respect to the thickness approaches unity. For this system, the laminate thickness is no longer negligible in comparison to the other dimensions, and interlaminar through-thickness stress tensor components must be considered. A second, and perhaps less obvious, scenario that prevents the use of continuum shell elements involves the nature of the boundary conditions present in the FE model. If the boundary conditions are applied such that nontrivial out-of-plane stresses arise in response to their application, then the system is no longer planar and continuum shells should not be used. Such is the case for the FE model under consideration in the present study, a rigid impactor incident upon the laminate in a direction aligned with the plane of material isotropy. In

this configuration, the direction of impact is parallel to the shell element normal vector, as shown in figure 10, and therefore will produce nontrivial through-thickness stresses. The plane stress assumption associated with continuum shell elements is inappropriate in this instance since it is in direct contradiction with the applied boundary conditions. Another important factor that precludes the usage of continuum shells in an impact simulation is the formation and propagation of delamination zones between the composite laminate. Since delamination is governed by the out-of-plane stress states in consecutive layers, incorporation of all stress tensor components is essential for accurate representation of postimpact delamination.

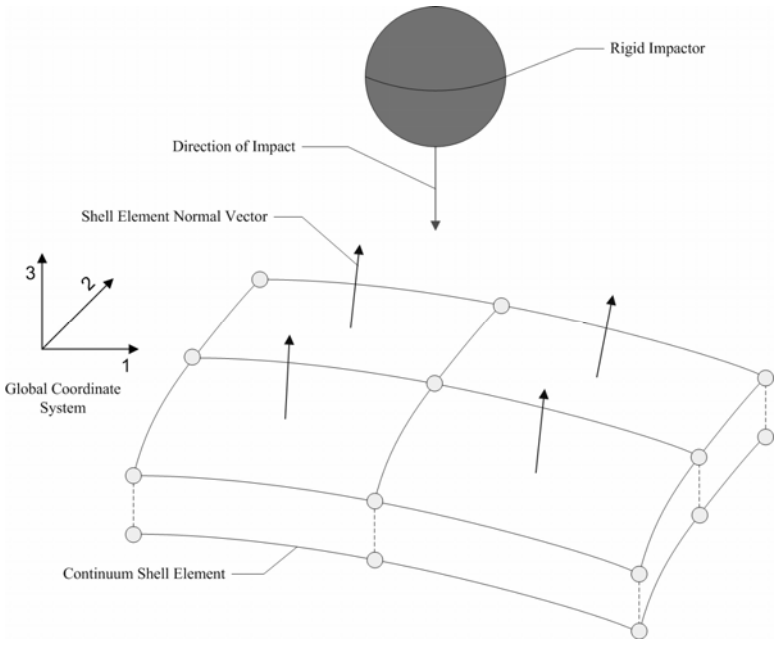

Figure 10. Continuum Shell Element Normal Vector Relation to Direction of Impact

3.2.2 Three-Dimensional Progressive Damage Model for Composite Materials.

Since shell elements are not appropriate for the impact simulation under consideration in the present study, a vectorized VUMAT was developed to simulate progressive damage and failure of composite materials with 3D solid elements. The methodology described herein applies to the ABAQUS/Explicit processor, but can be adapted to any displacement-based FE code. For each integration point in the model, the initiation of composite damage is defined using the well-known Hashin failure criteria, expressed in terms of the strain tensor (ε_{ij}) and experimentally measured strain at failure $\left(\varepsilon_{ij}^{init}\right)$ in equations 1-4 [25]. These failure strain values can be obtained from the more widely used failure stress measurements by taking the inner product with respect to the corresponding components of the material compliance tensor. The Hashin criteria allows for four modes of composite damage, illustrated in figure 11, with each mode represented by its own normalized failure variable (f^i).

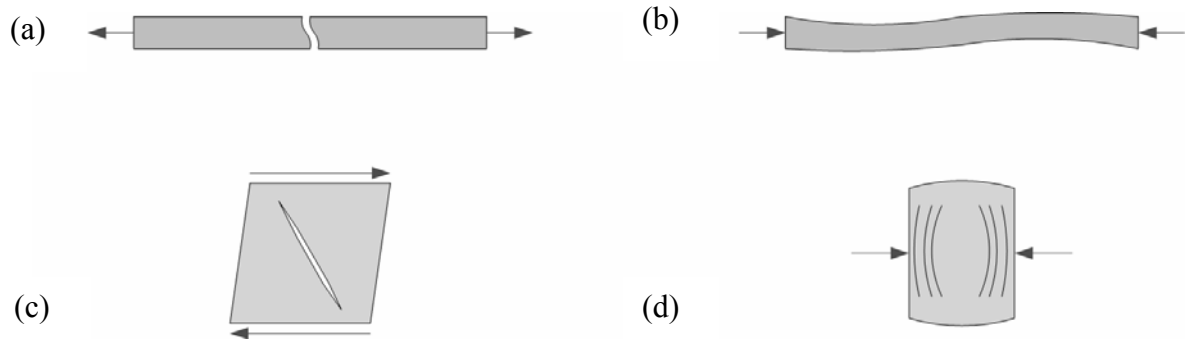

Figure 11. Hashin Composite Failure Modes (a) Fiber Tension, (b) Fiber Compression, (c) Matrix Tension/Shear, and (d) Matrix Compression

a. Fiber Tension Failure Mode ($\varepsilon_{11} > 0$)

$$f^{ft} = \left(\frac{\varepsilon_{11}}{\varepsilon_{11+}^{init}} \right)^2 + \frac{1}{\varepsilon_{12}^{init\ 2}} \left(\varepsilon_{12}^2 + \varepsilon_{13}^2 \right) \geq 1 \tag{1}$$

b. Fiber Compression Failure Mode ($\varepsilon_{11} < 0$)

$$f^{fc} = \frac{-\varepsilon_{11}}{\varepsilon_{11-}^{init}} \geq 1 \tag{2}$$

c. Matrix Tension/Shear Failure Mode ($\varepsilon_{22} + \varepsilon_{33} > 0$)

$$f^{mt} = \frac{1}{\varepsilon_{22+}^{init\ 2}} \left(\varepsilon_{22} + \varepsilon_{33} \right)^2 + \frac{1}{\varepsilon_{12}^{init\ 2}} \left(\varepsilon_{23}^2 + \varepsilon_{12}^2 + \varepsilon_{13}^2 - \varepsilon_{22}\varepsilon_{33} \right) \geq 1 \tag{3}$$

d. Matrix Compression Failure Mode ($\varepsilon_{22} + \varepsilon_{33} < 0$)

$$f^{mc} = \frac{1}{\varepsilon_{22-}^{init}} \left[\left(\frac{\varepsilon_{22-}^{init}}{2\varepsilon_{12}^{init}} \right)^2 - 1 \right] \left(\varepsilon_{22} + \varepsilon_{33} \right) + \frac{1}{\varepsilon_{12}^{init\ 2}} \left[\frac{\varepsilon_{22}^2 + \varepsilon_{33}^2}{2} + \varepsilon_{23}^2 + \varepsilon_{12}^2 + \varepsilon_{13}^2 \right] \geq 1 \tag{4}$$

When any of the above failure variables exceed unity, damage is defined to have occurred in the composite in that specific mode. It is important to note that this failure criterion includes all components of the strain tensor. The two-dimensional (2D) failure methodology employed by ABAQUS can be obtained from equations 1-4 by assuming a state of plane stress, which

eliminates the out-of-plane shear strains (ε_{13} and ε_{23}) and yields an explicit form for the out-of-plane normal strain (ε_{33}).

$$\varepsilon_{33} = \frac{1}{E_{22}}\left(\sigma_{33} - \nu_{23}\sigma_{22}\right) - \frac{\nu_{12}}{E_{11}}\sigma_{11} \tag{5}$$

In equation 5, the composite is assumed to be transversely isotropic, with the plane formed by the 2-3 axes representing the plane of isotropy. Because of the anisotropic nature of the material, all calculations performed by VUMAT are with respect to the local coordinate system. This provides a consistent general framework for any off-axis laminate whose local principal material directions are not aligned with those of the global system. Once failure has occurred in any given mode, the material response is evaluated using the damage mechanics approach proposed by Matzenmiller, et al. [29]. It is assumed that damage to the laminate in any of the four failure modes reduces the effective load bearing area of the composite. Since a physical reduction of area is not practical in an FE simulation, the damage mechanics area reduction is accomplished via modification of the material's elastic constants using an internal damage state variable (w^i). As a consequence, damage in the material at a given point reduces the tensorial stress components, typical of a strain-softening constitutive model. Once any Hashin failure variable, equations 1-4, exceeds a value of one, the internal damage state of the material follows a rate-based progression model, similar to that proposed by Iannucci, et al. [30]. The rate of propagation of damage in the material in all four modes at the current time step ($\dot{w}^i\ (t + \Delta t)$) depends on the damage state variable at the previous time step ($w^i(t)$) and the current strain state ($\varepsilon(t + \Delta t)$), as well as constant damage rate terms due to crack nucleation and growth (Ω_0 and Ω_1, respectively). The explicit form for the damage propagation rate is provided in equation 6, where the superscript (i) corresponds to each unique Hashin failure mode in equations 1-4.

$$\dot{w}^i(t+\Delta t) = \Omega_0 + \Omega_1 w^i(t)\left[\left(\frac{\varepsilon_{kl}(t+\Delta t)\varepsilon_{kl}(t+\Delta t)}{\varepsilon_{mn}^{init}\varepsilon_{nm}^{init}\left(1-w^i(t)\right)^2}\right) - 1\right] \tag{6}$$

In equation 6, it is important to note that the strain state at failure (ε_{ij}^{init}) is modified by the previous damage state ($w^i(t)$). This ensures that the "threshold" strain value required for composite damage decreases with increasing damage density. In other words, following the initial onset of damage, the energy required for crack formation is inversely proportional to the number of cracks in the material at a given time. Since the time step between successive increments is very small (on the order of picoseconds for an impact duration of 10 milliseconds), the degradation rate of equation 6 is assumed to have a linear form. Thus, the damage state variable at the current time step ($w^i(t+\Delta t)$) can be obtained from the previous damage state and the damage growth rate.

$$w^i\left(t+\Delta t\right) = w^i(t) + \dot{w}^i(t+\Delta t)\Big)\Delta t$$
$$w^i \in [0,1) \tag{7}$$

In this case, the damage state variables must be bounded by an upper limit less than one to prevent computational issues arising during inversion when they are used to degrade the composite elastic constants. Damage in a fiber-related mode (f^{ft}, f^{fc}) results in a decrease in the modulus in the local fiber direction (E_{11}) along with in-plane shear modulus and Poisson's ratio (G_{12} and ν_{12}, respectively). Conversely, damage in a matrix-specific mode (f^{mt}, f^{mc}) produces degradation of all elastic constants except for the modulus in the local fiber direction. Switching from a tensorial representation to a reduced index matrix form, the composite material compliance ($S(t)$) at any time step can be found from equations 8 and 9, where the linear elastic material response for undamaged laminate is obtained by setting all damage state variables to zero.

$$S(t)=\begin{bmatrix} 1/d_1E_{11} & -1/d_3\left(\nu_{12}/E_{11}\right) & -1/d_3\left(\nu_{12}/E_{11}\right) & 0 & 0 & 0 \\ -1/d_3\left(\nu_{12}/E_{11}\right) & 1/d_2E_{22} & -1/d_2\left(\nu_{23}/E_{22}\right) & 0 & 0 & 0 \\ -1/d_3\left(\nu_{12}/E_{11}\right) & -1/d_2\left(\nu_{23}/E_{22}\right) & 1/d_2E_{22} & 0 & 0 & 0 \\ 0 & 0 & 0 & 1/d_3G_{12} & 0 & 0 \\ 0 & 0 & 0 & 0 & 1/d_3G_{12} & 0 \\ 0 & 0 & 0 & 0 & 0 & 2(1+d_2V_{23})/d_2E_{22} \end{bmatrix} \tag{8}$$

$$\begin{aligned} d_1 &= (1-w_{ft})(1-w_{fc}) \\ d_2 &= (1-w_{mt})1-w_{mc}) \\ d_3 &= (1-w_{ft})(1-w_{mt})(1-w_{mc}) \end{aligned} \tag{9}$$

Note that in the above constitutive model, the transversely isotropic nature of the material is retained following the onset of damage. Once the material compliance is established at the current time step, the current stress state in reduced index form can be determined from equations 6-9 through inversion. For non-zero damage state variables, it is evident that the stresses carried by a damaged element will be smaller than those of the corresponding undamaged element, as required by the damage mechanics assumption.

$$\begin{aligned} \bar{\sigma}(t+\Delta t) &= C(t+\Delta t)\bar{\varepsilon}(t+\Delta t) \\ C(t+\Delta t) &= S^{-1}(t+\Delta t) \end{aligned} \tag{10}$$

Specific implementation of the damage mechanics procedure provided in equations 1-10 in the ABAQUS/Explicit processor is outlined via flowchart in figure 12. In this model, the compliance of FMLs was calculated first and then converted to stiffness under undamaged

scenarios. The strain-based failure criteria were determined and checked at each step of integration by updating strain and stress states. The starting point of laminates failure was obtained through Hashin failure variables. If an element met the failure criteria, it would be removed from the mesh.

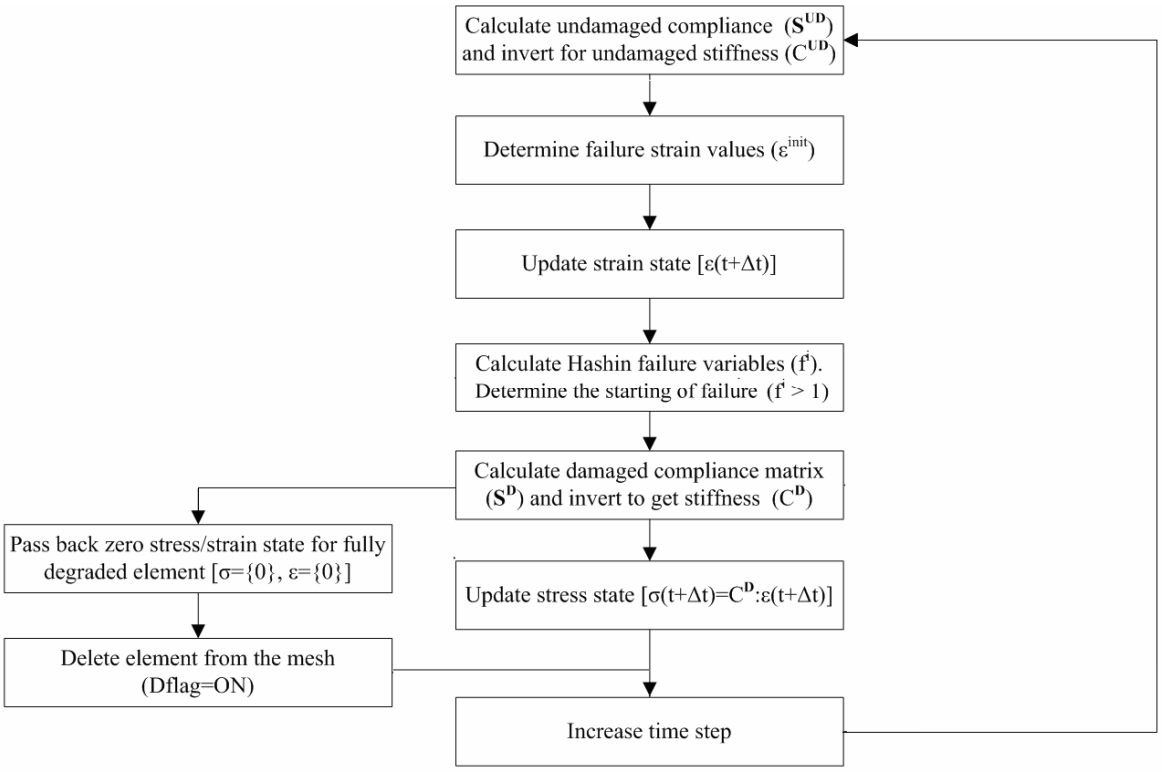

Figure 12. Composite Progressive Damage VUMAT Flowchart for the ABAQUS/Explicit Processor

3.2.3 Energy Dissipation Due to Damage.

As a consequence of the progressive failure methodology covered in the previous section, once the constitutive matrices are degraded, the material cannot revert to the undamaged state. Thus, energy is dissipated by the material due to damage formation and growth. The amount of this dissipated energy is an important quantity in impact simulations, since it represents the ability of the material to absorb the kinetic energy of the theoretically rigid impactor. If thermal effects on the material are neglected, the global balance of energy for the continuum body schematically illustrated in figure 13 can be established from the specified body forces, tractions, and the changes in kinetic and internal energy.

$$\int_{\partial\Gamma} v_i T_i dS + \int_{\Gamma} v_i F_i dV = \partial/\partial t \left[\int_{\Gamma} \left(\tfrac{1}{2} \rho v_i v_i + \rho U \right) dV \right] \tag{11}$$

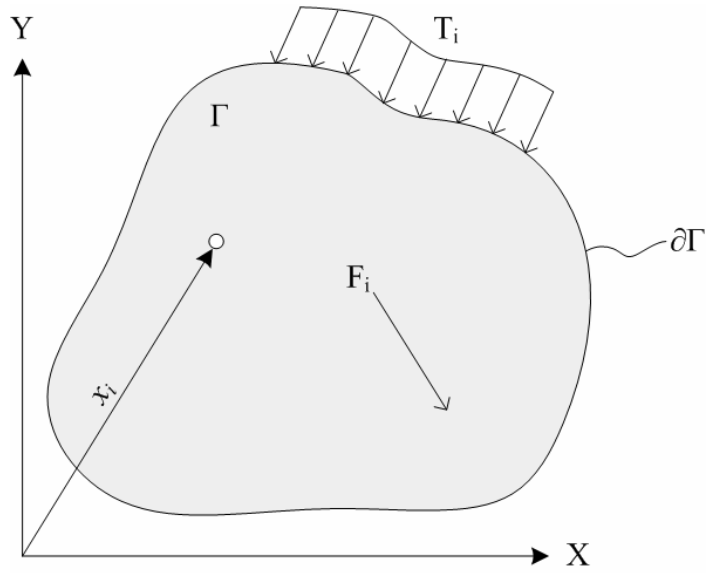

Figure 13. General Schematic for Energy Dissipation of a Continuum Body

Applying the divergence theorem to the surface integral in the above equation and assuming that the continuum body in figure 13 is at an equilibrium state, the time-integrated internal energy (W) can be expressed as

$$W = \int_{\Gamma} \rho U dV = \int_0^t \int_{\Gamma} \sigma_{ij} \dot{\varepsilon}_{ij} dV \tag{12}$$

The energy dissipated by the continuum body due to damage formation can be determined from equation 12 by examining the response of the continuum body to a constant strain field (ε^*). Considering two material states, one damaged and the other undamaged (denoted by "D" and "UD," respectively), it is evident that the stress required to deform the material by ε^* will not be the same in both cases due to the strain-softening nature of the constitutive model. The energy dissipated by the continuum body is equal to the difference in internal energy between the two states

$$\Delta W = W_{UD} - W_D = \int_0^t \int_{\Gamma} \sigma_{ij}^{UD} \dot{\varepsilon}_{ij}^* dV - \int_0^t \int_{\Gamma} \sigma_{ij}^{D} \dot{\varepsilon}_{ij}^* dV \tag{13}$$

Since the strain is required to be identical in both cases, an expression linking the damaged and undamaged stress states can be determined from the constitutive relations

$$\begin{aligned} \varepsilon_{ij}^* &= S_{ijkl}^D \sigma_{kl}^D = S_{ijkl}^{UD} \sigma_{kl}^{UD} \\ \therefore \sigma_{kl}^{UD} &= C_{ijkl}^{UD} S_{ijmn}^D \sigma_{mn}^D \end{aligned} \tag{14}$$

Inserting the above expression into the internal energy integral equation produces the following result for the dissipated energy, where (I_{klmn}) represents the fourth-order identity tensor

$$\Delta W = \int_0^t \left[\int_\Gamma \left(\left\{ C_{ijkl}^{UD} S_{ijmn}^{D} - I_{klmn} \right\} \sigma_{mn}^{D} \right) \dot{\varepsilon}_{kl} dV \right] \tag{15}$$

In the practical implementation of the progressive damage procedure into the FE model, this integral is evaluated in a piecewise fashion due to the extremely small time interval between successive steps. The degradation scheme of the composite's progressive damage is shown in table 5, and the cracking energy of GLARE laminates is shown in table 6.

Table 5. Degradation Scheme for Composite Progressive Damage

Failure Mode	Degraded Elastic Material Properties				
	E_{11}	E_{22}	v_{12}	v_{23}	G_{12}
Fiber tension	x		x		x
Fiber compression	x		x		x
Matrix tension/shear		x	x	x	x
Matrix compression		x	x	x	x

Table 6. Minimum Cracking Energy and Perforation Energy for GLARE Laminates [7]

Materials	Thinness (mm)	Areal Density (kg/m^2)	Minimum Cracking Energy (J)	Perforation Energy (J)
Al 2024-T3	1.6	4.45	18.1	33.4
GLARE 5-2/1	1.562	3.74	16.3	34.5

4. ANALYTICAL PREDICTION MODEL OF MSD FATIGUE CRACK GROWTH IN FIBER-METAL LAMINATES.

To investigate the crack growth behavior of GLARE laminates with MSD, an analytical crack growth model was proposed to calculate the crack growth rates. A flowchart is used to describe this prediction approach, as shown in figure 14.

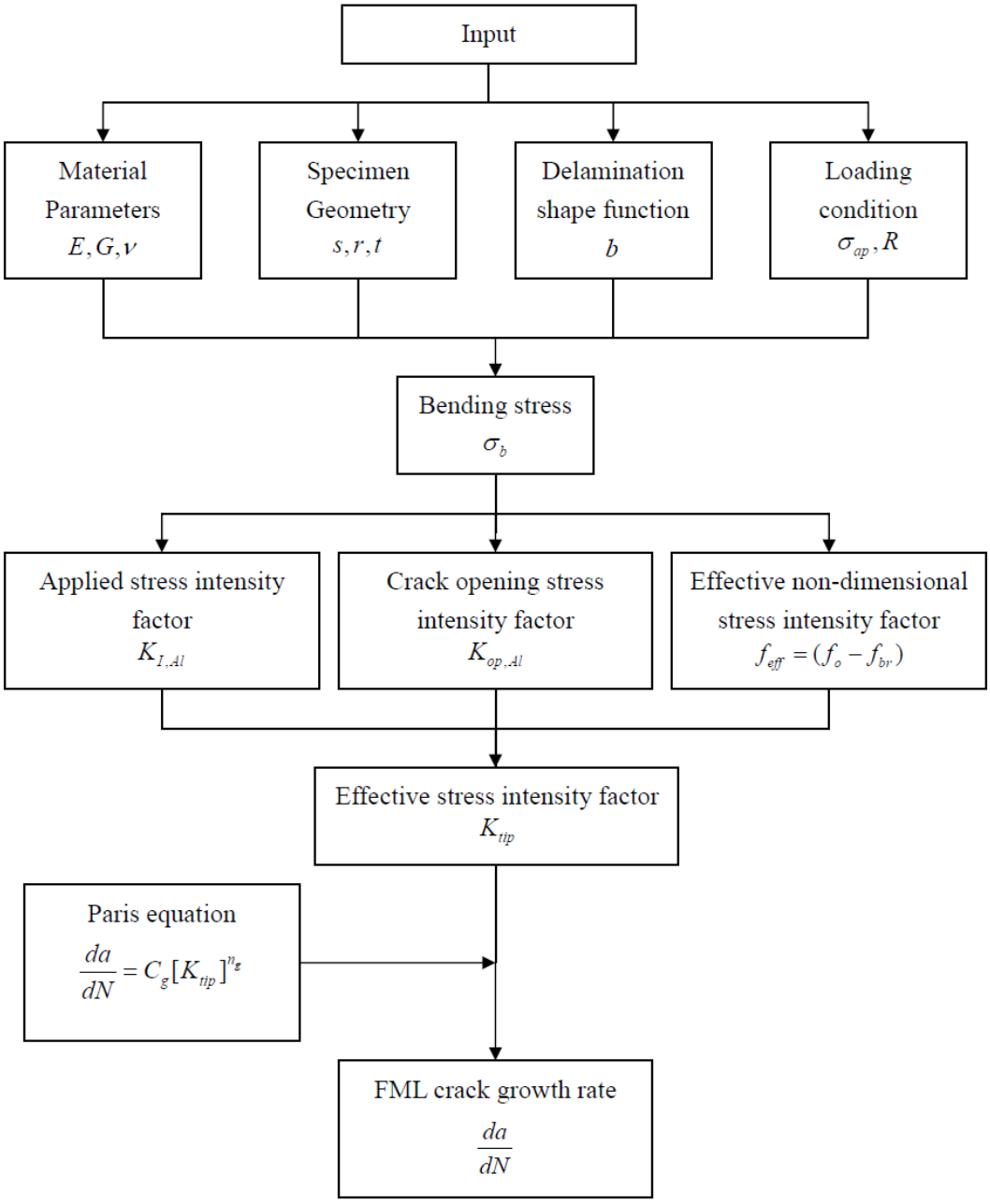

Figure 14. Flowchart of Crack Growth Prediction Approach for GLARE Laminates

4.1 CLASSIC LAMINATION THEORY.

The stress levels in each layer of FMLs are calculated through the 2D class lamination theory in *x*-*y* coordinates, which is written as [31]

$$\sigma_{\phi,l} = \begin{bmatrix} \sigma_x \\ \sigma_y \\ \tau_{xy} \end{bmatrix}_{\phi,l} = Q_{\phi,l} \left[Q_{lam}^{-1} \sigma_{lam} + \Delta T \left(\begin{bmatrix} \alpha_x \\ \alpha_y \\ 0 \end{bmatrix}_{lam} - \begin{bmatrix} \alpha_x \\ \alpha_y \\ 0 \end{bmatrix} \right) \right] \tag{16}$$

where the stiffness matrix is expressed as

$$Q = \begin{bmatrix} \dfrac{E_x}{1-\nu_{xy}\nu_{yx}} & \dfrac{\nu_{xy}E_y}{1-\nu_{xy}\nu_{yx}} & 0 \\ & \dfrac{E_y}{1-\nu_{xy}\nu_{yx}} & 0 \\ sym & & G_{xy} \end{bmatrix} \tag{17}$$

The coordinates *x* and *y* are parallel and perpendicular to the loading direction, respectively. When the stiffness matrix is under off-axis angle ϕ

$$Q_\phi = \Phi Q \Phi^T \tag{18}$$

where Φ is the off-axis matrix and is expressed as

$$\Phi = \begin{bmatrix} \cos^2(\phi) & \sin^2(\phi) & 2\cos(\phi)\sin(\phi) \\ \sin^2(\phi) & \cos^2(\phi) & -2\cos(\phi)\sin(\phi) \\ -\cos(\phi)\sin(\phi) & \cos(\phi)\sin(\phi) & \cos^2(\phi)-\sin^2(\phi) \end{bmatrix} \tag{19}$$

Using the lamination theory above, the actual stress levels in the Al and fiber layers were obtained and plotted as a function of cycle time and are shown in figure 15. Clearly, the stress level in the Al layer is higher than the applied stress due to the difference in the stiffness of the S2-glass/prepreg and metal layers. Due to the mismatch of thermal expansion coefficients in different constituents, the curing stress would also raise the stress level in the Al layer.

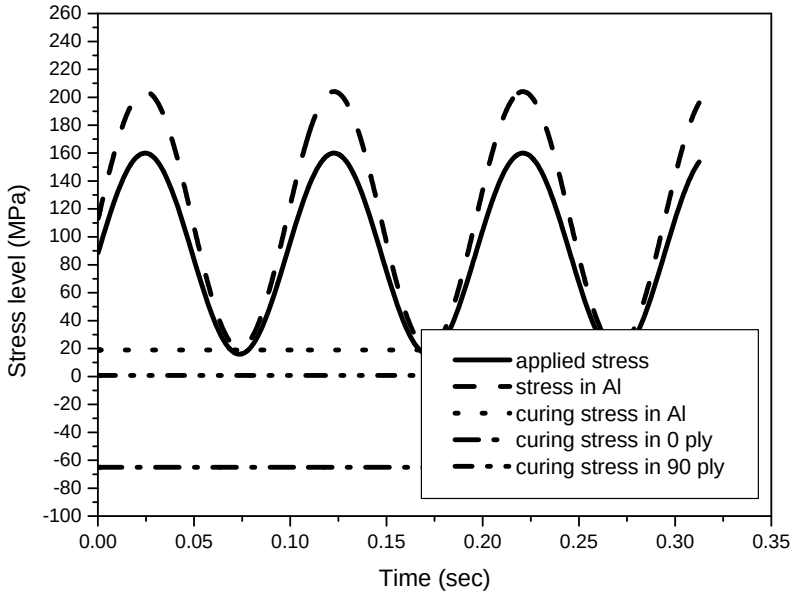

Figure 15. Typical Stress Distribution in Al Layer and Curing Stress in Each Layer of GLARE Laminate Under Cyclic Loading at Room Temperature With a Frequency of 10 Hz (The maximum applied stress was 160 MPa with a stress ratio of 0.1 [32].)

4.2 SECONDARY BENDING EFFECT.

A secondary bending will occur in a laminate if the configuration is unsymmetrical, which results in a shift of the neutral line. The thickness of a GLARE 3-3/2 laminate is thin, and this allows a beam theory to be used to analyze the stress variation in a laminate caused by the secondary bending. If the secondary bending is absent, the neutral axis will not be displaced and no additional stress will be incurred. In the presence of the eccentricity of neutral lines, as shown in figure 16, the neutral axis shifts and results in the introduction of bending stress. To calculate the magnitude of bending stress, the displacement of the neutral line needs to be obtained first for further consideration of stress level variation in a laminate. Using the neutral line model [33], the bending moment, M_x, is expressed as

$$M_x = P \cdot z \tag{20}$$

where P is the applied force in Newtons, and w is the displacement in unit of *mm.* The symbol z denotes the thickness of a laminate. By using the beam theory for a thin laminate, the bending moment can be written as

$$M_x = E * I \frac{d^2 w}{dx^2} \tag{21}$$

For plane bending, $E^* = E/(1-\nu^2)$. A laminate is divided into surface metal cracked (L_{cr}, $i = 1$) and uncracked (L_{un}, $i = 2$) parts, respectively. Then, equating equations 5 and 6, the differential equation yields

$$(d^2 w_i/dx_i^2) - (P/E^*I)_i \, w_i = 0, \; i = 1,2 \tag{22}$$

where E is the stiffness, and I is the moment inertia of a laminate. The general solution for the displacement of the neutral line is expressed as

$$w_i = sinh(\eta_i x_i) + \cosh(\eta_i x_i) \tag{23}$$

and

$$\eta_i = \sqrt{P/E^*I)_i} \tag{24}$$

For surface-cracked GLARE 3-3/2 laminates, the boundary conditions are defined as

$$x_1 = 0, \; w_1 = 0 \tag{25}$$

$$w_1(x_1 = L_1) = w_2(x_2 = 0) + e, \; e = 0.5 \, t_{Al} \tag{26}$$

(e = eccentricity of the neutral line in cracked and uncracked parts)

$$dw_1(x_1 = L_1)/d\,x_1 = d\,w_2(x_2 = 0)/dx_2 \tag{27}$$

$$x_2 = L_2, \; d\,w_2(x_2 = L_2)/\,dx_2 = 0 \tag{28}$$

Hence, the bending stress in the thickness direction of a laminate can be obtained with

$$\sigma_b = (Mw/I)z = (d^2 w/\,dx^2)E^*z \tag{29}$$

Using equations 8 through 21, the actual stress level in layer l of a laminate is able to be obtained as a combination of applied stress and bending stress. That is

$$\sigma_b = \sigma_{l,lam} + \sigma_b(x) \tag{30}$$

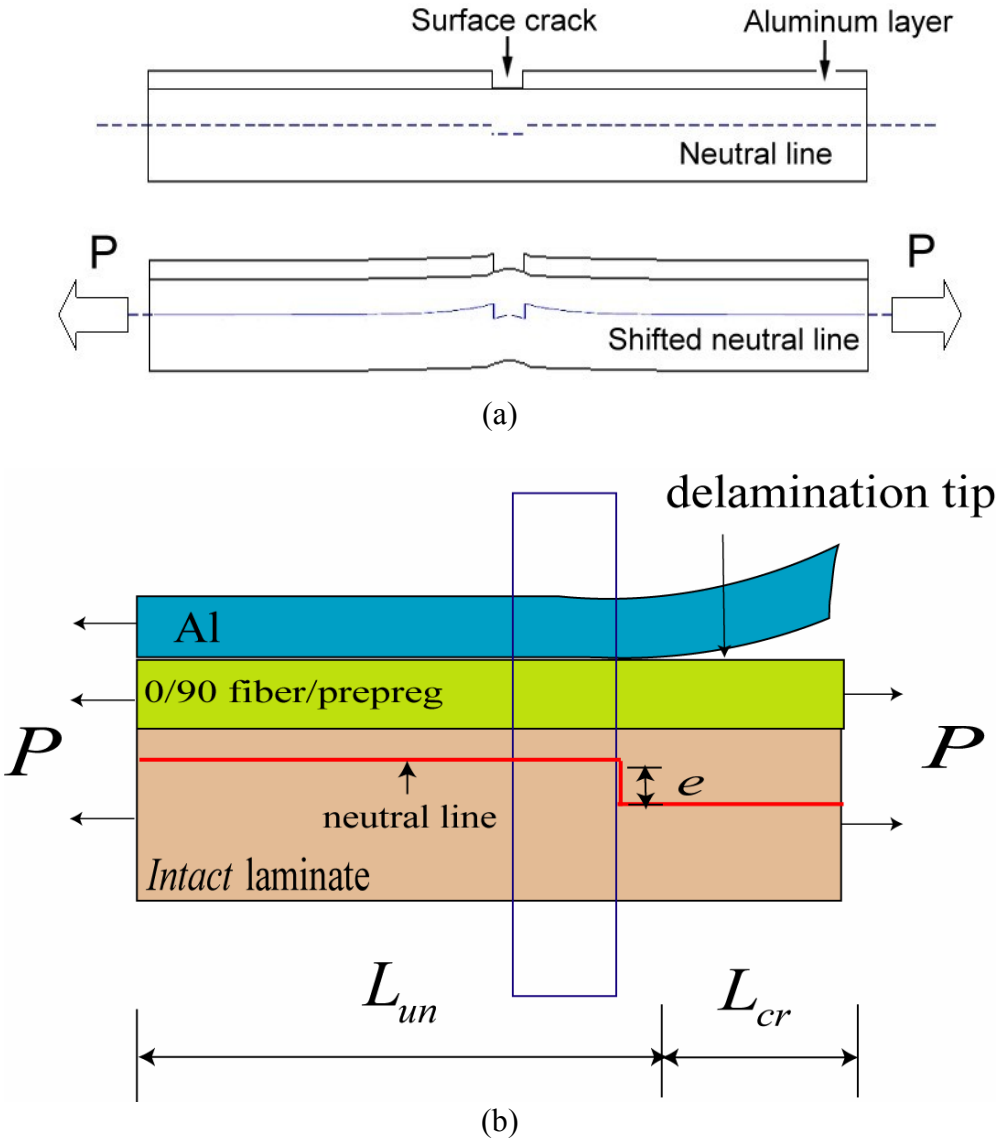

Figure 16. A Surface-Cracked FML Subjected to Tensile Load (a) Neutral Line Shift due to Unsymmetrical Configuration and (b) Eccentricity in Neutral Lines for FMLs

The deflection along the loading direction for a different lay-up sequence of GLARE 3 laminates is shown in figure 17. As the thickness of laminates increases, the magnitude of deflection decreases significantly. Clearly, the secondary bending would slightly change the neutral line position in GLARE 3-3/2 (Al/0/90/Al/0/90/Al) laminates because of the neutral line's eccentricity. As the crack advances, the deflection of the neutral line would gradually increase. The calculated bending stresses for GLARE 3-3/2, GLARE 3-4/3, and GLARE 3-5/4 were plotted as a function of crack length and are shown in figure 18. The maximum bending stress is around 15 MPa, 4 MPa, and 2 MPa for GLARE 3-3/2, 4/3, and 5/4, respectively. Hence, the secondary bending effect is not very significant to affect the stress level in the surface-cracked metal layer of GLARE 3-4/3 laminates and up.

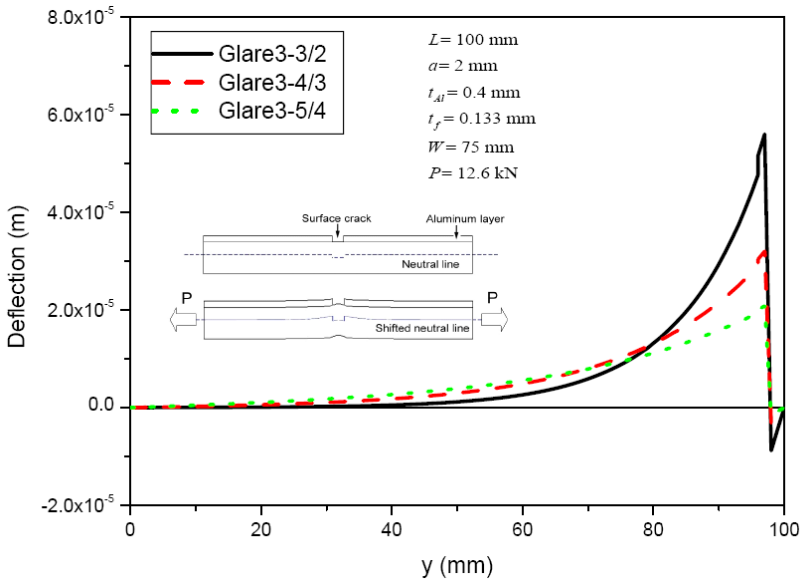

Figure 17. Deflection of the Neutral Line in GLARE Laminates Along Loading Direction

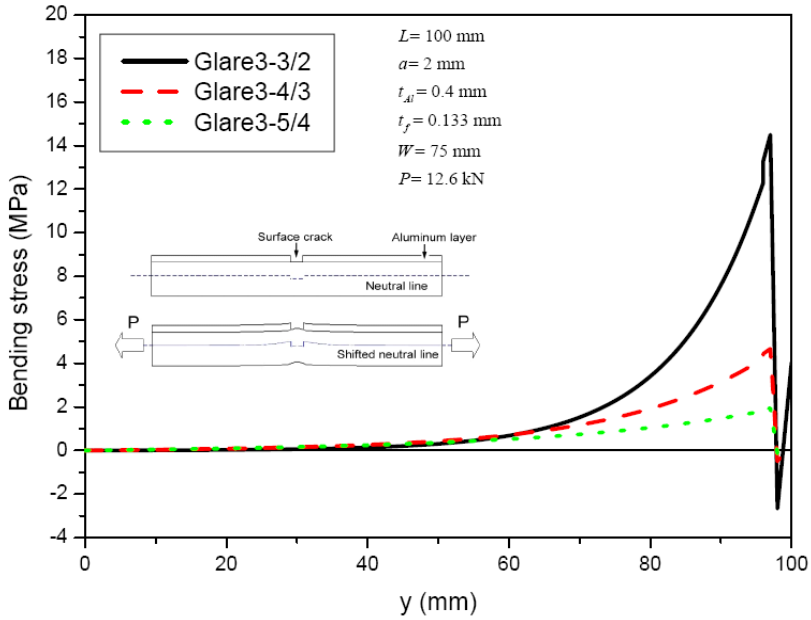

Figure 18. Bending Stress Distribution in Metal Layer of GLARE Laminates Along Loading Direction

The maximum bending stress occurs at the surface metal layer at the delamination tip along the loading direction. The averaged bending stress through-the-thickness direction is used in certain layers.

4.3 BRIDGING STRESS DISTRIBUTION.

In a GLARE laminate with MSD, the crack growth is impeded by the fiber-bridging mechanism so that the crack opening in the metal layers is restrained by the fiber-bridging stress. Guo and Wu established a theoretical prediction model for crack growth for center-cracked FMLs [34 and 35]. The configuration of the bridging stresses along the crack length for a center-cracked geometry in FMLs is shown in figure 19(a), which includes the crack opening contour under the maximum applied load with the corresponding closing bridging stress acting on the delamination boundary. Based on the crack displacement relation, Guo and Wu [34 and 35] incorporated the bridging traction into a theoretical prediction model for crack growth in GLARE laminates. This relation had been adopted by other authors in crack growth modeling of GLARE and boron/glass/Al FMLs [36-38]. With the presence of secondary bending, the bending moment needs to be considered as shown in figure 19(b) for bridging stress calculation.

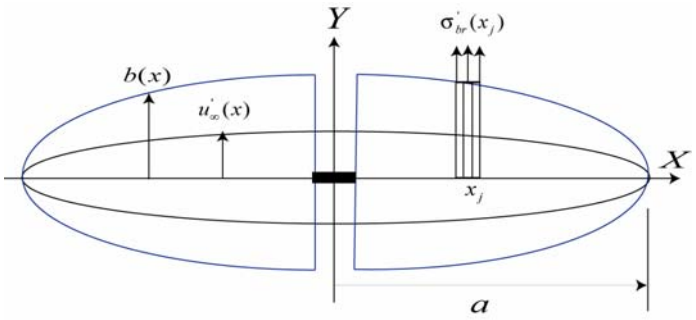

(a)

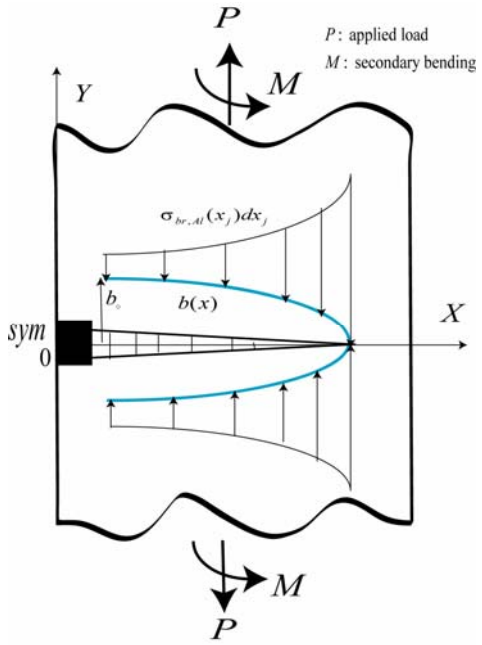

(b)

Figure 19. Bridging Stress in FMLs (a) Combination of Applied Load and Secondary Bending Moment and (b) Crack Opening and Closing Profiles

The crack opening in the Al layers of FMLs can be written as the crack opening due to remote applied stresses in the Al layers and the crack closing bridging stresses as result of the intact fiber layers [35]. That is

$$u_{fml,Al} = u_{\infty}(x) - u_{br}(x) \tag{31}$$

The effects of crack opening and closing bridging stress balance the deformation of fibers and adhesives. In other words, the crack opening in the Al layers is identical to the elongation and deformation of the fiber/prepreg layers in the crack opening area [35]. That is

$$u_{fml,Al} = \delta_f(x) + \delta_{pp}(x) + \delta_{Al} \tag{32}$$

where δ_f and δ_{pp} denote the deformation in the fiber and adhesive layers, respectively, and u_{∞} and u_{br} denote the crack-opening displacement due to the remote applied stress and fiber-bridging stress, respectively. δ_{Al} is the metal deformation, which is not considered owing to its negligible value. The subscripts f and Al represent the fiber and Al layers, respectively.

In a specimen containing multiple center cracks, the crack-opening displacement in the metal layer caused by uniform applied stress and secondary bending under plane stress condition is expressed in reference 39 as

$$u_{\infty}(a,x) = 2\frac{\sigma_{Al}}{E_{Al}}\sqrt{a^2 - x^2} \tag{33}$$

where x is the distance from the crack center, and E_{Al} is the elastic modulus of the Al layer. The stress level in the Al layer is determined by the applied stress and secondary bending. If the secondary bending effect is considered, the bending stress should be superimposed.

The crack-opening displacement, u_{br}, caused by the fiber-bridging stresses can be calculated through a series of crack-opening displacements induced by the point loads acting on position x_j of the crack flanks, as shown in figure 19(b), that is

$$u_{br} = \int_0^a u(x,x_j)dx_j \quad \text{for } 0 \le x \le a \tag{34}$$

The crack-opening displacement $u(x,x_j)$ caused by a point load acting on arbitrary positions is expressed as [39 and 40], if $x < x_j$

$$u(x,x_j) = \frac{4}{\pi E}\left(\tanh^{-1}\sqrt{\frac{a^2 - x_j^2}{a^2 - x^2 + b^2}} + \frac{\frac{1}{2}(1+\nu)b^2}{x_j^2 - x^2 + b^2}\sqrt{\frac{a^2 - x_j^2}{a^2 - x^2 + b^2}} \right)\sigma_{br}(x_j)dx_j \tag{35}$$

If $x > x_j$, then replace $x = x$ and $x_j = x$ in equation 35, where E is the elastic modulus, ν is the Poisson ratio of laminate, and s is the spacing between two open holes.

Concerning the fiber/layer deformation, it should be noted that a superposition is used for deformation induced by the stresses in the fibers and by the bridging stresses. In the presence of delamination, the elongation of the fiber layer over the crack opening area is expressed as

$$\delta_f(x) = \varepsilon_f(x) b(x) = \frac{\sigma_f + \sigma_{br}}{E_f} b(x) \tag{36}$$

where ε_f and E_f are the strain and elastic modulus of the fiber layers, and σ_f and σ_{br} are the stress level and bridging stress in the fiber layers, respectively. $b(x)$ is an arbitrary shape function for delamination. The parabolic and triangular shape functions are expressed as

$$b(x) = b_\circ \sqrt{\frac{(a-x)}{(a-r)}} \tag{37}$$

and

$$b(x) = b_\circ \frac{(a-x)}{(a-r)} \tag{38}$$

where $b_\circ$ is the initial delaminating length at the notch root.

The shear deformation as a function of the shear stress at the Al/prepreg interface is expressed as

$$\delta_{pp} = \gamma t_f = (\frac{\tau_f}{G_f}) t_f \tag{39}$$

Based on this expression and with linear shear deformation analysis, the prepreg shear deformation in FMLs with cross-ply prepreg layers is derived and expressed as [41]

$$\delta_{pp} = C_{corr} \sigma_{Al} t_{Al} \frac{t_f}{G_f} \sqrt{(\sum \frac{G_f}{t_f}) \times (\frac{1}{2 n_{Al} t_{Al} E_{Al}} + \frac{1}{\sum n_f t_f E_f})} \tag{40}$$

where the subscripts Al and f denote aluminum and fiber layer, respectively. The symbol t represents the thickness of each layer. If the small delamination length is considered, a correction factor, C_{corr}, needs to be used, as presented in reference 40.

Similar to a governing equation in reference 34, the fiber-bridging stress σ_{br} is derived as

$$\sigma_{br} = M_j^{-1} N \tag{41}$$

where

$$N = u_{\infty}(x) - \delta_{pp}(x) - \frac{\sigma_f}{E_f} b(x) \tag{42}$$

and

$$M_j = \sum \frac{u_{br}(x_i, x_j)\Delta x_j}{\sigma_{br}(x_j)} - \frac{b(x_i)}{E_f}\delta(i, j) \tag{43}$$

$$\delta(i, j) = \begin{cases} 1, \text{if } i \neq j \\ 0, \text{if } i = j \end{cases} \text{ Kronector factor} \tag{44}$$

This governing equation can be solved using any programming tool. The bridging traction acts on the surface of the metal layer to impede the crack growth, and the bridging stress at the crack surface of the Al layer, $\sigma_{br,Al}$, is obtained using the relationship of force balance in the FMLs. Thus, the bridging stress at the crack face of the metal layers in a cross-ply FML is expressed as

$$\sigma_{br,Al} = \left(\frac{n_{0,f} t_{0,f} + n_{90,f} t_{90,f}}{n_{Al} t_{Al}}\right) M_j^{-1} N \tag{45}$$

In the application of weight function for the SIF calculation, the stress distribution on the crack face can be known by using the same governing equation. The metal-bridging stress at the crack surface under the unit applied load in the laminate as a function of crack length was plotted and is shown in figure 20. Observably, the bridging stress is close to uniform along the crack length, and the highest value is at the crack tips.

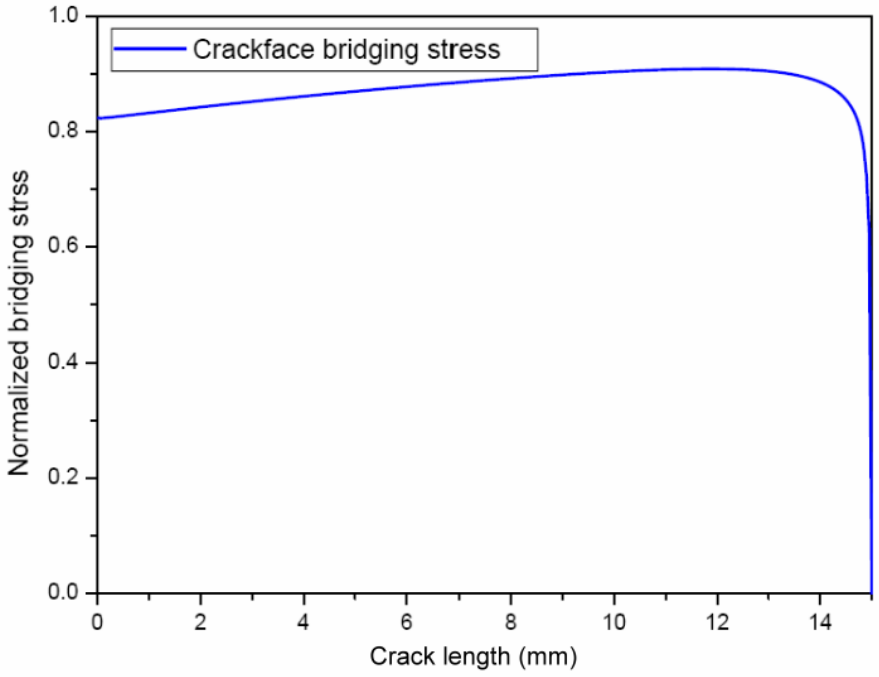

Figure 20. Bridging Stress Distribution at the Crack Face in GLARE 3-3/2 Specimens Under Unit Applied Load in FMLs With an Applied Stress Ratio of 0.05

4.4 WEIGHT FUNCTION FOR SIF CALCULATION.

In the presence of multiple-site fatigue damage, the geometry and configuration need to be taken into account while calculating the far-field SIF in the metal layer of GLARE laminates. Using the weight function approach, the effects of geometry and configuration of the test specimens can be properly incorporated. The direction of crack propagation is perpendicular to the loading direction, therefore, only mode I SIF needs to be considered.

For one-dimensional, through-thickness crack propagation, the SIFs associated with symmetric mode I loading can be calculated by applying the concept of weight function. That is [42]

$$K = \int_0^a \sigma(x) m(a,x) dx \tag{46}$$

where $\sigma(x)$ is the stress distribution on the crack face, and $m(a,x)$ is the weight function. In equation 21, the SIF can be expressed as [42]

$$K = f\sigma\sqrt{\pi a} \tag{47}$$

where f is the nondimensional SIF, and a is the crack length starting from an open hole. The weight function for a one-dimensional crack can be expressed as [42]

$$m(a,x) = \frac{E'}{f_r \sigma \sqrt{\pi a}} \frac{\partial u_r(\bar{a},\bar{x})}{\partial \bar{a}} \tag{48}$$

where E' is the elastic modulus, $u_r(\bar{a},\bar{x})$ is the displacement of the crack face relative to the plane of symmetry, and f_r is the reference SIF. To apply this relation, the distributions of the applied load have to be calculated from the relation between the load and the crack-opening displacement. For convenience of calculation, normalization is applied to crack length a, coordinates x, and crack-opening displacement u with respect to s. That is

$$\bar{a} = \frac{a}{s} \text{ and } \bar{x} = \frac{x}{s}$$

4.5 FORMATION OF EFFECTIVE SIF.

As FMLs are subjected to cyclic load, crack propagation is driven by the far-field applied load and retarded by the bridging stress on the delamination boundary. For a crack to continue to propagate, the driving force needs to overcome residual strength-induced crack closure while the crack growth is bridged by the bridging mechanism. The effective SIFs of FMLs at the crack tips need to incorporate the effects from applied load, crack closure, and bridging stresses. Also, the presence of residual stress in FMLs needs to be taken into account in fatigue crack growth in terms of the crack opening stress.

Following the definition of effective SIF used for FMLs in reference 34, the effective SIF of an FML can be expressed as

$$K_{tip} = (K_{I,Al} - K_{op,Al}) f_{\text{eff}} \tag{49}$$

where $K_{I,Al}$ is the mode I SIF in the Al layer, $K_{op,Al}$ is the crack opening SIF in the Al layer, and f_{eff} is the effective nondimensional SIF. The effective nondimensional SIF is defined as

$$f_{\text{eff}} = (f_o - f_{br}) = f_o(1 - \beta_f) \tag{50}$$

and

$$\beta_f = \frac{f_o}{f_{br}} \tag{51}$$

where f_o is attributed to the unit applied load, and f_{br} is attributed to the corresponding bridging stress. The nondimensional β_f is the fiber-bridging factor. Equating these equations, the effective SIF at the crack tips can be rewritten as

$$K_{tip} = (K_{I,Al} - K_{op,Al})(1-\beta_f) f_o \tag{52}$$

A nondimensional fiber-bridging factor, β_f, of zero is the crack growth behavior for monolithic Al alloy, and f_o is a geometrical correction factor. As the bridging effect increases, as described in β_f, the effective SIF is modulated by the fiber-bridging factor. As a result, the crack growth rate is reduced by the fiber-bridging mechanism in FMLs. If the nondimensional bridging factor, β_f, is equal to one, then the crack growth in FMLs is fully bridged. Each item in the effective SIF will be discussed in the following sections.

4.5.1 Far-Field SIF.

For specimens subjected to unidirectional fatigue load, the crack path in the metal layer is perpendicular to the loading direction, only mode I SIF is considered. Taking into account the effect of bending and applied stress in the metal layer, superposition is used to calculate the actual stress level in the metal layer. Therefore, the model I SIF in the Al layer is expressed as [39]

$$K_{I,Al} = (\sigma_{Al} + \sigma_{Al}^{b})\sqrt{\pi a} \tag{53}$$

where σ_{Al} is the stress level in the Al layer, σ_{Al}^{b} is the stress in the Al layer caused by secondary bending effect, and a is the total crack length in FMLs. If there is no secondary bending, then the bending stress is zero. Different scenarios of crack interaction due to the presence of MSD in Al alloy can be found in reference 12.

4.5.2 Crack-Opening SIF.

The crack-opening SIF is expressed as [21]

$$K_{op} = \sigma_{Al,op}\sqrt{\pi a} \tag{54}$$

where $\sigma_{Al,op}$ is the crack-opening stress in the Al layer of FMLs. It should be noted that the empirical crack-opening stress is a function of stress ratio. The stress ratio used to obtain the crack-opening stress is the actual stress ratio in the metal layer of FMLs. In other words, the actual stress ratio in the Al layer is applied to obtain the crack-opening stress in Al alloy.

The crack-opening stress for the Al alloy was plotted as a function of stress ratio and is shown in figure 21 [43]. A plain stress condition (constraint factor c = 1) is considered due to the thin metal layer used in GLARE laminates.

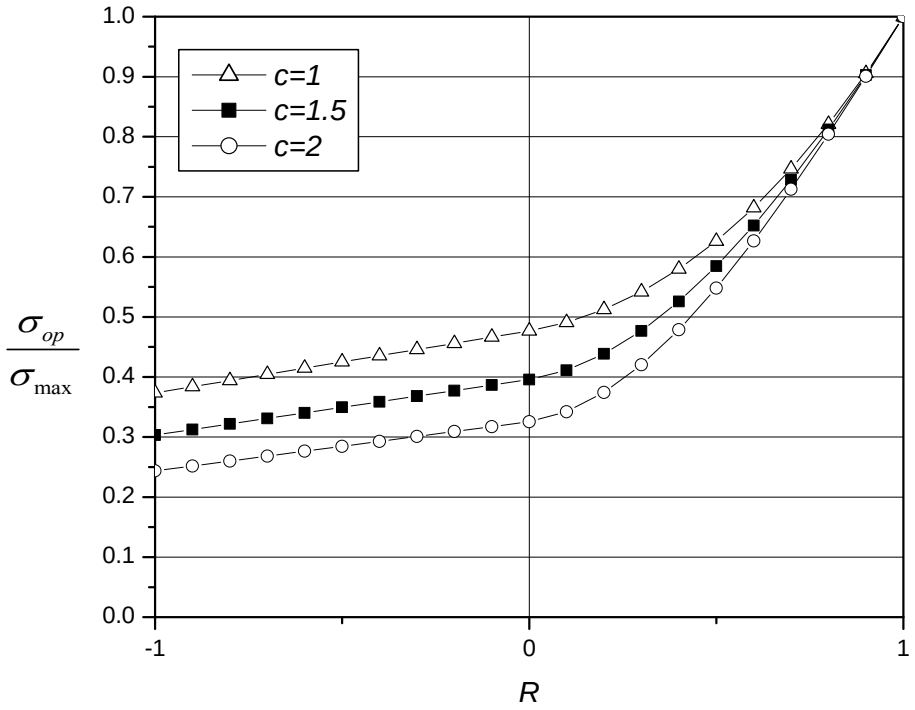

Figure 21. Crack-Opening Stress as a Function of Stress Ratio [43]

4.5.3 Nondimensional SIF.

Analytically, the nondimensional SIFs, f_o, is expressed as [42]

$$f_o = \int_{a_o}^{a} \sigma_o(x) \frac{m_o(a,x)}{\sqrt{\pi a}} dx \tag{55}$$

where $\sigma_n(x)$ is the stress on the crack face induced by the unit applied load and secondary bending, and σ is the scaling factor. The weight function is expressed as

$$m_o(a,x) = 2\sqrt{\frac{a}{\pi(a^2 - x^2)}} \tag{56}$$

and the stress on crack face is expressed as

$$\sigma_o(a,x) = \frac{\sigma_{Al} x}{\sqrt{x^2 - a_o^2}} \tag{57}$$

The nondimensional SIF, f_{br}, is expressed as [42]

$$f_{br} = \int_0^a \sigma_{n,br,Al}(x) \frac{m_{br}(a,x)}{\sqrt{\pi a}} dx \tag{58}$$

where $\sigma_{n,br,Al}(x)$ is the bridging stress on the crack face of the metal layer in FMLs under a unit-applied load. For a periodic array of collinear cracks in a sheet under applied load, the crack-opening displacement leads to the following exact weight function [42]

$$m_{br}(a,x) = \cos(\frac{\pi \bar{x}}{2}) \sqrt{\frac{\frac{2}{\pi \bar{a}} \tan(\frac{\pi \bar{a}}{2})}{\sin^2(\frac{\pi \bar{a}}{2}) - \sin^2(\frac{\pi \bar{x}}{2})}} \tag{59}$$

The dimensionless bridging SIF was plotted as a function of crack length and is shown in figure 22. Clearly, there is a transition in the dimensionless bridging factor. Physically, it indicates that the influence of the fiber-bridging effect would lower the SIF, leading to an approximately steady-state crack growth after a certain number of cycles. Compared to the far-field and bridging SIFs, the effective SIF was plotted as a function of crack length and is shown in figure 23.

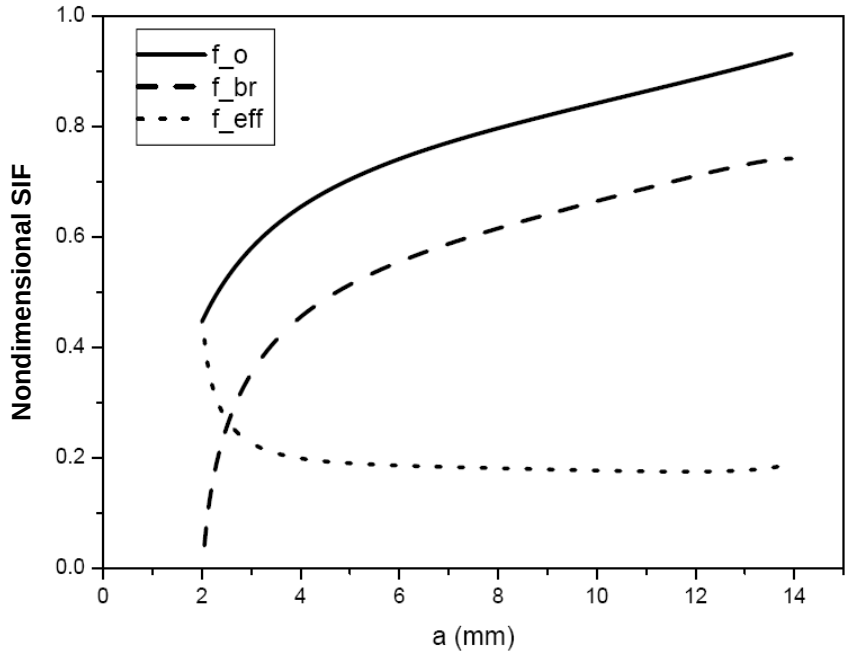

(a)

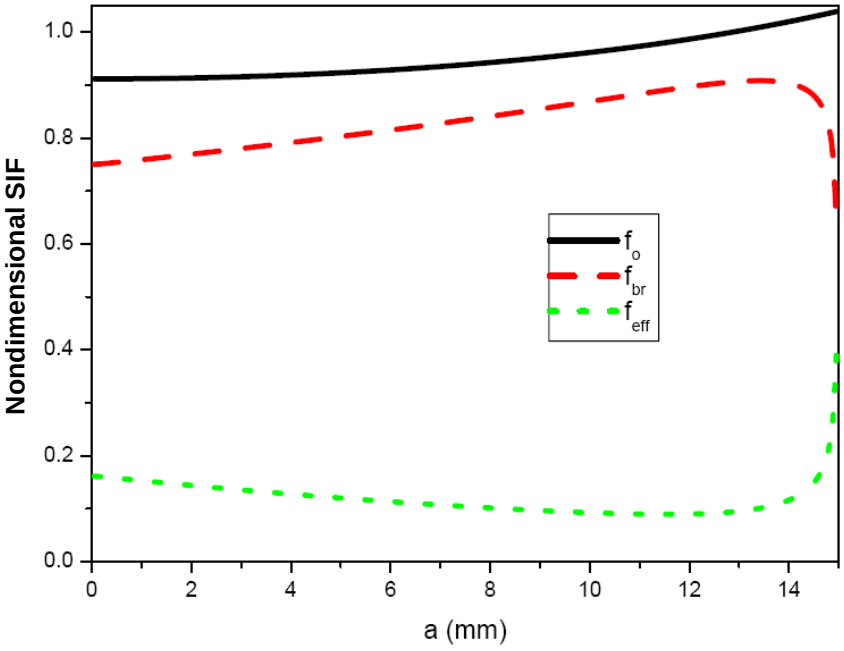

(b)

Figure 22. Effective Nondimensional SIF ($f_{\text{eff}} = f_o - f_{br}$) as a Function of Crack Length (a) Through-Thickness and (b) Partial-Thickness

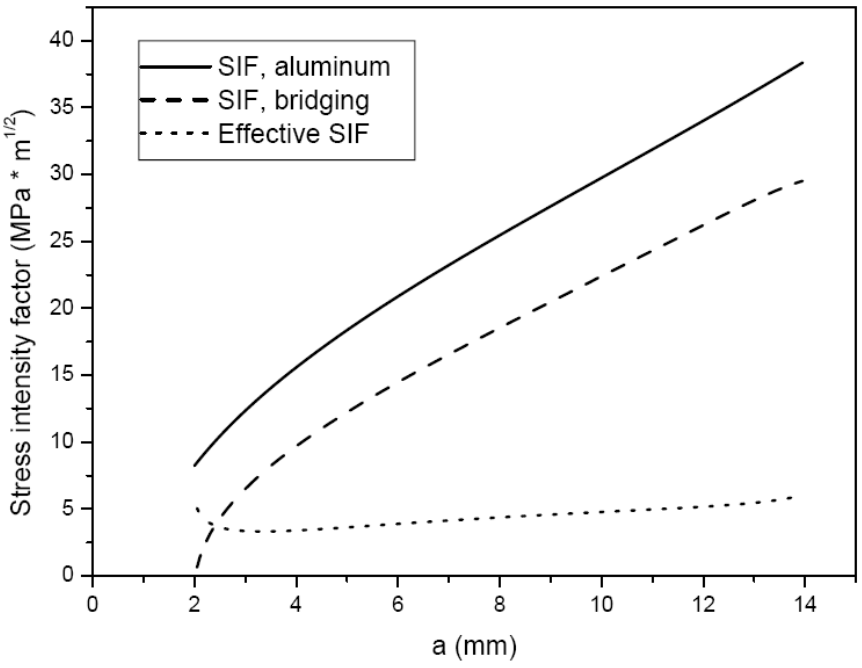

(a)

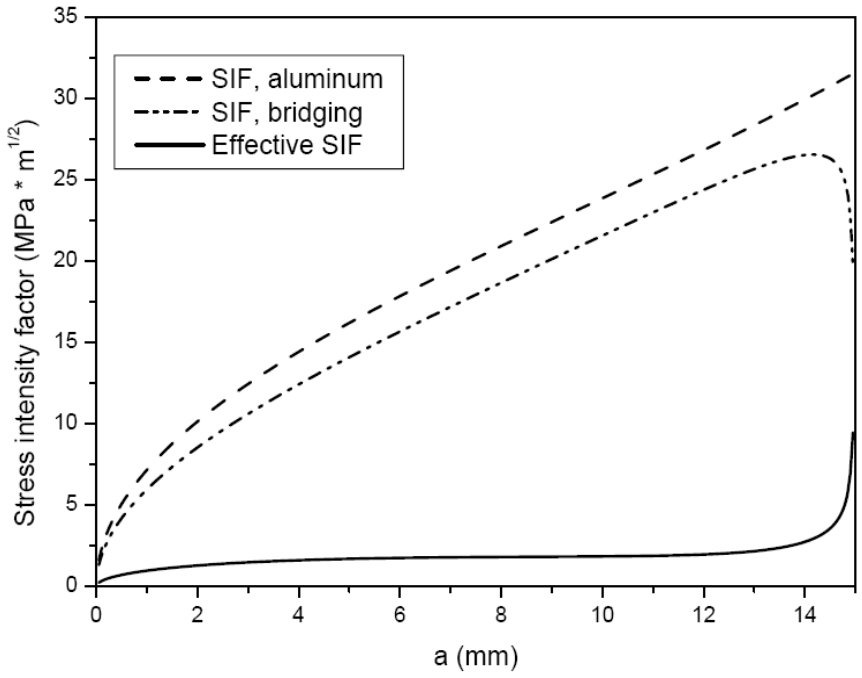

(b)

Figure 23. Effective SIF for GLARE 3-3/2 Specimens With Multiple Surface Cracks Under the Applied Stresses of 120 MPa With an Applied Stress of 0.05 (a) Through-Thickness and (b) Partial-Thickness

4.6 FATIGUE CRACK GROWTH PREDICTION.

In GLARE laminates, the constituent metal layer is Al 2024-T3, and it is assumed that the fatigue law can be used for predicting crack growth rate (*da*). The empirical Paris-Walker fatigue equation (mm/cycle) is expressed as [36]

$$\frac{da}{dN} = C_{g1}\left[\Delta K_{tip}\right]^{n_{g1}} \tag{60}$$

The constituent metal of hybrid FMLs is Al 2024-T3, which corresponds to $C_g = 1.27\times10^{-11}$ and $n_g = 2.94$. The effective SIF is in the unit of $MPa\sqrt{mm}$.

4.7 FATIGUE DELAMINATION GROWTH PREDICTION.

For FMLs, the delamination growth (mm/cycle) (*db*) can be expressed as a function of the strain energy release rate [44]. That is

$$\frac{db}{dN} - C_b(\Delta\sqrt{g})^{nb} = C_b(\sqrt{g_{\max} - \sqrt{g_{\min}})^{nb}} \tag{61}$$

The GLARE empirical coefficients C_b and n_b are 0.05 and 7.5, respectively [44], and the strain energy release rate is expressed as [44 and 45]

$$g = \frac{\sigma_{fml}^2}{2n_iE_{Al}}[\gamma^2(n_{Al}-1) - \lambda^2 n_{Al}t_{Al} + \frac{E_{f,0}}{E_{Al}}n_{f,0}t_{f,0}(\gamma^2-\lambda^2) + \frac{E_{f,90}}{E_{Al}}n_{f,90}t_{f,90}(\gamma^2-\lambda^2)] \tag{62}$$

where n_i is the number of interfaces, and

$$\gamma = \frac{t_{fml}}{(n_i-1)t_{Al} + \frac{E_{f,0}}{E_{Al}}n_{f,0}t_{f,0} + \frac{E_{f,90}}{E_{Al}}n_{f,90}t_{f,90}} \tag{63}$$

$$\lambda = \frac{t_{fml}}{n_{Al}t_{Al} + \frac{E_{f,0}}{E_{Al}}n_{f,0}t_{f,0} + \frac{E_{f,90}}{E_{Al}}n_{f,90}t_{f,90}} \tag{64}$$

As observed in this study, there is a mixed-mode involvement of delamination growth near the stage of delamination linkup. In this study, only mode II delamination growth was considered. Also, it should be noted that the secondary bending is not considered in delamination growth.

5. TEST RESULTS.

5.1 MULTIPLE-IMPACT BEHAVIOR OF GLARE 5-2/1 LAMINATES.

The multiple-impact loads were applied to GLARE 5-2/1 by the weight drop. The impact loads were repeated twice to observe the accumulated damage in GLARE 5-2/1 laminates. Three levels of impact energy were set in the experiment: 8 J, 16 J, and 26 J, respectively. If there was immediate metal cracking after weight drop, the impact energy would not increase. The maximum impact energy applied was 26 J, which would cause a permanent metal opening in the GLARE 5-2/1 laminates.

Figure 24(a) and (b) show multiple-impact dent damage (which is BVID) in Al 2024-T3 and GLARE 5-2/1 in the top and bottom figures, respectively. The crack multiple-impact damage (which is CVID) in Al 2024-T3 and GLARE 5-2/1 is shown in figure 24(c). The CVID in GLARE 5-2/1 occurred in the outer Al layer on the nonimpacted side along the 0° and 90° fiber direction.

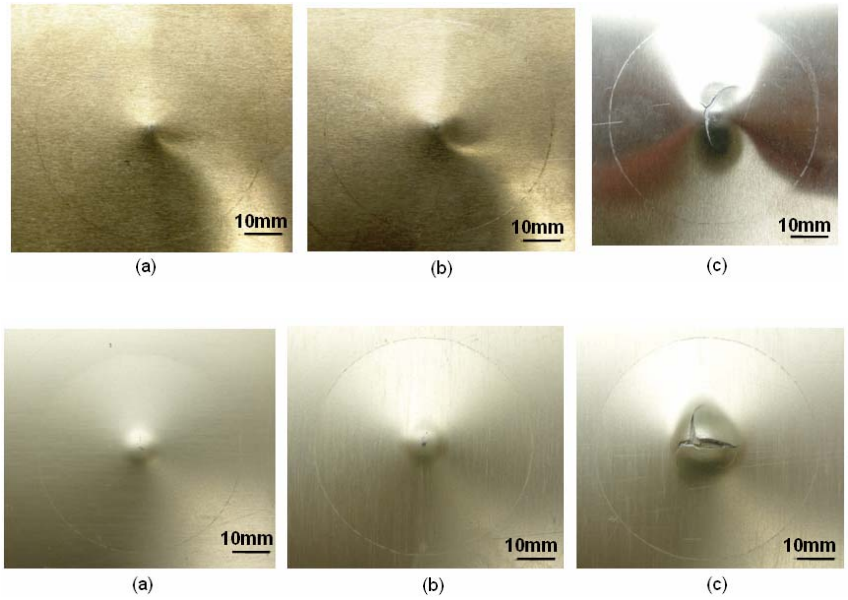

Figure 24. Multiple-Impact Damage of Al 2024-T3 (Top) and GLARE 5-2/1 (Bottom) at (a) BVID (8 J (2x4 J)), (b) BVID (16 J (2x8 J)), and (c) CVID (26 J (2x13 J))

Figure 25 shows experimental results for the load-time history of Al 2024-T3 and GLARE 5-2/1. After the first impact of 8 J and 16 J, Al 2024-T3 and GLARE 5-2/1 experience the plastic deformation. After the second impact for Al 2024-T3 and GLARE 5-2/1, 8 J shows the same trend as the first impact. However, the 16-J GLARE 5-2/1 shows a small, sharp load drop. This discrete load drop is believed to indicate the delamination and failure of the composite layer [4]. At a multiple-impact energy of 26 J, after the second impact in Al 2024-T3 and GLARE 5-2/1, the load was dramatically reduced, indicating the occurrence of CVID. The specific energy to create a dent and crack damage in the outer Al layer for Al 2024-T3 is somewhat higher than GLARE 5-2/1. It comes from the effects of thickness and minimum cracking energy. As shown

in reference 4, the minimum cracking energy of Al 2024-T3 is somewhat higher than GLARE 5-2/1. As the relationship of the area density and impact energy is considered, GLARE 5-2/1 shows a better impact performance than Al 2024-T3.

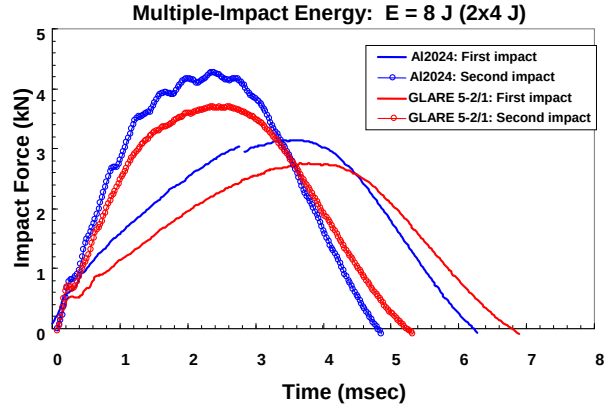

(a)

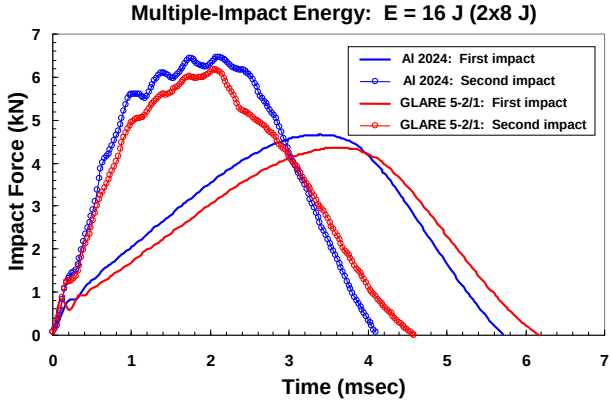

(b)

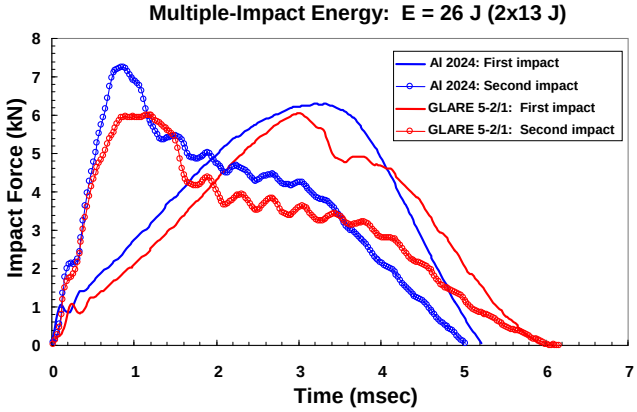

(c)

Figure 25. Load-Time Histories of Al 2024-T3 and GLARE 5-2/1 Under Multiple Impact With (a) Impact Energy = 8 J, (b) Impact Energy = 16 J, and (c) Impact Energy = 26 J

Figure 26 shows the permanent central displacement of Al 2024-T3 and GLARE 5-2/1 as a function of impact energy after low-velocity impact. After the first impact, GLARE 5-2/1 has almost the same dent depth as Al 2024-T3. However, after the second impact, GLARE 5-2/1 shows a larger dent depth than Al 2024-T3. The total dent depth may be affected by the dent depth after the second impact. Finally, the difference of total dent depth between GLARE 5-2/1 and Al 2024-T3 is 10%.

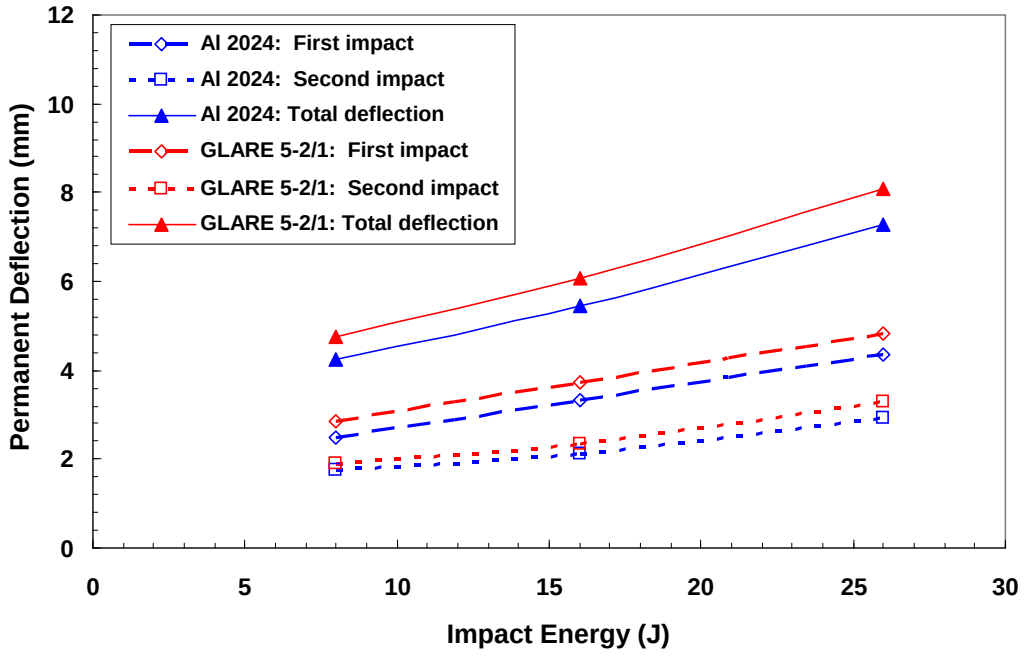

Figure 26. The Permanent Central Deflection as a Function of Impact Energy

Figure 27 shows the multiple-site impact damage fatigue crack growth on a variety of GLARE 5-2/1 specimens at different fatigue cycles. Cracks may initiate from the edge or from the damage area and travel along the crack path. Crack lengths were carefully measured at specific fatigue cycles.

Figures 28-31 show the crack length as a function of cycles under different applied stresses. The applied stresses corresponded to the postimpact tensile strength. In this experiment, the site location is indicated by the number. The letters "R" and "L" indicates whether the fatigue crack is on the right or left of the impact site. The letters "d" and "e" represent the damage area and edge crack initiation sites, respectively. For example, "1Le" represents the fatigue crack that is located on the left-hand side of impact 1, and this crack initiates from the edge of the sample. Table 7 is a summary of the crack growth data.

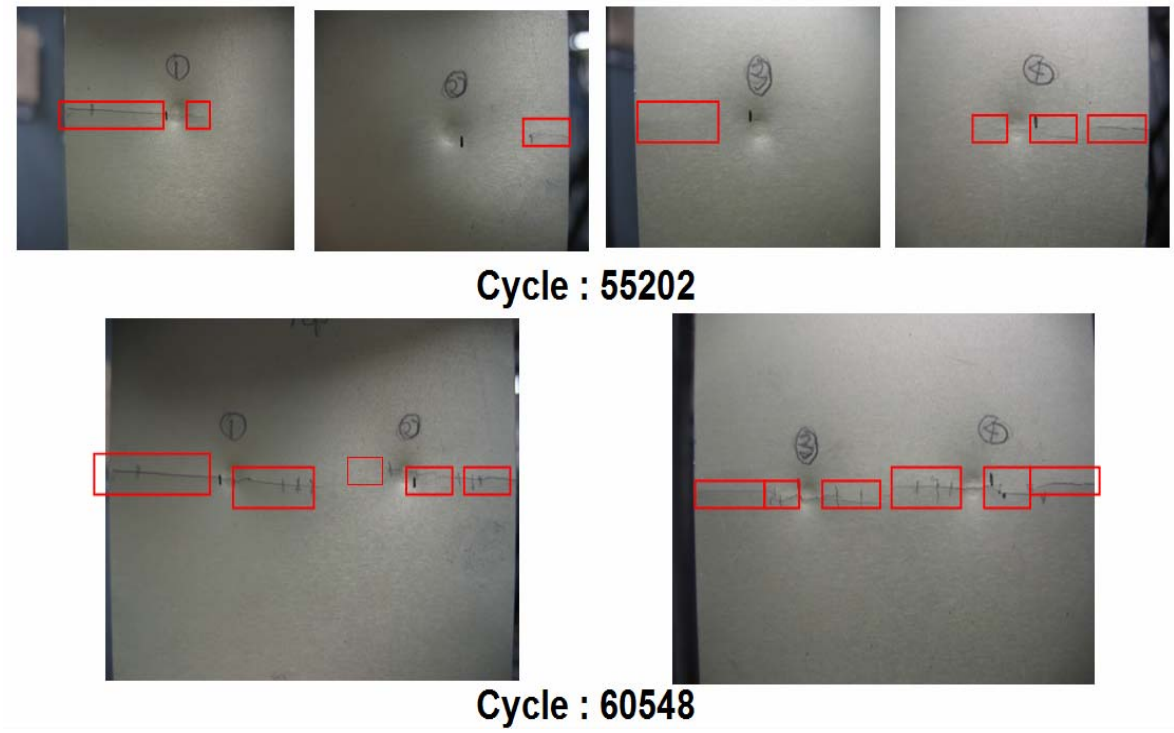

Figure 27. Multiple-Site Impact Damage Fatigue Crack Propagation

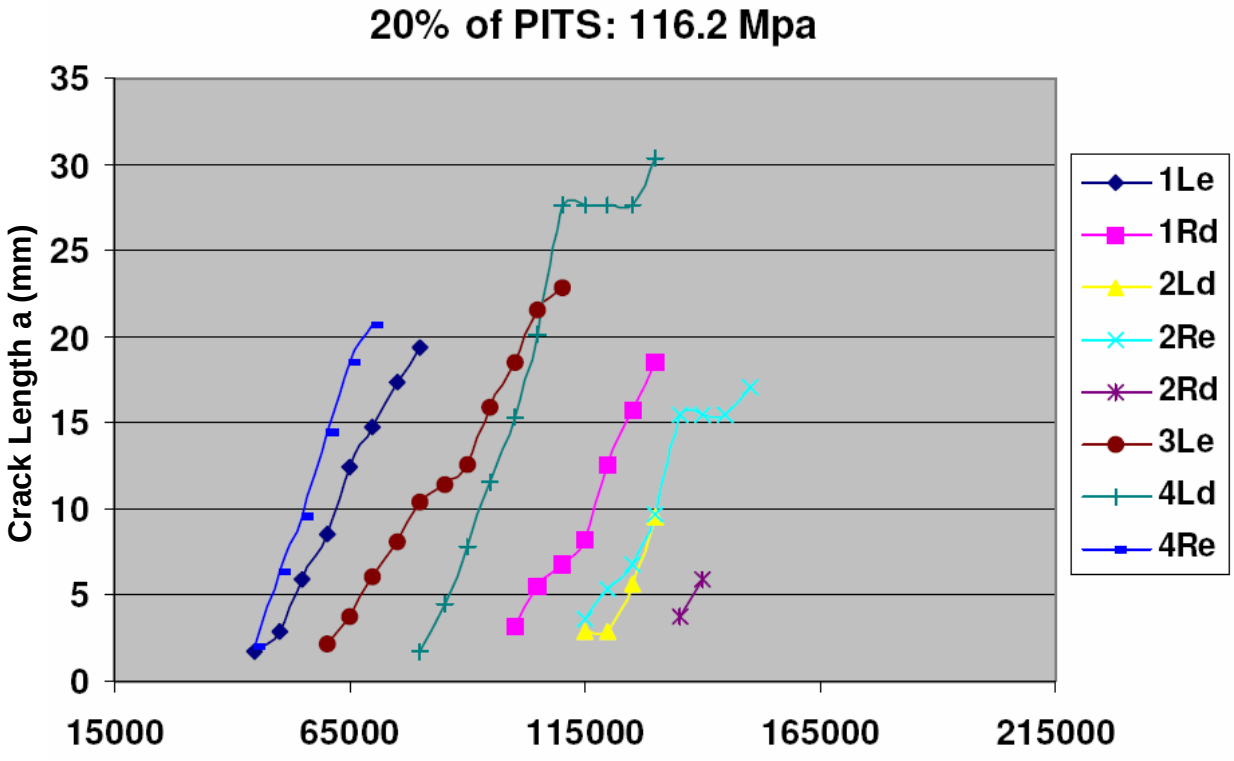

Figure 28. Multiple-Site Impact Damage Fatigue Crack Growth (116.2 MPa)

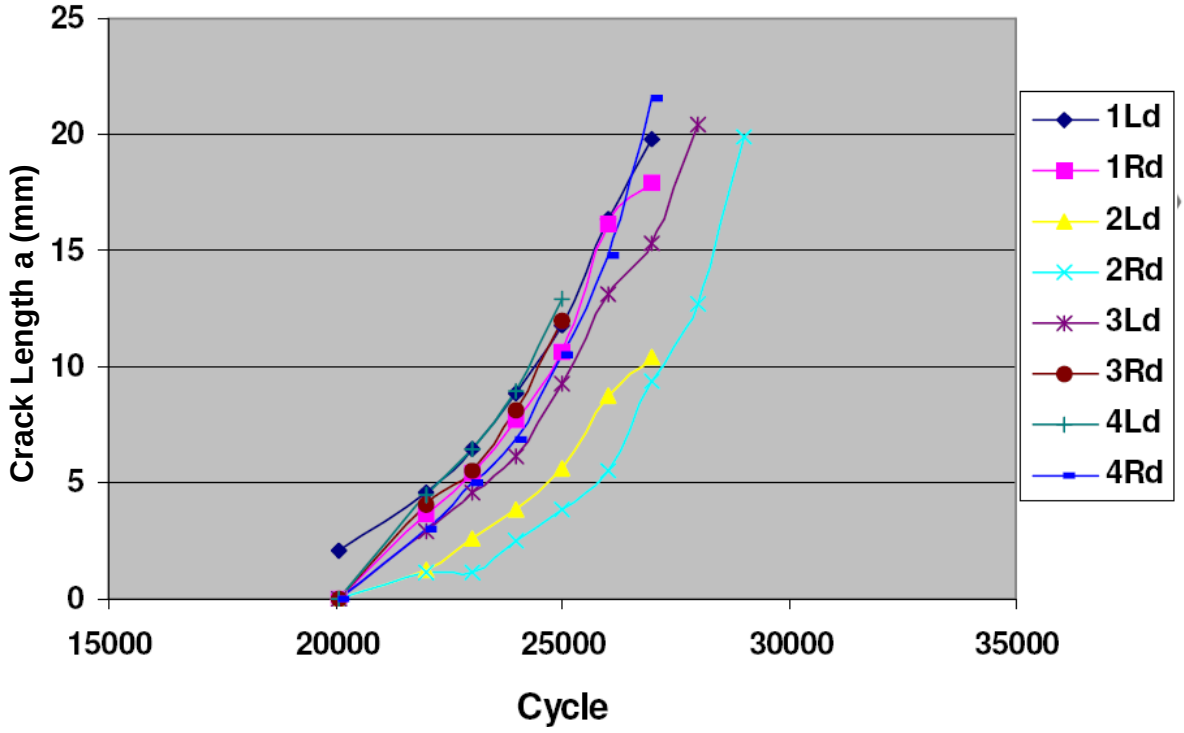

Figure 29. Multiple-Site Impact Damage Fatigue Crack Growth

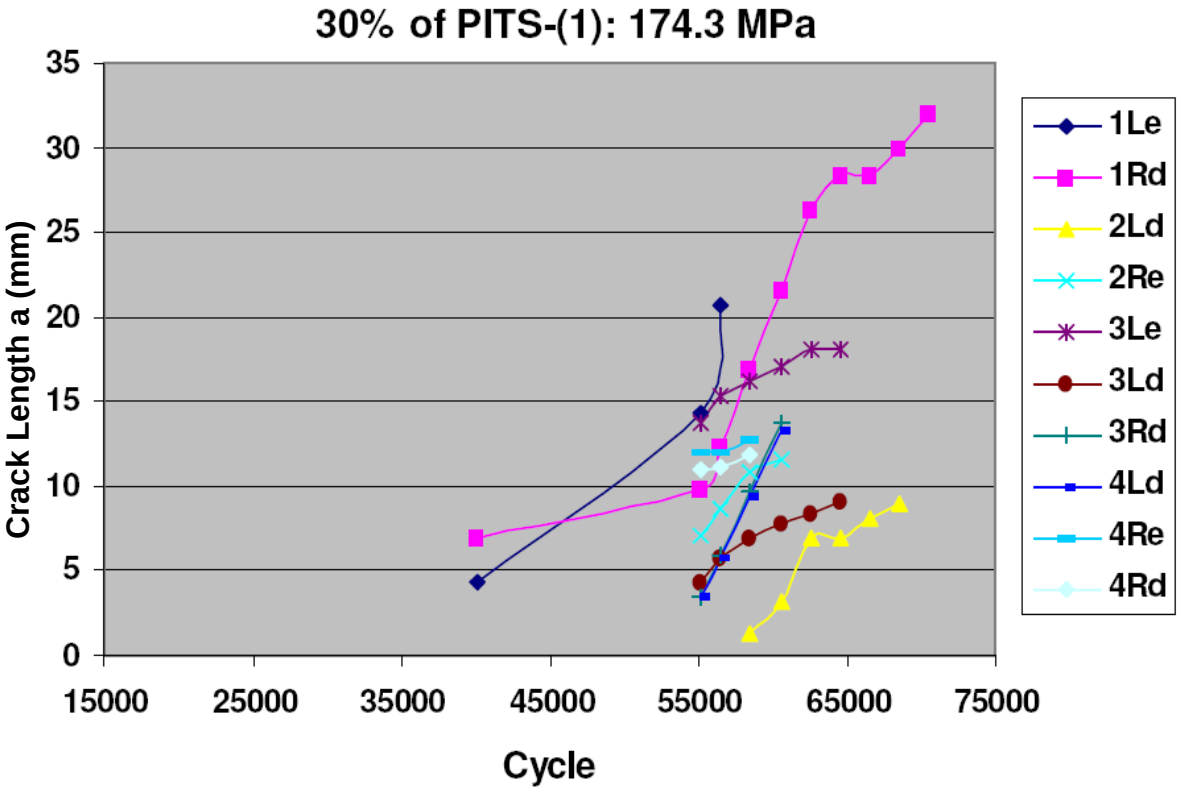

Figure 30. Multiple-Site Impact Damage Fatigue Crack Growth (174.3 MPa)

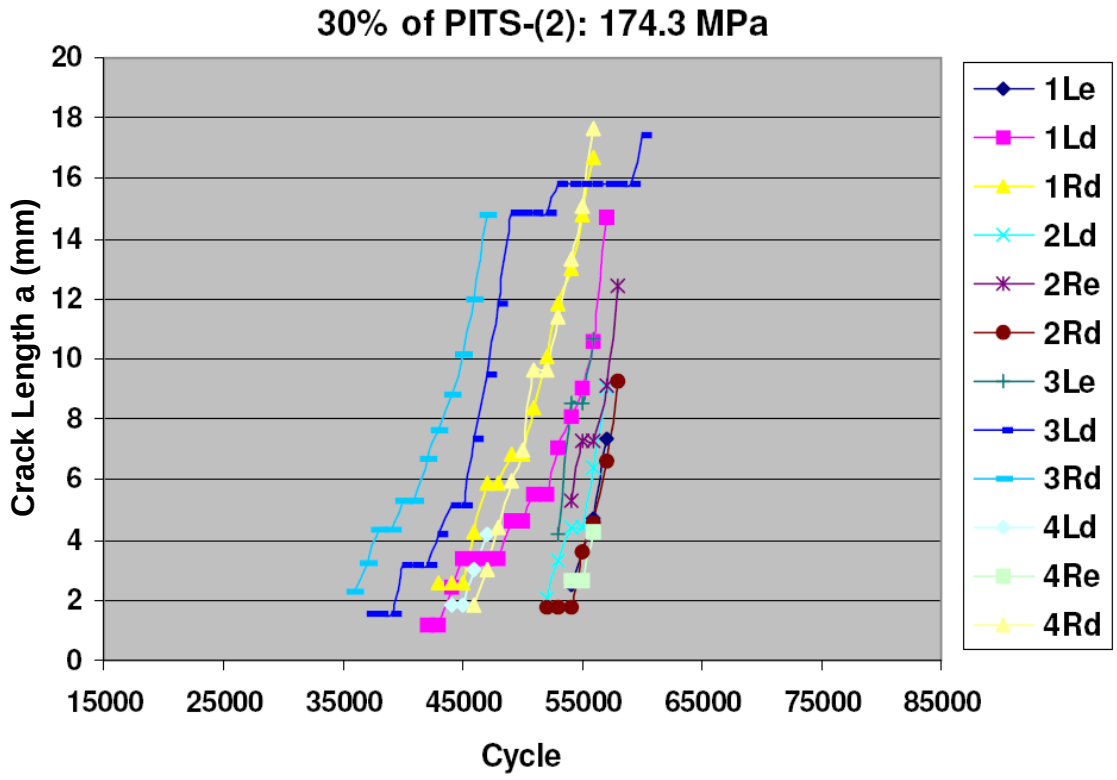

Figure 31. Multiple-Site Impact Damage Fatigue Crack Growth (174.3 MPa)

Table 7. Multiple-Site Impact Damage Fatigue Crack Growth Data

No./Cycle	1E	1L	1R	2L	2R	2E	3E	3L	3R	4L	4R	4E
55202	14.34	0	6.93	0	0	7.09	13.67	4.27	3.49	3.49	11.04	12.02
60548	20.72	0	16.93	5.11	0.75	11.64	17.03	7.79	13.68	13.27	11.88	12.72

Unit of measurement: mm

5.2 MULTIPLE-SITE DAMAGE FATIGUE BEHAVIOR OF GLARE 3-3/2 LAMINATES.

To study MSD fatigue crack growth behavior, two scenarios were considered in GLARE 3-3/2 laminates. (1) Through-thickness crack growth, which means that all cracks will initiate and propagate in all the metal layers of FMLs. (2) The partial-thickness crack growth, which means that cracks only initiate and propagate in the surface metal layer. For surface crack growth in FMLs, due to the unsymmetry of crack growth, the secondary bending effect needs to be addressed properly. All specimens were tested under tension-tension, constant-amplitude fatigue loading.

5.2.1 Through-Thickness Crack Growth.

In the presence of a through-thickness starter notch, the cracks initiated from the notch tip in the direction perpendicular to the applied load in all cases, as shown in figure 32. Cracks initially grew away in the stable growth phase from the open hole/start notch at zero angles and then continued to grow without any change in crack trajectories, i.e., a mode I SIF-dominant crack growth in the metal layer. As two cracks propagated toward each other and reached the region of linkup, they bypassed each other, leading to a formation of an eye-shaped region, instead of having a direct crack linkup (figure 32). At this juncture, the crack growth was unstable, and the crack path angle changed toward the opposite crack trajectory. The crack path deviated and did not remain 0°. This phenomenon is explained as two propagating cracks in the vicinity of a crack linkup mutually influencing each other, and the crack trajectory is determined by a function of mode I and mode II SIF.

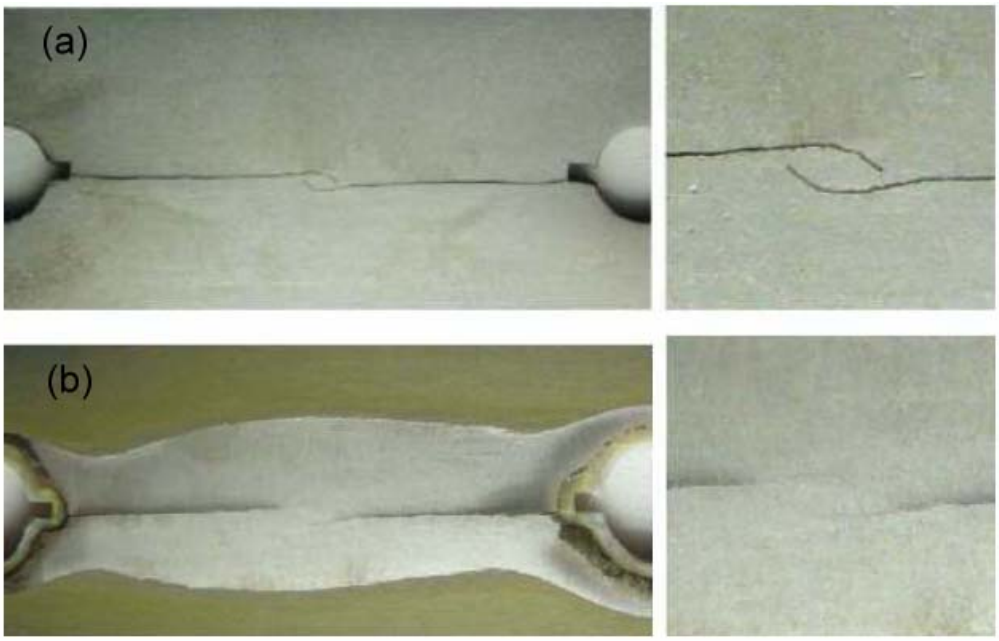

Figure 32. On-Going MSD Fatigue Cracks in GLARE 3-3/2 (a) Crack Growth in the Surface Metal Layer and (b) Crack Growth in the Inner Metal Layer (A close-up of the crack bypass is shown on the right.)

Furthermore, it was observed that the crack length in the inner metal layer was almost identical to the crack length in the outer metal layer, as shown in figure 32(b), after removing the surface metal layers. Similarly, an eye-shaped region was observed in the inner Al layer of GLARE 3-3/2 laminates. Compared to specimens with a single through-thickness notch, this observation was different since the direction of the crack path remained the same as the cracks propagated through the metal layers of the laminate.

Meanwhile, the delamination zones in the fiber/adhesive layer appeared to avoid linkup as they grew toward each other, as shown in figure 33. The stable delamination growth is a

mode II-dominant fracture behavior; however, it became a mixed mode (mode I and mode II) delamination behavior as two delaminations approached the region of linkup and deviated from the original center line. In other words, the shear stress induced by cyclic fatigue loading did not affect the direction of the mode II-dominant delamination growth until it fell into the eye-shaped crack formation region. Ultimately, the two propagating delaminations emerged to be approximately a rectangular shape. A brief summary of the experimental results are listed in table 8.

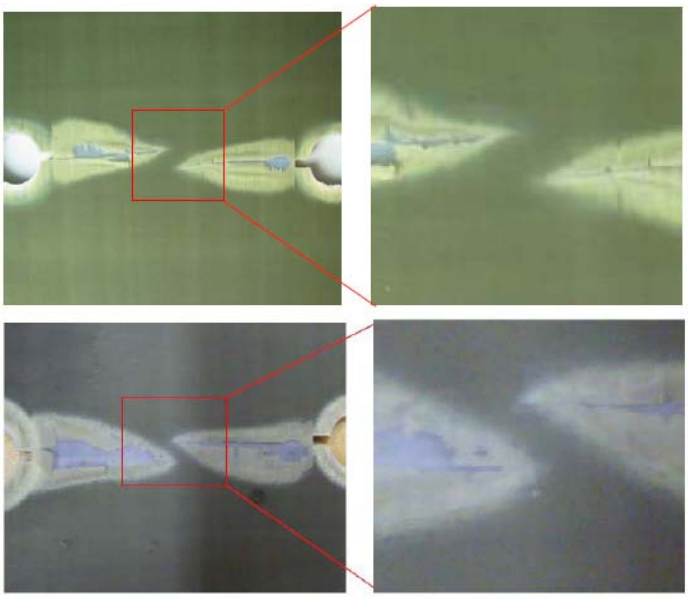

Figure 33. The MSD Fatigue Delamination Pattern in the Fiber/Adhesive Layer at Cracks 1B and 2B for GLARE 3-3/2

The crack lengths as a function of fatigue cycles for GLARE 3-3/2 specimens under maximum applied stresses of 120 and 100 MPa were recorded through continuous monitoring during the fatigue tests. For the ease of investigation in MSD crack growth, all the cracks in the upper and bottom rows in table 8 were categorized as lead cracks and nonlead cracks, and the total average crack length was used as a base line.

The multiple-site crack propagations as a function of fatigue cycles under different applied stresses are shown in figures 34 and 35, respectively. The lead and nonlead cracks do not have the same crack length, which indicates that the cracks interacted with one another. The crack growth rates as a function of crack length were plotted and are shown in figures 36 and 37 for the applied stresses of 120 and 100 MPa, respectively. The initial fast crack growth phase was one in which insufficient fiber bridging occurred to transfer enough load from the Al sheet to reduce the effective SIF at the crack tip. Initially, the crack growth rate decreased, and then grew progressively. Unlike a single-notched specimen, the crack growth rate was approximately a constant due to the absence of crack interaction. This correspondence to the fiber-bridging mechanism is dependent on the delamination profiles proposed by Guo and Wu [34 and 35] and the damage-tolerant characteristics of fiber-metal laminates. As the bridging SIF becomes predominant, the crack growth reaches a steady state.

Table 8. Summary of Experimental Results for Through-Thickness GLARE 3-3/2 Laminates

Applied Stress Level = 120 MPa, Applied Stress Ratio = 0.05					
Panel ID	Starter Notch (mm)	Total Crack Length (mm)	Final Cycles (N)	Averaged Crack Growth Rates (mm/cycle)	Lead Crack (linkup)/ Nonlead Crack
T1	1	11.43	70,000	1.63E-04	Lead
T2	1	11.43	70,000	1.63E-04	Lead
T3	1	11.43	70,000	1.63E-04	Lead
T4	1	11.43	70,000	1.63E-04	Lead
B1	1	9.144	70,000	1.31E-04	Nonlead
B2	1	9.144	70,000	1.31E-04	Nonlead
B3	1	9.144	70,000	1.31E-04	Nonlead
B4	1	9.144	70,000	1.31E-04	Nonlead
Applied Stress Level = 100 MPa, Applied Stress Ratio = 0.05					
T1	1	7.62	145,984	5.21975E-05	Nonlead
T2	1	7.62	145,984	5.21975E-05	Nonlead
T3	1	11.43	145,984	7.82963E-05	Lead
T4	1	11.43	145,984	7.82963E-05	Lead
B1	1	11.43	145,984	7.82963E-05	Lead
B2	1	11.43	145,984	7.82963E-05	Lead
B3	1	8.89	145,984	6.08971E-05	Nonlead
B4	1	8.89	145,984	6.08971E-05	Nonlead

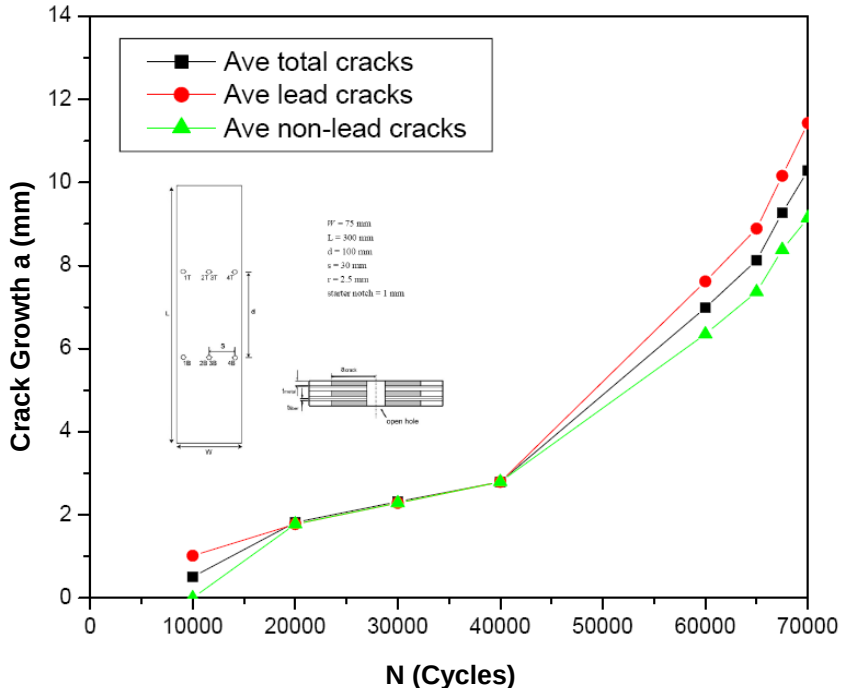

Figure 34. Average Crack Length as a Function of Cycles for GLARE 3-3/2 Laminates at the Applied Stress Level of 120 MPa

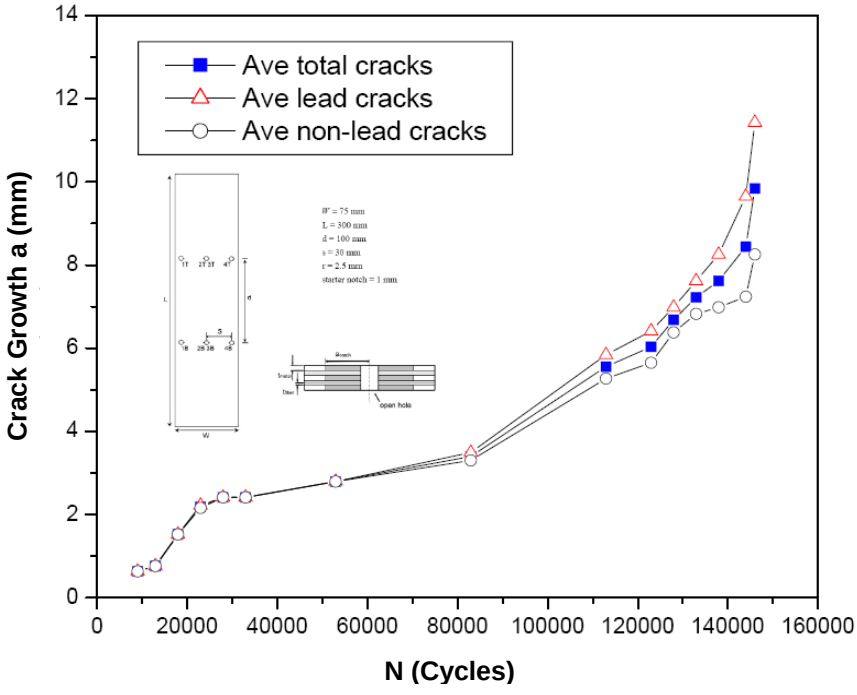

Figure 35. Average Crack Length as a Function of Cycles for GLARE 3-3/2 Laminates at the Applied Stress Level of 100 MPa

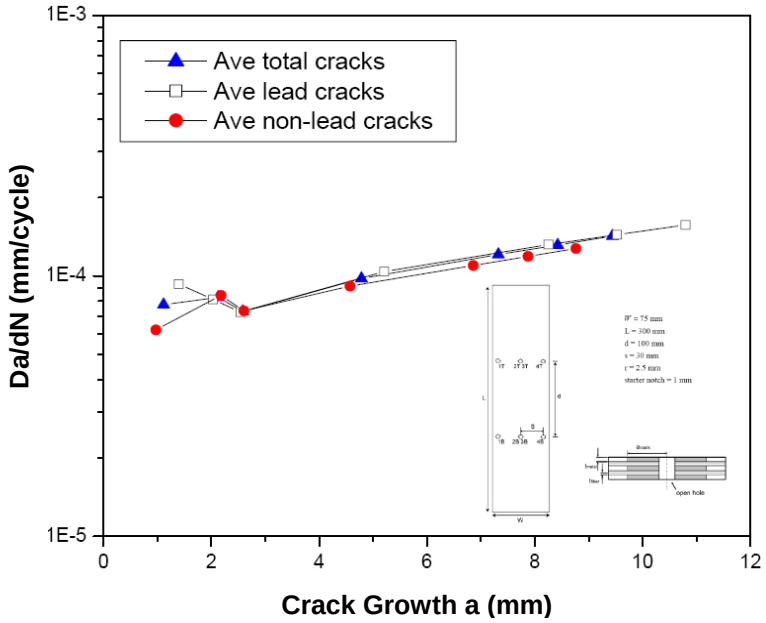

Figure 36. Average Crack Growth Rate as a Function of Crack Length for GLARE 3-3/2 Laminates at the Applied Stress Level of 120 MPa

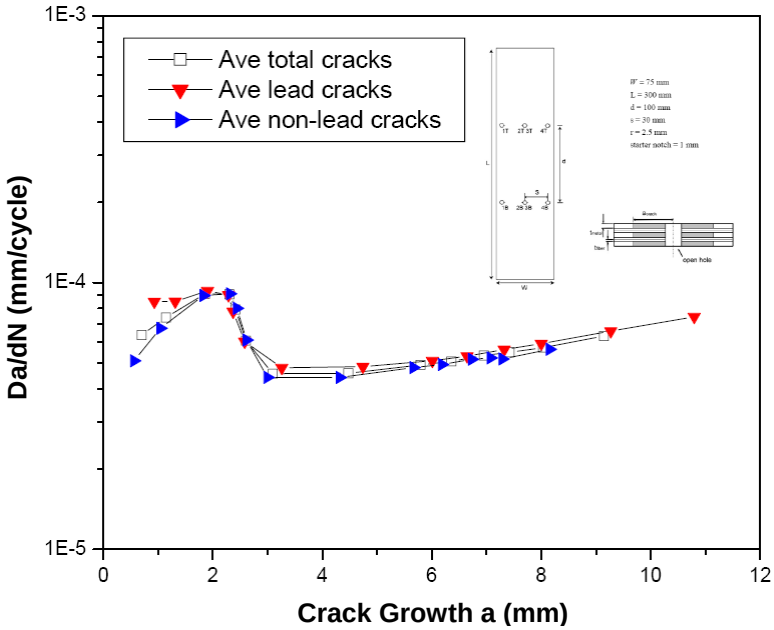

Figure 37. Average Crack Growth Rate as a Function of Crack Length for GLARE 3-3/2 Laminates at the Applied Stress Level of 100 MPa

The presence of multiple-site fatigue cracks would accelerate the crack growth rates, as shown in figures 36 and 37. Therefore, as two propagating cracks approached each other, the crack growth rates increased gradually due to the effect of crack interaction. Ultimately, the crack growth rates reached peak values when the cracks linked up near the eye-shaped region.

In MSD crack growth, since the Al sheet had a higher modulus, it picked up more load than the S2-glass/prepreg; this higher percentage of overall load translated to higher stress in the metal layers to drive the cracks. Cracks began to propagate and then reached approximately constant. Some cracks grew faster and some were relatively slower. Ultimately, the final leading crack lengths were significantly greater than the average crack lengths.

5.2.2 Partial-Thickness Crack Growth.

To evaluate the fatigue behavior of multiple surface cracks, all cracks were divided into two categories, leading cracks (lead crack) and nonleading (nonlead) cracks. Experimentally, it was observed that with the presence of multiple surface slits under fatigue loading, cracks in all cases initiated at locations on the edge of the surface slits and propagated approximately perpendicular to the direction of the applied load. The cracks continued to grow away perpendicularly to the loading direction. These cracks did not initiate at the same time nor did they propagate with the same growth rates. Figure 38 shows the nonlead and lead cracks. As the propagating cracks were approaching each other at the vicinity of the crack fronts, they had a direct crack linkup, leading to a straight line formation instead of bypassing each other at the applied stress level of 120 MPa, as shown at the bottom of figure 38. In other words, mode I fracture behavior dominates in surface crack growth as cracks linkup. Figure 39 shows the corresponding nonlead delamination and lead delamination. Similarly, lead delaminations formed a direct linkup at the vicinity of the crack tips at the applied stress of 120 MPa.

The surface crack lengths were measured during the fatigue loading. For the ease of comparing the deviation of crack growth rates, the averaged lead crack and averaged nonlead crack growth rates were used with the averaged total crack growth rate as a base line. A brief summary of the experimental results are listed in table 9.

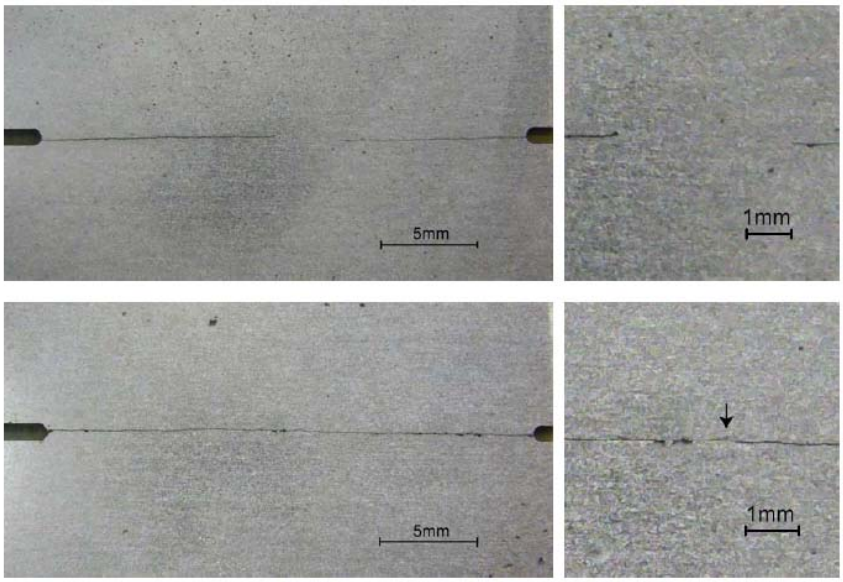

Figure 38. Crack Propagation in Surface-Cracked GLARE 3-3/2 at the Applied Stress Level of 120 MPa (Top: nonlead cracks and Bottom: lead cracks and crack linkups)

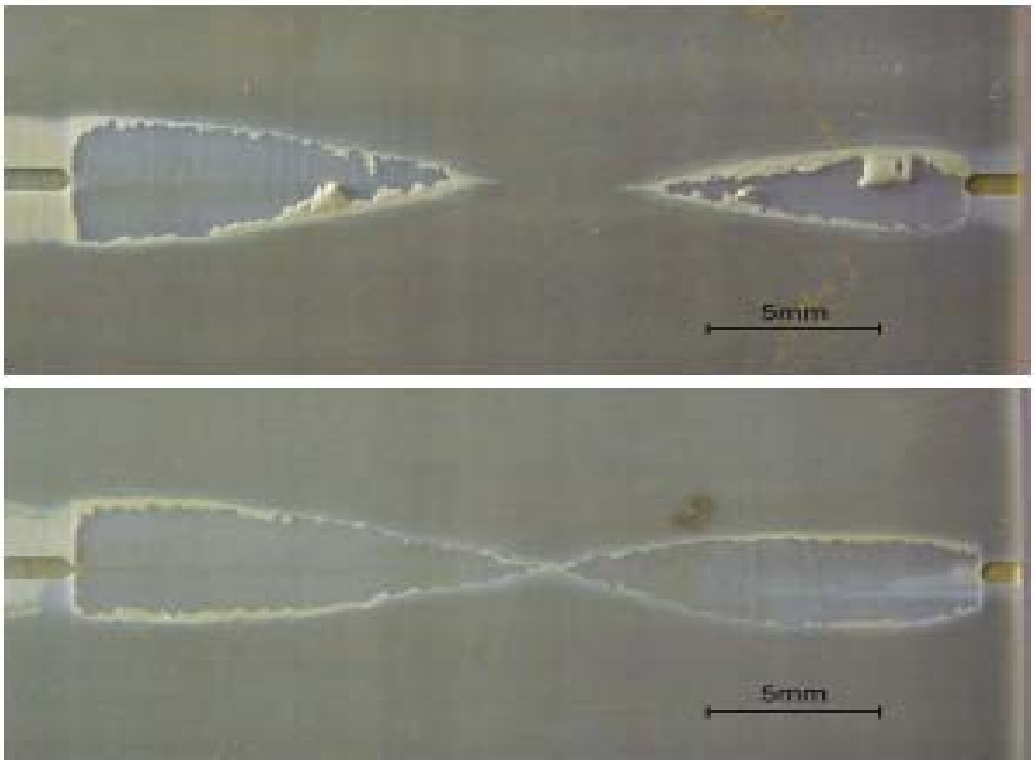

Figure 39. Delamination Growth in Surface-Cracked GLARE 3-3/2 Specimens, Nonlead Delamination (top) and Leading Delamination and Linkup (bottom)

Table 9. Summary of Experimental Results for GLARE 3-3/2 Surface (Partial-Thickness) Crack Growth

Applied Stress Level = 120 MPa, Applied Stress Ratio = 0.05					
Panel ID	Half Slit (mm)	Total Crack Length (mm)	Final Cycles (N)	Averaged Crack Growth Rates (mm/cycle)	Lead Crack (linkup)/Nonlead Crack
T1	2	13.335	570,000	2.33947E-05	Lead
T2	2	12.828	570,000	2.25053E-05	Lead
T3	2	11.303	570,000	1.98298E-05	Nonlead
T4	2	10.922	570,000	1.91614E-05	Nonlead
B1	2	12.7	570,000	2.22807E-05	Nonlead
B2	2	10.922	570,000	1.91614E-05	Nonlead
B3	2	10.795	570,000	1.89386E-05	Nonlead
B4	2	9.652	570,000	1.69333E-05	Nonlead

Table 9. Summary of Experimental Results for GLARE 3-3/2 Surface (Partial-Thickness) Crack Growth (Continued)

Applied Stress Level = 120 MPa, Applied Stress Ratio = 0.05					
Panel ID	Half Slit (mm)	Total Crack Length (mm)	Final Cycles (N)	Averaged Crack Growth Rates (mm/cycle)	Lead Crack (linkup)/Nonlead Crack
Applied Stress Level = 100 MPa, Applied Stress Ratio = 0.05					
T1	2	5.08	750,000	6.77333E-06	Nonlead
T2	2	3.556	750,000	4.74133E-06	Nonlead
T3	2	5.08	750,000	6.77333E-06	Nonlead
T4	2	3.302	750,000	4.40267E-06	Nonlead
B1	2	6.6096	750,000	8.8128E-06	Lead
B2	2	5.08	750,000	6.77333E-06	Nonlead
B3	2	2.794	750,000	3.72533E-06	Nonlead
B4	2	2.794	750,000	3.72533E-06	Nonlead

The averaged crack lengths as a function of fatigue cycles under the maximum applied stress of 120 and 100 MPa were plotted and are shown in figures 40 and 41, respectively. Under the same fatigue cycles, the lead and nonlead cracks did not reach the same length, and crack growth deviation existed. Especially for cracks propagated at the applied stress of 100 MPa, the crack length deviation was obvious. The averaged crack growth rates as a function of crack length are shown in figures 42 and 43 for the corresponding applied stress levels. The crack growth deviation between the lead and nonlead cracks is small at the applied stress of 120 MPa, and the crack growth deviation is obvious at the applied stress of 100 MPa.

In FMLs, crack growth rate decelerated once the crack reached a certain length. When the cracked metal layer becomes more compliant, it will carry less load locally, which is the source of fatigue crack growth retardation. That is, there is load transfer to the fiber layers through the crack flanks and at the crack tips. Since the aluminum sheet has a higher modulus, it picks up more load than the S2-glass/prepreg. This higher percentage of overall load translates to higher stress in the metal layers to drive the cracks. On the experimental observation, surface crack growth was much slower compared to through-thickness crack growth. The further reduced crack growth rates in the surface-cracked GLARE laminates were attributed to the extent of greater bridging traction, provided by the intact laminates, and to the extent of higher residual strength. These surface-cracked specimens are more damage-tolerant than through-thickness GLARE laminates.

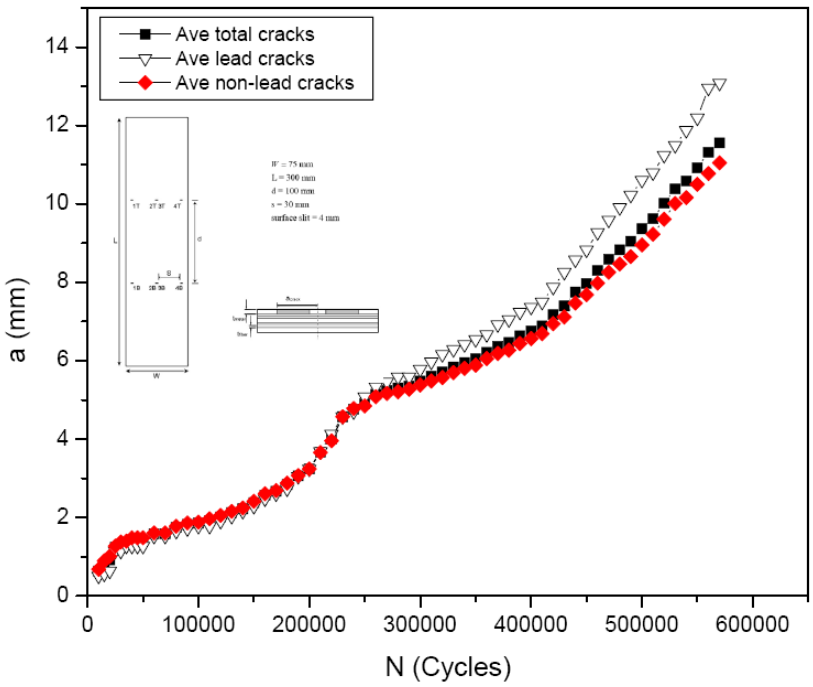

Figure 40. The MSD Crack Length as a Function of Cycles for Surface-Cracked GLARE 3-3/2 at the Applied Stress of 120 MPa

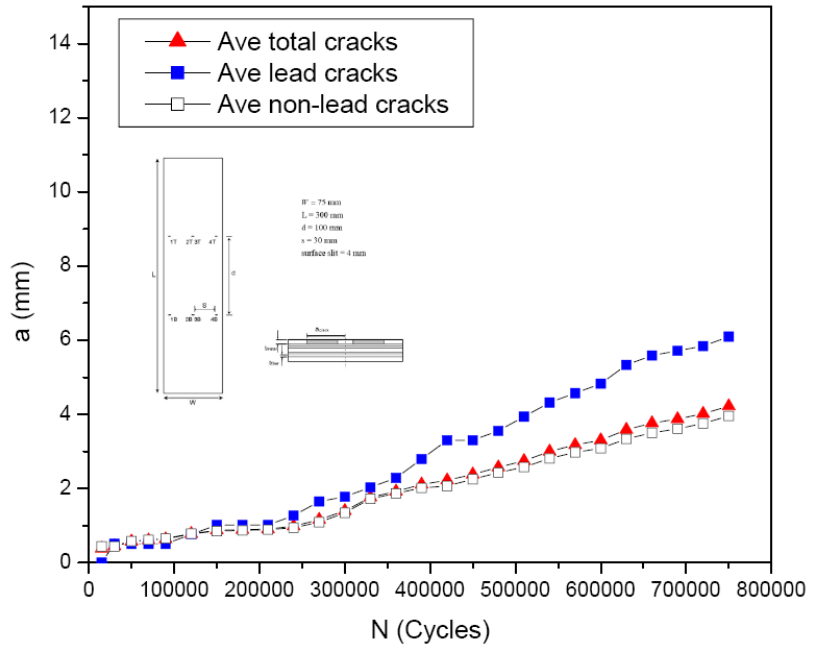

Figure 41. The MSD Crack Length as a Function of Cycles for Surface-Cracked GLARE 3-3/2 at the Applied Stress of 100 MPa

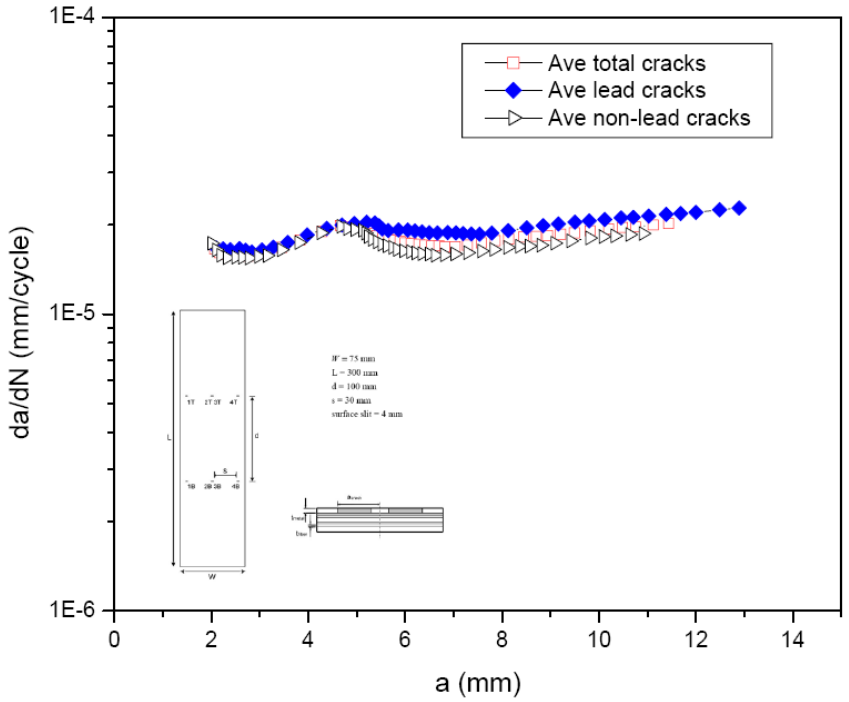

Figure 42. The MSD Crack Growth Rate as a Function of Crack Length at the Applied Stress of 120 MPa for Surface-Cracked GLARE Specimen

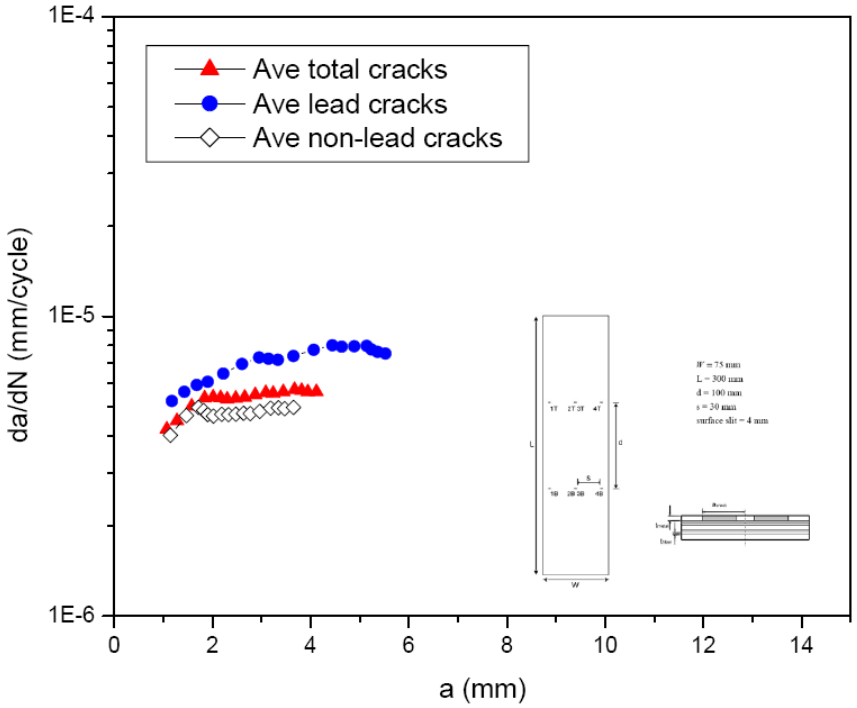

Figure 43. The MSD Crack Growth Rate as a Function of Crack Length at the Applied Stress of 100 MPa for Surface-Cracked GLARE Specimen

6. COMPARISON OF TEST AND ANALYSIS OF MULTIPLE-IMPACT LOADS AND FATIGUE CRACK GROWTH.

6.1 MULTIPLE-IMPACT LOADS.

6.1.1 Comparison of Experiment and FE Simulation.

In modeling multiple-site impacts on GLARE 5-2/1, the impact loads were repeated twice on the same position of the laminates. The double-impact procedure is shown in figures 44 and 45 for the first and second impact load, respectively. As the first impact load was applied to the GLARE 5-2/1 laminates, the second impact load was immediately applied. This procedure is identical to the experimental setup of multiple-impact loads. It was expected that the application of the second impact load would cause the GLARE laminates to experience larger deformation than the single impact case, as was observed in the experiments.

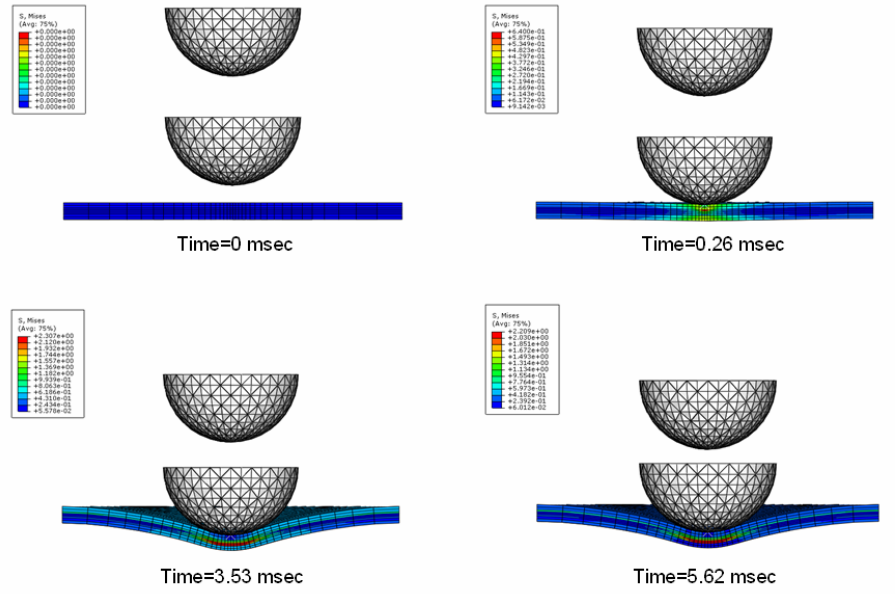

Figure 44. First Impact on GLARE 5-2/1

Literature proved that in the case of multiple-impact loads, the Al layer absorbs most of the energy instead of the composite layers [3 and 4] for the first impact. If the impact energy is relatively low for both 8-J and 16-J impact energy, the GLARE 5-2/1 Al layer experienced plastic deformation to absorb the impact energy.

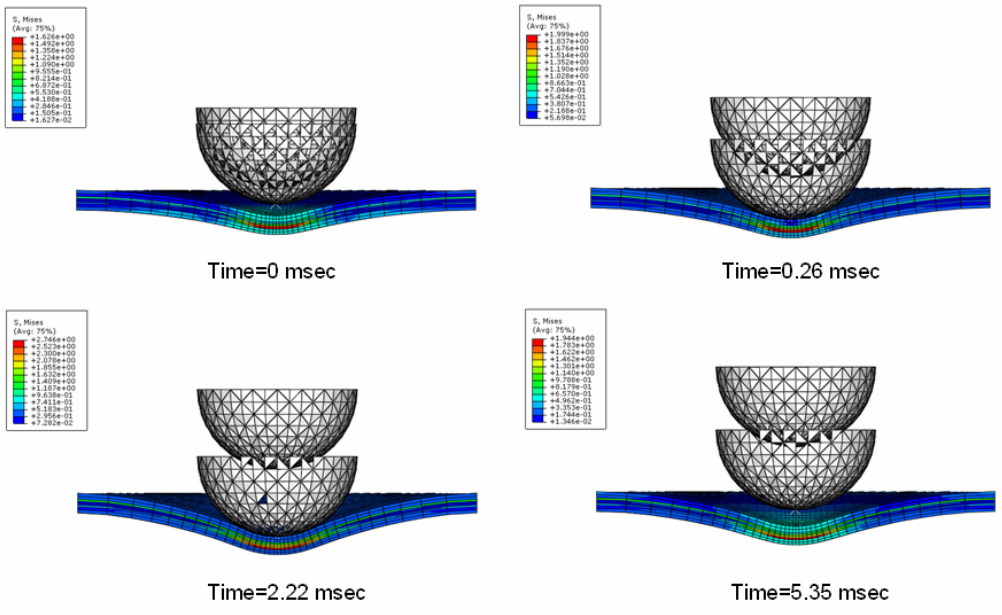

Figure 45. Second Impact on GLARE 5-2/1

Experimentally, the response of the impact force as a function of time was recorded automatically. Numerically, a reference point was set on the head of the drop weight to extract the response of the impact load. That is, the maximum impact response was used to compare to the experimental data. As shown in figure 46, the peak impact force was plotted as a function of time from the results of the 2D and 3D FE models, respectively. For ease of comparison, the nonfailure mode was used as a base line. Two sets of impact energies were studied and applied to GLARE 5-2/1 laminates, 8 J (2x4 J) and 16 J (2x8 J), respectively. In the FE simulation, only the cases with low-velocity impact load were considered. Hence, the 26-J impact energy, which would cause permanent metal cracking observed in experiments, was not within this scope of this study.

For the 8-J impact energy case, the load-time response in simulation was similar in trend during the first and second impact. This indicated that the failure criteria applied to the composite layers in both the 2D and 3D FE models did not critically affect the stiffness degradation in the GLARE laminates. Although the repeated load was applied to the GLARE laminates, only plastic deformation in the metal layers would occur as long as the impact energy was low. This can be proved by experimental observation or FE modeling. However, for the 16-J impact energy case, experimentally, dent damage was observed. Following the second impact load, damage accumulated and caused failure in both the aluminum and composite layers. In the FE simulation, it was observed that composite layers began to degrade either in the 2D or 3D model with Hashin failure criteria [20]. Clearly, both the 2D and 3D failure criteria models are capable of capturing the impact response of the laminate materials. The prediction model with nonfailure criteria would overestimate the impact force and time history compared to the experimental data or to the FE model with failure criteria setup. Therefore, it is important that the failure criteria be used to simulate damage progression in stiffness or compliance degradation.

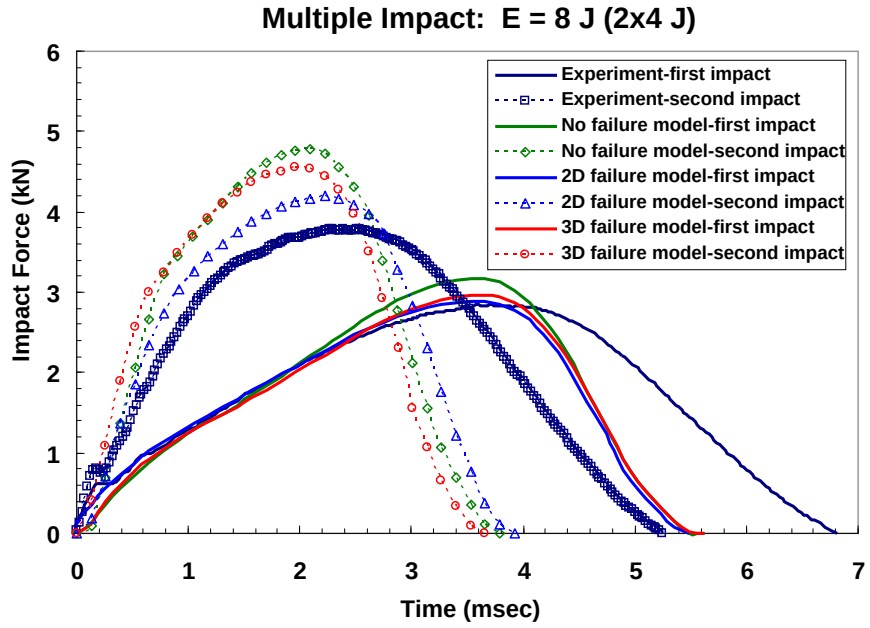

(a)

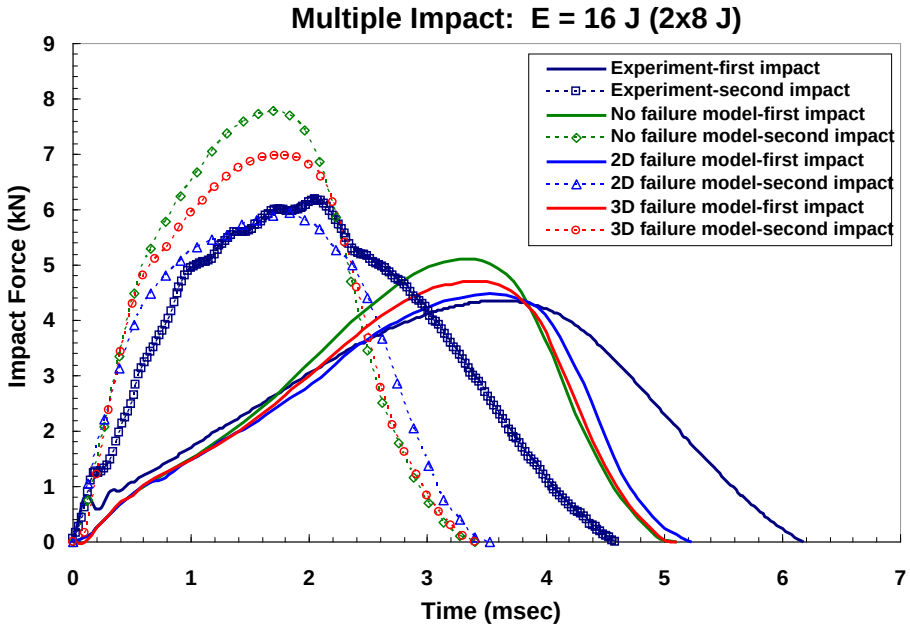

(b)

Figure 46. Comparisons of Experimental and Simulation Results of Multiple-Impact, Force-Time History for GLARE 5-2/1, Impact Energy (a) 8 J and (b) 16 J

Figure 47 shows the central displacement changes at different levels of impact energy. Because of the fully fixed boundary condition, the FE model of GLARE 5-2/1 is less deflected than the experiment after the first and second impact. There is no difference in the central displacement in the 2D and 3D failure models.

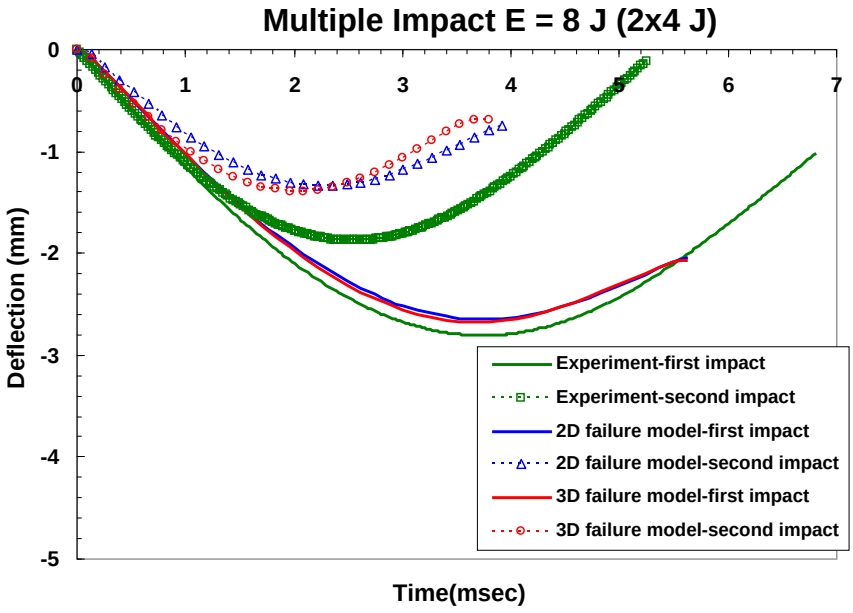

(a)

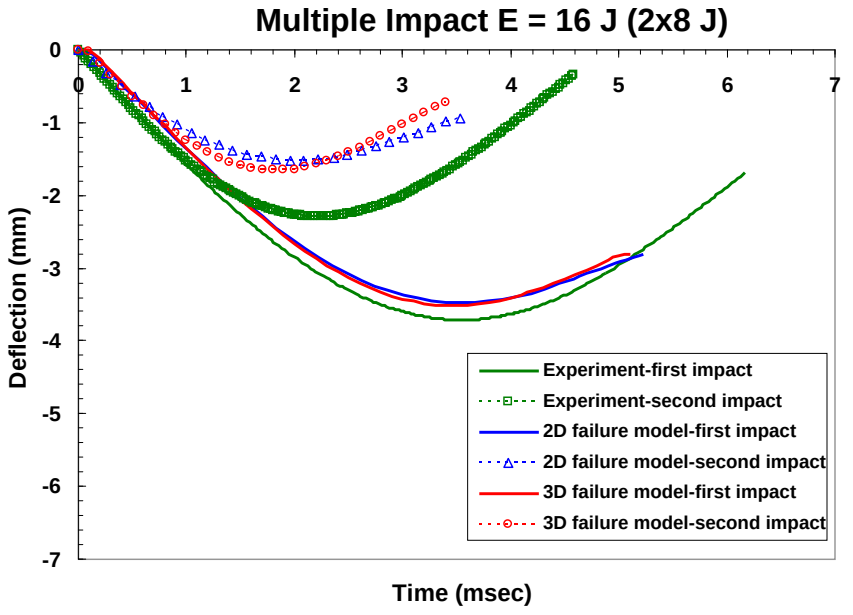

(b)

Figure 47. Difference Between Predicted and Measured Central Displacement for GLARE 5-2/1 Impact Energy (a) E = 8 J and (b) E = 16 J

6.1.2 Two- and Three-Dimensional Failure Criterion Comparison.

As mentioned, since the composite layer is so thin, 2D failure criterion works well under plane stress assumption problems. Thus, the 3D stress tensor $<\sigma_{13}, \sigma_{23}, \sigma_{33}>$ and the strain tensor $<\varepsilon_{13}, \varepsilon_{23}, \varepsilon_{33}>$ in the dynamic problem cannot be ignored because of three-directional large deformation. Even though 2D failure criteria may work in composite layers using the continuum shell element, 3D failure criteria, including three-directional stress and strain parts, is believed to compensate for the weak points for impact simulation.

A series of damage failure patterns in the 2D and 3D FE models were put together for comparison. These damage areas were compared based on the time step in simulation. Only failed regions were marked as red and the others were marked as white. In other words, the stress levels were purposely removed.

Figures 48 through 51 show the Hashin failure result in the GLARE 5-2/1 composite layers with different fiber orientations [0°/90°/90°/0°] and different impact energies. The damage progression induced by the first and second impact loads are also shown in these figures.

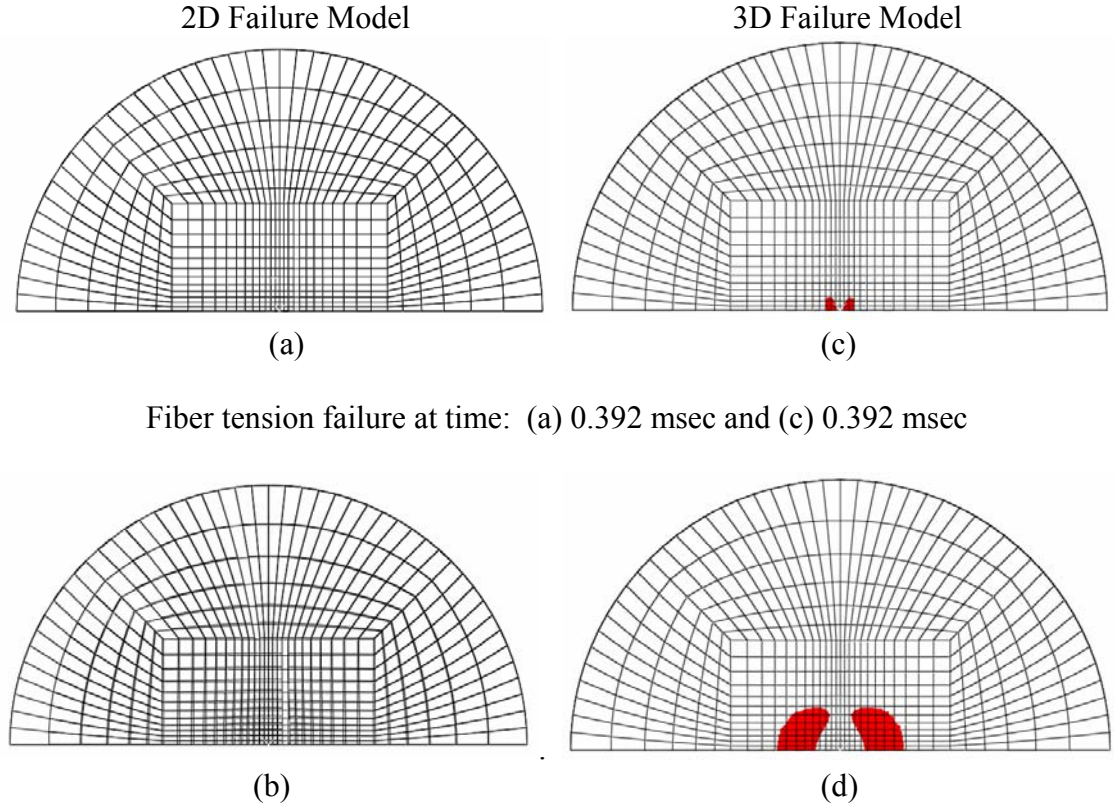

Fiber tension failure at time: (a) 0.392 msec and (c) 0.392 msec

Fiber tension failure at time: (b) 3.66 msec and (d) 3.66 msec

Figure 48. Failure Mode Comparison for 2D (left) and 3D (right) Models of GLARE 5-2/1 After First Impact E = 8 J

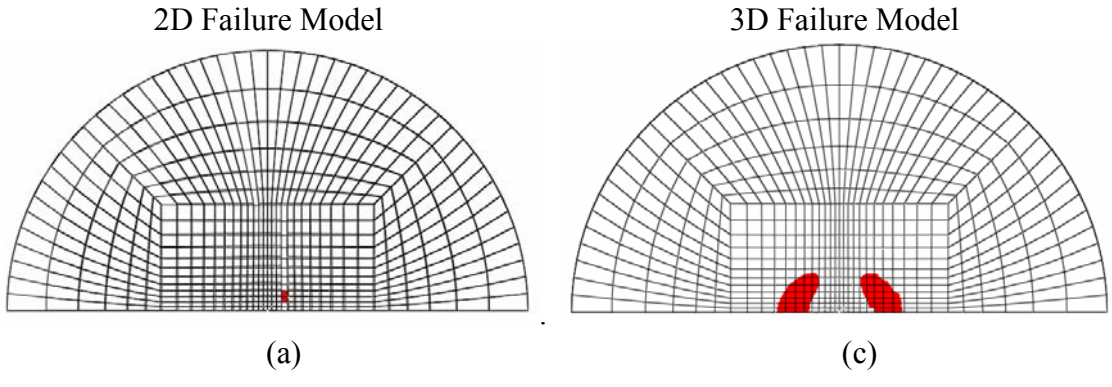

Fiber tension failure at time: (a) 0.392 msec and (c) 0.392 msec

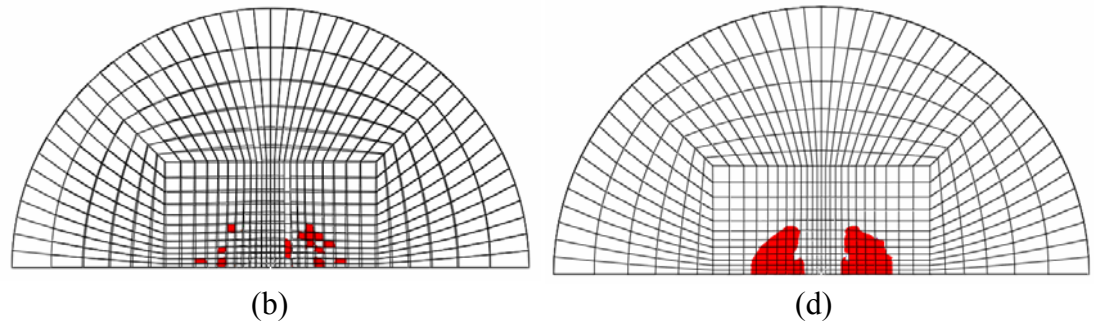

Fiber tension failure at time: (b) 2.22 msec and (d) 1.96 msec

Figure 49. Failure Mode Comparison for 2D (left) and 3D (right) Models of GLARE 5-2/1 After Second Impact E = 8 J

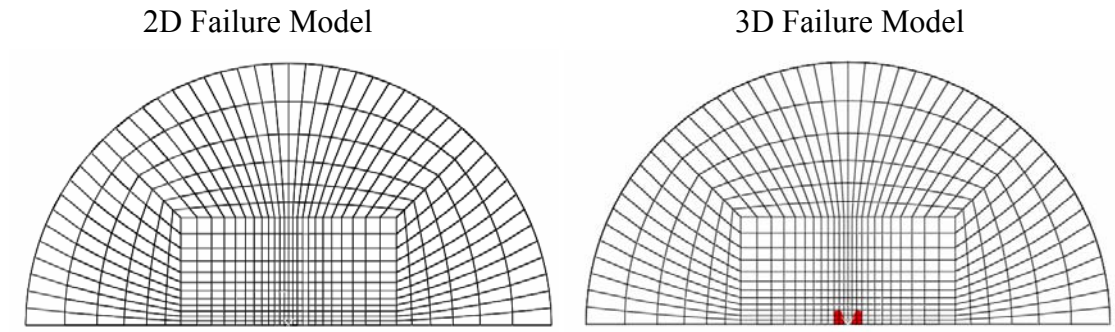

Fiber tension failure at time: (a) 0.392 msec and (c) 0.392 msec

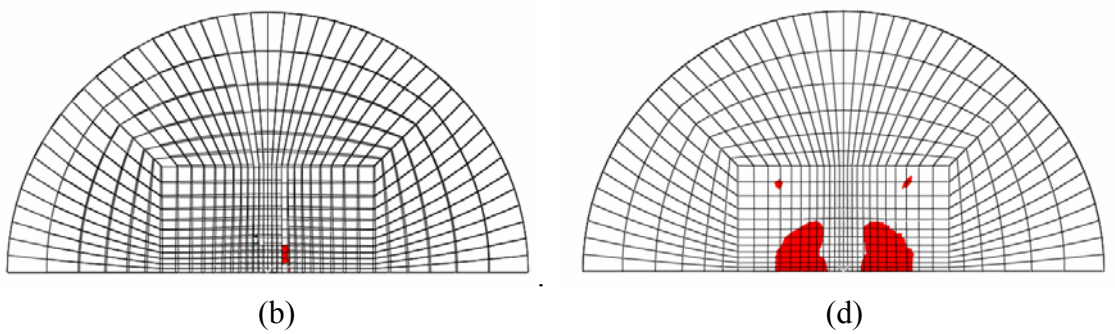

Fiber tension failure at time: (b) 3.53 msec and (d) 3.4 msec

Figure 50. Failure Mode Comparison for 2D (left) and 3D (right) Models of GLARE 5-2/1 After First Impact E = 16 J

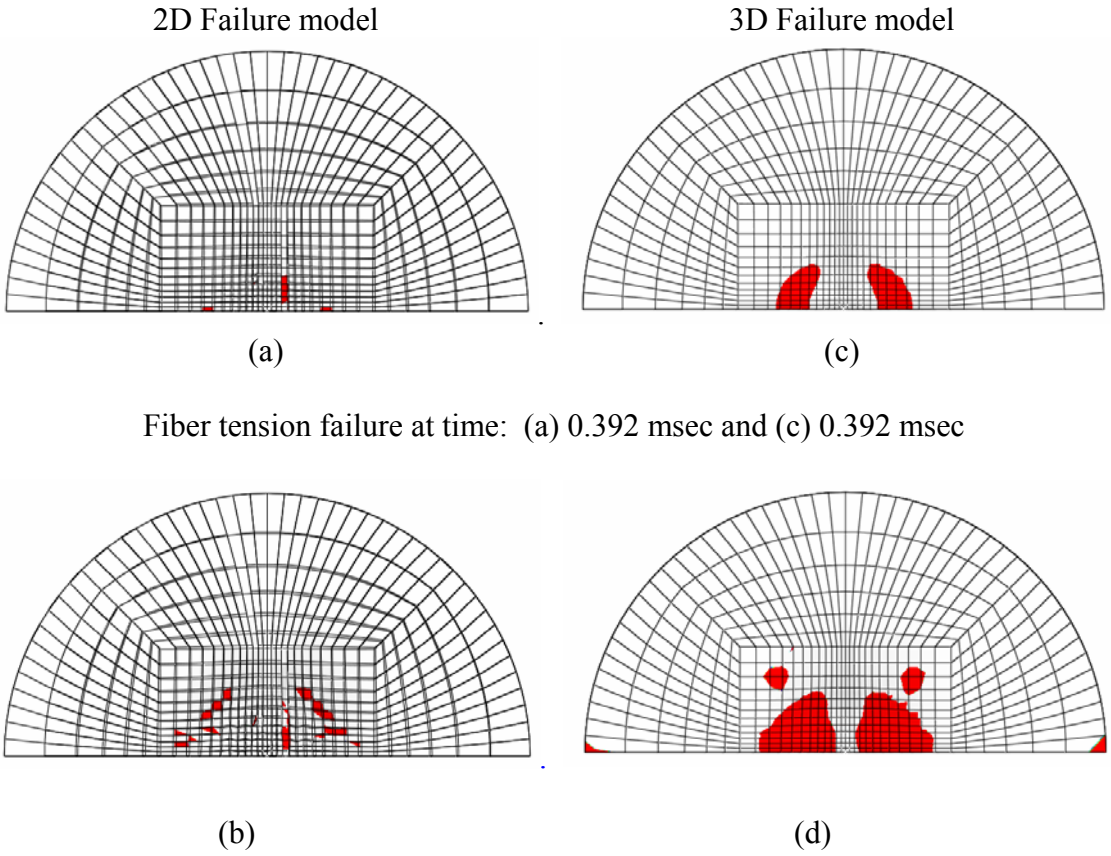

Figure 51. Failure Mode Comparison for 2D (left) and 3D (right) Models of GLARE 5-2/1 After Second Impact E = 16 J

The 2D failure damage models are shown in figures 48(a) and (b), 49(a) and (b), 50(a) and (b), and 51(a) and (b) at multiple-impact energy 8 and 16 J. The 3D failure criterion models are shown in figures 48(c) and (d), 49(c) and (d), 50(c) and (d), and 51(c) and (d). The damage area is realized by a state variable value greater than or equal to one that corresponds to a point at which the failure criteria value has been exceeded in the GLARE 5-2/1 composite layer. As shown in each figure, the FE model with 3D failure criteria clearly has a greater number of integration points marked as damaged areas when compared to the 2D failure criteria model.

Figure 52 shows the damage state in the GLARE 5-2/1 metal layer with Hashin failure criteria in composite layers. The differences between single- and multiple-impact loads are also shown in figure 52. It is known that compressive stress is exhibited on the nonimpacted side of the GLARE 5-2/1 specimens. The compressive stress on the impacted Al layer is small compared to the nonimpacted side. The colored damage is realized by a state variable value greater than or equal to one that corresponds to a point at which the failure criteria value has been exceeded. The colored areas display the failure or damage of the Al metal layer. The 3D FE model with failure criteria has more integration points that show damage initiation/progression when compared to the previous 2D model with failure criteria.

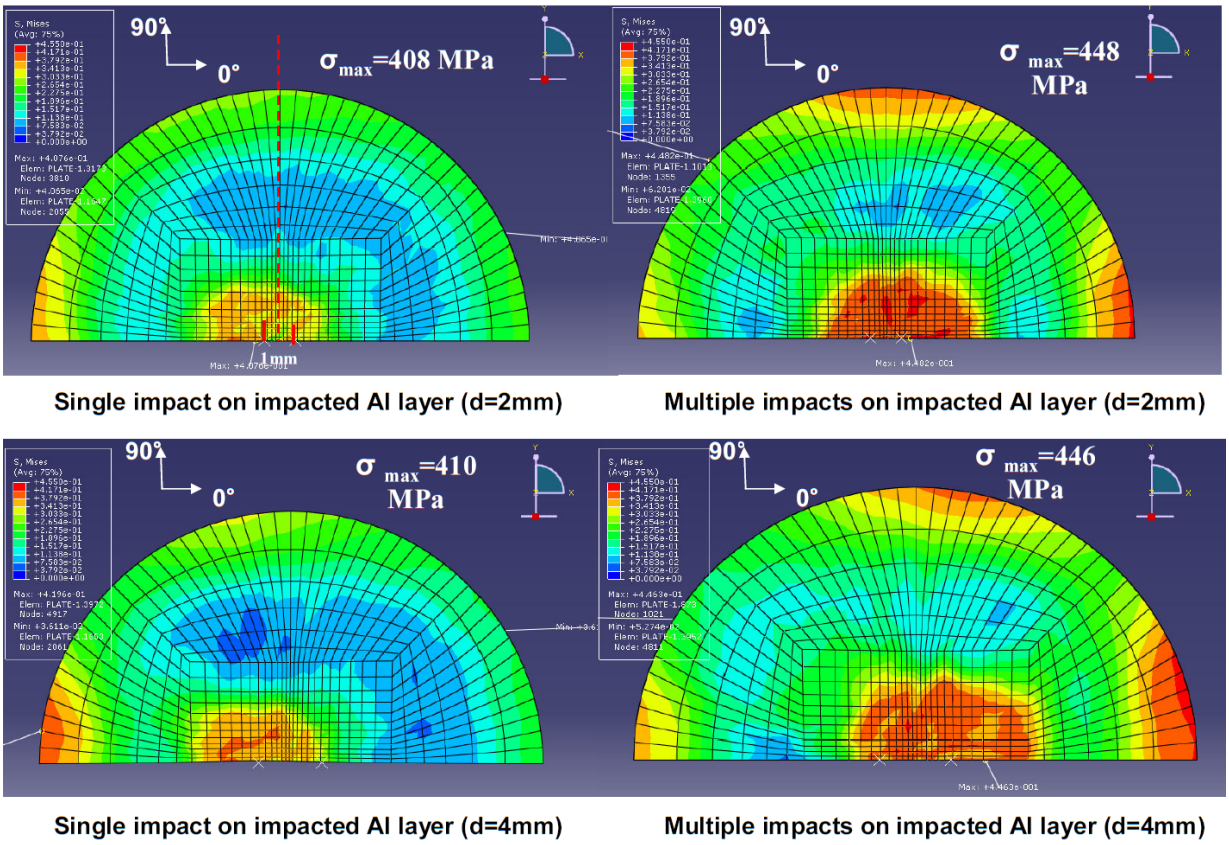

Figure 52. The 3D ABAQUS Simulation of Multiple-Site Impact Damage on GLARE 5-2/1

6.2 MULTIPLE-SITE DAMAGE FATIGUE CRACK GROWTH.

6.2.1 Through-Thickness Test Specimens.

To predict the average crack growth rates, the proposed methodology was used. At the initial stage, the crack growth of FMLs was faster due to the increasing fiber-bridging factor, followed by a steady-state crack growth due to the flat-out of fiber-bridging factor. In most MSD, the greatest concern is leading cracks; the predicted leading crack growth rates under different applied stress levels were averaged and plotted, as shown in figures 53 and 54, respectively.

The predicted crack growth rates using the proposed methodology were calculated under different applied stress levels. At the initial stage of crack growth, the far-field SIF dominates, so the crack growth is relatively faster than in the steady-state region. As the bridging SIF becomes predominant, the crack growth reaches a steady state. The presence of multiple-site fatigue cracks would accelerate the crack growth rates as two cracks approach each other. Therefore, as the propagating cracks approach each other, the crack growth rates increased gradually due to the effect of crack interactions. Ultimately, the crack growth rates reached the peak values when the cracks linked up. The predicted results under different maximum applied stress are in good agreement with the experimental results.

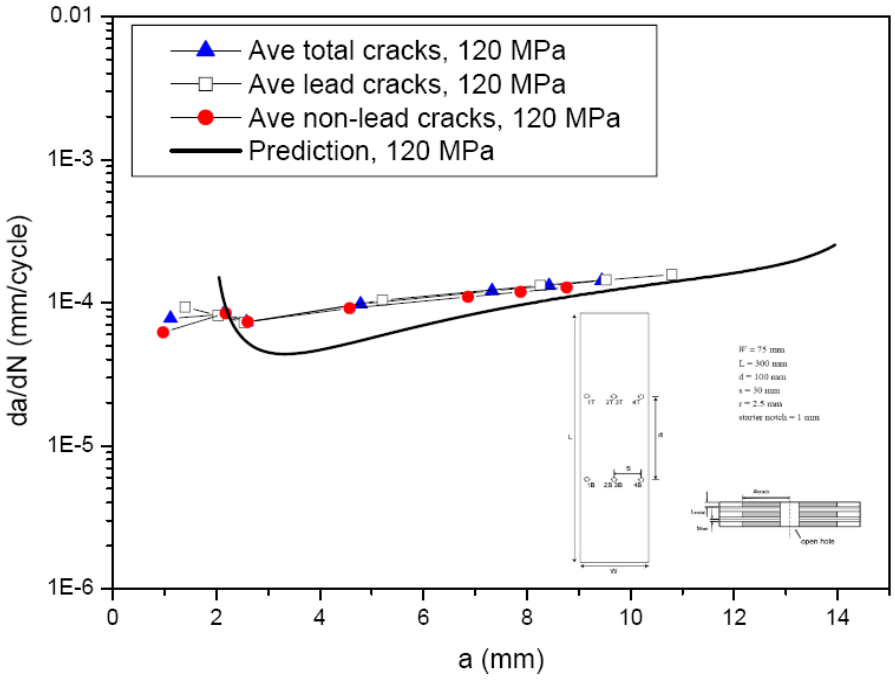

Figure 53. Comparison of Predicted Averaged Leading Crack Growth Rates and Experimental Results With an Applied Stress Ratio of 0.05 for GLARE 3-3/2 Through-Thickness Test Specimens (120 MPa)

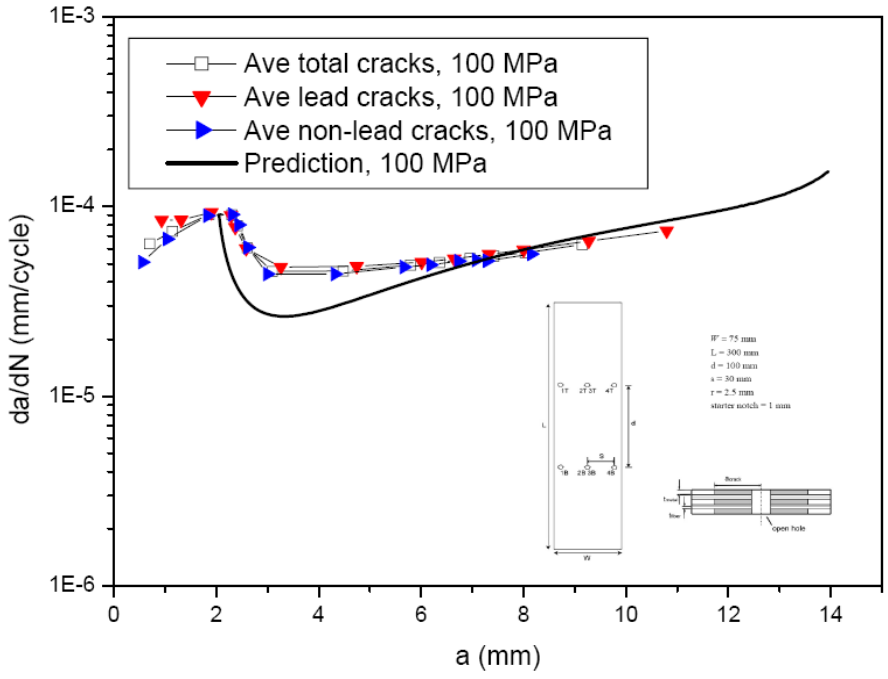

Figure 54. Comparison of Predicted Averaged Leading Crack Growth Rates and Experimental Results With an Applied Stress Ratio of 0.05 for GLARE 3-3/2 Through-Thickness Test Specimens (100 MPa)

6.2.2 Partial-Thickness Test Specimens.

The averaged crack lengths as a function of fatigue cycles under the maximum applied stress of 120 and 100 MPa were studied. Under the same fatigue cycles, the lead and nonlead cracks did not reach the same length, and crack growth deviation existed. Especially for cracks propagated at the applied stress of 100 MPa, the crack length deviation was obvious.

In FMLs, crack growth rate decelerated once the crack reached a certain length. When the cracked metal layer becomes more compliant, it will carry less load locally, which is the source of fatigue crack growth retardation. That is, there is load transferring to the fiber layers through the crack flanks and at the crack tips. Since the aluminum sheet has a higher modulus, it picks up more load than the S2-glass/prepreg. This higher percentage of overall load translates to higher stress in the metal layers to drive the cracks. On the experimental observation, surface crack growth is much slower compared to through-thickness crack growth. The further reduced crack growth rates in the surface-cracked GLARE laminates were attributed to the extent of greater bridging traction, provided by the intact laminates, and to the extent of higher residual strength. These surface-cracked specimens are more damage-tolerant than through-thickness GLARE 3-3/2 laminates.

The predicted results of averaged leading surface crack growth for GLARE 3-3/2 laminate were plotted in figures 55 and 56 at the applied stress levels of 120 and 100 MPa, respectively, along with the experimental results. The predicted crack growth rates agreed well with the experimental results of averaged crack growth rates, though discrepancy still existed for mainly nonlead cracks.

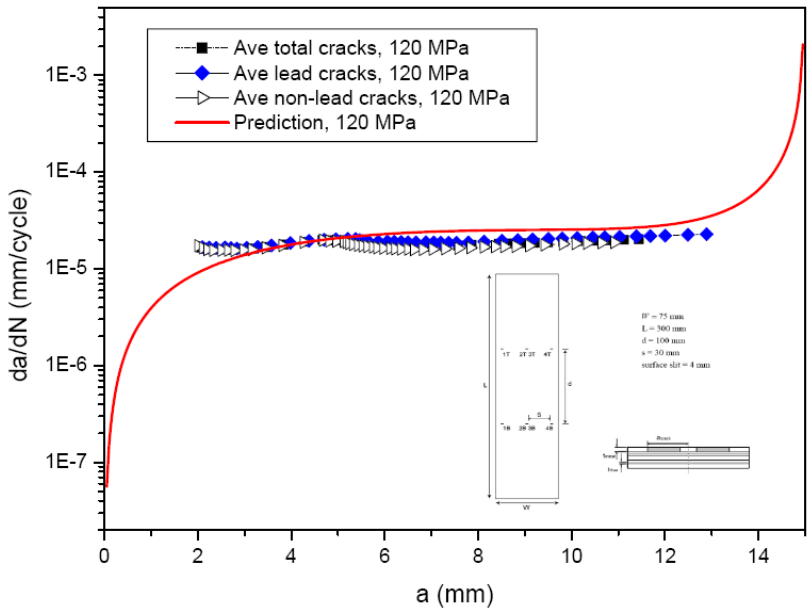

Figure 55. Comparison of Predicted Averaged Leading Crack Growth Rates and Experimental Results With an Applied Stress Ratio of 0.05 for GLARE 3-3/2 Partial-Thickness Test Specimens (120 MPa)

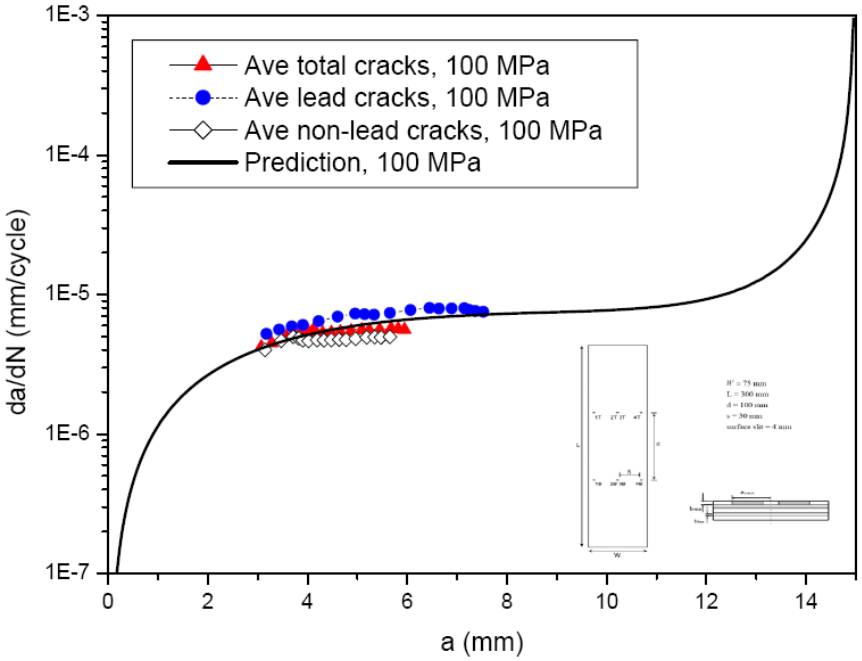

Figure 56. Comparison of Predicted Averaged Leading Crack Growth Rates and Experimental Results With an Applied Stress Ratio of 0.05 for GLARE 3-3/2 Partial-Thickness Test Specimens (100 MPa)

7. CONCLUSIONS.

The low-velocity, multiple-impact behavior for 2024-T3 aluminum alloy and S2-glass fiber-reinforced aluminum laminates (trade name GLARE) GLARE 5-2/1 was investigated through experiment and finite element (FE) simulation. Three different multiple-impact energies of 8 J (2x4 J), 16 J (2x8 J), and 26 J (2x13 J) were applied on aluminum alloy and GLARE 5-2/1 to induce two different levels of damage (barely visible impact damage (BVID) and clearly visible impact damage (CVID)). As in single-impact cases, the BVID of 8 J and 16 J introduced plastic deformation dents on the outer aluminum layer. The CVID of 26 J was characterized by cracks coming out from the plastic indentation in the fiber direction.

The FE analyses were performed on GLARE 5-2/1 for two different multiple-impact energies (8 J and 16 J). The 26-J impact energy caused metal cracking and was not studied in FE modeling in the scope of low-velocity multiple impacts. The FE simulation showed good agreement with experiment for impact force-time history curve. A three-dimensional failure criteria model was compared to a two-dimensional failure criteria model. Both failure models correlated well with the experimental results. But in the impact force-time history curve case, the two-dimensional failure model was better than the three-dimensional failure model to predict peak impact force in multiple-impact behavior. The damage progression size in the three-dimensional failure criteria model was bigger than the two-dimensional criteria failure model. The FE simulation results were able to predict where the crack can occur in post-multiple-impact fatigue behavior from the results of stress distribution on the impacted and nonimpacted aluminum layer of GLARE laminates.

The crack growth behavior of a fiber-metal laminate with multiple-site damage (MSD) has been investigated experimentally and analytically. To understand the surface crack growth in GLARE 3-3/2 laminates, the surface-bridging mechanism and the secondary bending effect were proven through data analysis and experimental work, which supported the arguments. It was concluded that in fiber-metal laminates with through-thickness MSD, as the fatigue cracks emanated from the open holes and propagated, the crack growth rate was faster with the presence of MSD cracks as compared to the case without the interaction of MSD cracks. The propagating cracks tended to bypass each other and formed an eye-shaped region as two propagating cracks approached each other before linkup, mode I fracture behavior dominates and results in crack linkup at the vicinity of the crack tips. The crack growth acceleration was not observed at the vicinity of crack linkup in experiments with multiple surface slits. As surface cracks linkup in the metal layer, delaminations in the interface of metal/prepreg linkup with each other simultaneously. The fatigue crack resistance in surface crack growth was better than in the through-thickness crack growth. The proposed methodology for predicting the crack growth rates of GLARE laminates with multiple-site fatigue damage was validated with experiments under constant-amplitude fatigue load at a variety of stress levels.

8. REFERENCES.

1. Vogelesang, L.B., Marissen, R., and Schijve, J., "A New Fatigue Resistant Material: Aramid Reinforced Aluminum Laminate (ARALL)," *Proceedings of the 11th ICAF Symposium*, Noordwijkerhout, NLR, 1981, pp. 3.4/1-3.4/39.

2. Vlot, A. and Gunnink, J.W., eds., *Fibre Metal Laminates-An Introduction*, Kluwer Academic Publisher, USA, 2001.

3. Wu, G. and Yang, J.-M., "The Mechanical Behavior of GLARE Laminates for Aircraft Structures," *JOM*, Vol. 57, No. 1, January 2005, pp.72-79.

4. Wu, G. and Yang, J.-M., "The Impact Properties and Damage Tolerance and of Bidirectionally Reinforced Fiber Metal Laminates," *Journal of Material Science*, Vol. 42, No. 3, 2007, pp. 948-957.

5. Cantwell, W.J. and Morton, J., "The Impact Resistance of Composite Materials—A Review," *Composites*, Vol. 22, Issue 5, 1991, pp. 347-362.

6. Found, M.S. and Howard, I.C., "Single and Multiple Impact Behaviour of a CFRP Laminate," *Composite Structures*, Vol. 32, 1995, pp. 159-163.

7. Rotem, A., "The Strength of Laminated Composite Materials Under Repeated Impact Loading," *Journal of Composites Technology and Research*, Vol. 10, No. 2, 1988, pp. 19-27.

8. Harris, B., Chen, A.S., Coleman, S.L., and Moore, R.J., "Residual Strength and Toughness of Damaged Composites," *Journal of Material Science*, Vol. 26, 1991, pp. 307-320.

9. Mittelman, A., "Low-Energy Repetitive Impact in Carbon-Epoxy Composites," *Journal of Material Science*, Vol. 27, 1992, pp. 2458-2462.

10. Jones, R., "Residual Strength of Composites With Multiple Impact Damage," *Composite Structures*, Vol. 28, 1994, pp. 347-356.

11. Al-Hassani, S.T.S., "Numerical Simulation of Multiple Shot Impact," *The 7th International Conference on Shot Peening*, Institute of Precision Mechanics, Warsaw, Poland, 1999.

12. Partl, O. and Schijve, J., "Multiple-Site Damage in 2024-T3 Alloy Sheet," *International Journal of Fatigue*, Vol. 15, No. 4, 1993, pp. 293-299.

13. Jones, R., Molent, L., and Pitt, S., "Study of Multi-Site Damage of Fuselage Lap Joints," *Theoretical and Applied Fracture Mechanics*, Vol. 32, 1999, pp. 81-100.

14. Park, J.H., Singh, R., Pyo, C.R., and Atluri, S.N., "Integrity of Aircraft Structural Elements With Multi-Site Fatigue Damage," *Engineering Fracture Mechanics*, Vol. 51 Issue 3, 1995, pp. 361-380.

15. Schijve, J., "Multiple-Site Damage in Aircraft Fuselage Structures," *Fatigue Fracture Engineering Material Structure*, Vol. 18, No. 3, 1995, pp. 329-344.

16. Pitt, S. and Jones, R., "Multiple-Site and Widespread Fatigue Damage in Aging Aircraft," *Engineering Failure Analysis*, Vol. 4, No. 4, 1997, pp. 237-257.

17. Schijve, J., "Fatigue of Aircraft Materials and Structures," *International Journal of Fatigue*, Vol. 16, No. 1, 1994, pp. 21-32.

18. Schijve, J., "Prediction of Fatigue," *Japan Society of Mechanical Engineers International Journal Series I—Solid Mechanics, Strength of Materials*, Vol. 34, No. 3, 1991, pp. 269-280.

19. Alderliesten, R.C. and Homan, J.J., "Fatigue Crack Growth Behaviour of Surface Cracks in GLARE, Advances in Damage Mechanics," *Fatigue Damage of Materials: Experiment and Analysis*, Wessex Institute of Technology Press, United Kingdom, 2003, pp. 213-222.

20. Schijve, J., Campoli, G., and Monaco, A., "Fatigue of Structures and Secondary Bending in Structural Elements," *International Journal of Fatigue*, Vol. 31, 2009, pp.1111–1123.

21. Guo, Y.J. and Wu, X.R., "A Phenomenological Model for Predicting Crack Growth in Fiber-Reinforced Metal Laminates under Constant-Amplitude Loading," *Composites Science and Technology*, Vol. 59, 1999, pp. 1825–31.

22. ASTM D 3479, "Standard Test Method for Tension-Tension Fatigue of Polymer Matrix Composite Materials," *American Society for Testing and Materials (ASTM) Standards and Literature References for Composite Materials*, ASTM, pp. 67-70.

23. "A Finite Element System," *ABAQUS User Manual, Ver. 6.7*, Dassault Systems Inc., 2008.

24. Linde, P., Pleitner, J., De Boer, H., and Carmone, C., "Modeling and Simulation of Fiber Metal Laminates," *ABAQUS User's Conference*, Boston, Massachusetts, 2004.

25. Hashin, Z., "Failure Criteria for Unidirectional Fiber Composites," *Journal of Applied Mechanics*, Vol. 47, 1980, pp. 329-335.

26. DeVries, T.J., "*Blunt and Sharp Notch Behavior of GLARE Laminate,*" Ph.D. Dissertation, Delft University Press, 2001.

27. Hengenbeek, M., VanHengel, C., Bosker, O.J., and Vermeerne, C.A.J.R., "Static Properties of Fibre Metal Laminates," *Applied Composite Materials*, Vol. 10, 2003, pp. 207-222.

28. Nguyen, M.Q., Elder, D.J., Bayandor, J., Thomson, R.S., and Scott, M.L., "A Review of Explicit Finite Element Software for Composite Impact Analysis," *Journal of Composite Materials*, Vol. 39, No. 4, 2005, pp. 375-386.

29. Matzenmiller, A., Lubliner, J., and Taylor, R.L., "A Constitutive Model for Anisotropic Damage in Fiber Composites," *Mechanics of Materials*, Vol. 20, No. 2, 1995, pp. 125-152.

30. Iannucci, L., Dechaene, R., Willows, M., and Degrieck, J., "A Failure Model for the Analysis of Thin Woven Glass Composite Structures Under Impact Loadings," *Computer and Structures*, Vol. 79, 2001, pp. 785-799.

31. Chang, P.Y., Yeh, P.C., and Yang, J.M., "Fatigue Crack Initiation in Hybrid Boron/Glass/Aluminum Fiber Metal Laminates," *Materials Science and Engineering A*, Vol. 496, 2008, pp. 273–280.

32. Chang, P.Y., Yang, J.M., Seo, H., and Hahn, H.T., "Off-Axis Fatigue Cracking Behaviour of Notched Fiber Metal Laminates," *Fatigue and Fracture of Engineering Materials and* Structures, Vol. 30, 2007, pp.158-1171.

33. Schijve, J., Campoli, G., and Monaco, A., "Fatigue of Structures and Secondary Bending in Structural Elements," *International Journal of Fatigue*, Vol. 31, 2009, pp.1111–1123.

34. Guo, Y.J. and Wu, X.R., "A Theoretical Model for Predicting Fatigue Crack Growth Rates in Fibre-Reinforced Metal Laminates," *Fatigue Fracture Engineering Material Structure*, Vol. 21, 1998, pp. 1133-45.

35. Guo, Y.J. and Wu, X.R., "Bridging Stress Distribution in Center-Cracked Fiber Reinforced Metal Laminates: Modeling and Experiment," *Engineering Fracture Mechanics*, Vol. 63, 1999, pp. 147-63.

36. Alderliesten, R.C., "Analytical Prediction Model for Fatigue Crack Propagation and Delamination Growth in GLARE," *International Journal of Fatigue*, Vol. 29, 2007, pp. 628-646.

37. Chang, P.Y. and Yang, J.M., "Modeling of Fatigue Crack Growth in Notched Fiber Metal Laminates," *International Journal of Fatigue*, Vol. 30, 2008, pp. 2165–2174.

38. Chang, P.Y., Yeh, P.C., and Yang, J.M., "Fatigue Crack Growth in Hybrid Boron/Glass/Aluminum Fibre Metal Laminates," *Fatigue Fracture Engineering Material Structure*, Vol. 30, 2008, pp. 989-1003.

39. Tada, H., Paris, P.C., and Irwin, G.R., *The Stress Analysis of Cracks Handbook*, 3rd ed., The American Society of Mechanical Engineers, 2000.

40. Alderliesten, R.C., "*Fatigue Crack Propagation and Delamination Growth in GLARE,*" Ph.D. Thesis, Delft University of Technology, Delft, Netherlands, 2005.

41. Alderliesten, R.C., Campoli, G., and Benedictus, R., "Modeling Cyclic Shear Deformation of Fibre/Epoxy Layers in Fibre Metal Laminates," *Composites Science and Technology*, Vol. 67, Issues 11-12, 2007, pp. 2545-2555.

42. Wu, X.R. and Carlsson, A.J., "*Weight Functions and Stress Intensity Factor Solutions,*" Pergamon Press, 1991.

43. Newman, J.C., "A Crack Opening Stress Equation for Fatigue Crack Growth," *International Journal of Fracture*, Vol. 24, 1984, pp. R131-R135.

44. Alderliesten, R.C., "Application of the Energy Release Rate Approach for Delamination Growth in GLARE," *Engineering Fracture Mechanics*, Vol. 73, No. 6, 2006, pp. 697-709.

45. Suiker, A.S.J. and Fleck, N.A., "Crack Tunneling and Plane-Strain Delamination in Layered Solids," *International Journal of Fracture*, Vol. 125, 2004, pp. 1-32.